

ABSTRACT

Title of Dissertation: MAGNETISM IN MULTIPLY
 CONNECTED SUPERCONDUCTORS

Aaron Philip Nielsen, Doctor of Philosophy, 2001

Dissertation directed by: Professor Christopher J. Lobb
 Department of Physics

We used a scanning liquid-helium cooled superconducting quantum interference device microscope to study the magnetic properties of superconducting devices and thin films from 4.2 K to 13 K. The microscope provides spatially resolved magnetic information about samples and a new source of data to test existing theories of the distribution of magnetic field in superconductors.

In Nb – Al₂O₃ – Nb Josephson-junction arrays of differing square lattice geometry (30×100 and 100×150) we made field-cooled measurements of the magnetization as a function of external field (from zero up to 3 G) and found that the array is preferentially paramagnetic. This demonstrates that the observation of paramagnetism in a superconductor does not provide evidence for an exotic symmetry in the order parameter. Furthermore, we explain this preferential paramagnetism with a simple model for flux screening which has applicability to a generic multiply-connected superconducting system.

In $\text{YBa}_2\text{Cu}_3\text{O}_{7-\delta}$ films on Rolled Annealed Biaxially Textured Substrates (RABiTSTM)¹ we found the spontaneous magnetization of the RABiTS substrates to be more complicated than described in previously published work. Furthermore, we found YBCO films on RABiTS films to have small holes (diameter $< 10\text{ }\mu\text{m}$) which we positively correlate to the spatial dependence of DC magnetic hysteresis in the films. Additionally, we made detailed measurements of the magnetic field distribution in the Meissner state (reversible magnetization) for YBCO films on strontium titanate substrates. From these measurements we determined the demagnetizing factor to be 0.961 and the first critical field to be less than 300 mOe. Additionally, we infer the current distribution which leads to this magnetic field distribution and demonstrate that it agrees with recent theoretical predictions.

¹RABiTS is a registered trademark of Oak Ridge National Laboratory.

MAGNETISM IN MULTIPLY
CONNECTED SUPERCONDUCTORS

by

Aaron Philip Nielsen

Dissertation submitted to the Faculty of the Graduate School of the
University of Maryland at College Park in partial fulfillment
of the requirements for the degree of
Doctor of Philosophy
2001

Advisory Committee:

Professor Christopher J. Lobb, Chairman/Advisor
Associate Professor Steven Anlage
Associate Professor Frederick C. Wellstood
Assistant Professor Paola Barbara, Georgetown University
Assistant Professor Romel Gomez, Electrical Engineering

©Copyright by
Aaron Philip Nielsen
2001

DEDICATION

To my father

ACKNOWLEDGEMENTS

Fred Cawthorne did a beautiful job of setting up the lab, and organizing things (as well as amassing an unsurpassed collection of resistors, capacitors and other miscellaneous electronic components). It is only possible to use the SQUID microscope today because of his hard work. The original designs for the SQUID computer control were his and have provided a great base to build upon. Fred Strauch worked a brief time in the sub-sub-basement made great contributions to the automation of the scanning procedure by implementing GPIB control in the microscope controller.

Prof. Rick Newrock, at the University of Cincinnati, has been very gracious in allowing periodic visits to the University of Cincinnati to discuss the microscope and the results and conclusions of PME measurements. I am greatly indebted to him for acknowledging my work in several presentations of his. I also need to thank Jenny Holzer,

a student of Prof. Newrock, who provided several crucial pieces of knowledge required to run the SQUID microscope.

I am greatly indebted to Erin Fleet and Guy Chatraphorn for providing assistance and inspiration in working with and interpreting the data from the SQUID microscope. Perhaps most importantly, it was with their help that we developed the important sub-basement conservation law for SQUIDs.

I have to thank Brana Vasilic for many very useful conversations, particularly about the meaning of the quantum number n . Doug Strachan has been a great friend down in the sub-sub-basement, and as the only other member of the sub-sub-basement coffee club has been the source of many great ideas and fruitful conversations. Roberto Ramos provided many useful ideas for the work with the probe. Matt Kenyon was a great source of help, especially in the early stages with leak checking.

Of course, none of this would have been possible without the excellent help from Jane Hessing who always made sure I was caught up with the university bureaucracy. Becky Lorenz is a great welder and without her skilled hands the SQUID microscope would have been in a state of perpetual leaks.

Most importantly, I must thank Evelyn for putting up with all of my crazy schemes and for graciously allowing me to make helium transfers in the middle of many dates.

TABLE OF CONTENTS

List of Tables	x
List of Figures	xi
1 Introduction	1
1.1 The Meissner effect	1
1.2 Types of superconductors	2
1.3 Structure of the thesis	3
2 Josephson-junction arrays as models of multiply-connected superconductors	5
2.1 Introduction	5
2.2 Single plaquette of Josephson-junction array	6
2.2.1 RCSJ model	7
2.2.2 The meaning of the quantum number n	10
2.2.3 Time independent external field	12
2.2.4 Time-dependent external field	18
2.2.5 Gibbs free energy of single loop stable solutions	19
2.2.6 Non-identical junctions	19
2.3 Complete model of entire array	21

2.3.1	Mutual induction matrix	24
3	Paramagnetic Meissner effect in Josephson-junction arrays	27
3.1	Introduction	27
3.1.1	Paramagnetic Meissner effect in high T_c superconductors .	27
3.1.2	Paramagnetic Meissner effect in low T_c superconductors . .	28
3.2	Our samples	29
3.3	Experimental technique	31
3.4	Experimental results	46
3.4.1	30×100 junction array	46
3.4.2	100×150 junction array	51
3.5	Summary of magnetization measurements	55
4	A model of the paramagnetic Meissner effect in multiply-connected superconductors	57
4.1	Introduction	57
4.1.1	π -junction models	57
4.1.2	Josephson-junction array models	58
4.1.3	Flux compression	59
4.1.4	Pinning and surface barriers	60
4.2	Comparison of experimental data to various models	60
4.3	Mean field theory of Josephson-junction array	62
4.4	Array screening	62
4.4.1	Self-inductance of square loop	65
4.4.2	Screening due to large loop around edge of array	68
4.4.3	Screening due to single plaquettes	69

4.4.4	Outer diamagnetic current	71
4.5	Consequences of edge loop screening	74
4.5.1	Internal plaquette response to fields generated by external plaquettes	76
4.5.2	Array response to external field plus screening fields	76
4.5.3	Numerical array simulations	77
5	Magnetic penetration into $\text{YBa}_2\text{Cu}_3\text{O}_{7-\delta}$ thin films	81
5.1	Introduction	81
5.1.1	Rolling-assisted, biaxially-textured structures	82
5.1.2	Magnetic penetration into YBCO films	83
5.2	YBCO on RABiTS	86
5.2.1	RABiTS AC susceptibility	89
5.2.2	RABiTS DC hysteresis measurements	98
5.3	Magnetic penetration into YBCO thin films	104
5.3.1	Experimental details	104
5.3.2	Meissner state	106
5.3.3	Demagnetization factor	112
5.3.4	Remanence in YBCO films	114
6	Prospective	119
6.1	Introduction	119
6.2	Vortex avalanches	119
6.2.1	Avalanche phenomenology	120
6.2.2	Potential avalanche explanations and further experiments .	127
6.3	Vortex ratchets	130

A	Low T_c scanning SQUID microscope	136
A.1	Introduction	136
A.2	Mechanical design	137
A.2.1	Thermometer placement	137
A.2.2	Friction	140
A.2.3	Vacuum quality	140
A.2.4	Scanning range	142
A.3	SQUID design	142
A.4	Electronic design	143
A.4.1	Digital phase detector	143
A.4.2	Electronic frequency response	147
B	Computer control documentation	149
B.1	General overview	149
B.2	Computer controller and software	150
B.2.1	SCAN CONFIG menu, setting the controller parameters	150
B.2.2	GPIB control	152
B.3	Stepper motors	156
B.3.1	Coordinate systems	157
B.4	A/D board	160
B.5	Manual control	160
B.5.1	Joystick control	161
B.6	Scanning	161
C	Experimental procedure	162
C.1	Preparing probe for measurements	162

C.1.1	Sample mounting	162
C.1.2	SQUID mounting	164
C.1.3	SQUID and sample contacts	167
C.1.4	Sample and SQUID alignment	167
C.2	Pumping down and leak checking	172
C.3	Pre-cooling in liquid nitrogen	173
C.4	Cooling with liquid helium	174
C.5	Finding the sample	176
C.6	Day to day operation	177
C.6.1	Holding	177
C.6.2	Scanning	178
C.7	Warming up	179
C.8	Vacuum leak information	179

Bibliography	183
---------------------	------------

LIST OF TABLES

B.1	SQUIDBox GPIB Commands	153
C.1	Room temperature flange pinouts at room temperature	168
C.2	Room temperature flange pinouts at 77 K	169
C.3	Room temperature flange pinouts at 4.2 K	170
C.4	Typical values for the alignment parameters of the SQUID and the sample.	172

LIST OF FIGURES

2.1	One plaquette of a Josephson-junction array.	8
2.2	Circuit schematic of single Josephson junction.	8
2.3	ϕ plotted against ϕ_{ext} for $\beta_{\ell} = 30$ and $N = 4$ for different values of the quantization number n	13
2.4	Single loop magnetization <i>vs.</i> external flux.	15
2.5	Gibbs free energy calculated for a four-junction loop with $\beta_{\ell} = 30$	20
2.6	Sketch of Josephson-junction array with labeled variables for nu- merical modeling.	22
2.7	Block arrangement used to compute mutual induction matrix.	25
3.1	Optical micrograph of Josephson-junction array samples used in the PME experiment.	30
3.2	Experimental arrangement of sample Josephson-junction array and SQUID in the probe.	32
3.3	Magnetic image of sample after field cooling in $\phi_{\text{ext}} = 4.8$, $T = 4.2$ K.	35
3.4	Magnetic image of zero field cooled sample, $T = 4.2$ K.	36
3.5	Magnetic image of $\phi_{\text{ext}} = 4.8$, $T = 13$ K.	37
3.6	Magnetic image of zero field, $T = 13$ K.	38
3.7	Magnetization of 30×100 junction array after field cooling in $\phi_{\text{ext}} =$ 4.8.	39

3.8	Histogram of the magnetization data shown in the magnetization image, Fig. 3.7.	40
3.9	Magnetization of 30×100 junction array after field cooling in $\phi_{\text{ext}} = 1.2$	41
3.10	Histogram of the magnetization data shown in the magnetization image, Fig. 3.9.	42
3.11	Zero-field cooled, with SQUID on top, magnetic image of sample.	44
3.12	Histogram of background magnetization for $\phi_{\text{ext}} = 4.8$, from Fig. 3.7.	48
3.13	Histogram of background magnetization for $\phi_{\text{ext}} = 1.2$, from Fig. 3.9.	49
3.14	Measured mean magnetization for 30×100 junction array plotted versus cooling field.	52
3.15	Representative paramagnetic image for the 100×150 junction array.	53
3.16	Paramagnetic histogram shown in Fig. 3.15.	54
3.17	Measured mean magnetization versus cooling field for 100×150 junction array.	56
4.1	Effect of the mean field due to surrounding plaquettes in the array.	63
4.2	Comparative array screening: individual plaquette <i>vs.</i> large outside loop.	64
4.3	Geometry for calculation of square loop self inductance.	67
4.4	Computed self inductance of a square current loop.	70
4.5	Different array screening configurations for individual plaquettes.	70
4.6	Close up view to two adjacent plaquettes with screening currents.	72
4.7	Schematic of interior and exterior plaquettes, with screening provided by external plaquettes only.	75

4.8	Modeled array magnetization for a 10×40 Josephson-junction array, field cooled in $\phi_{\text{ext}} = 4.8$	78
4.9	Simulated array magnetization <i>vs.</i> cooling field.	80
5.1	Optical micrographs of YBCO deposited on RABiTS and STO. . .	84
5.2	Sample geometry used magnetic penetration experiment analysis.	85
5.3	Magnetic image of bare RABiTS substrate.	88
5.4	Magnetic image of zero field cooled YBCO on RABiTS.	90
5.5	YBCO on RABiTS AC susceptibility images at 1 kHz.	92
5.6	YBCO on RABiTS AC susceptibility images at 500 kHz.	93
5.7	χ' and χ'' line cuts through AC susceptibility measurements. . . .	96
5.8	DC hysteresis before and after images of YBCO/RABiTS.	100
5.9	DC hysteresis difference and gradient images of YBCO/RABiTS.	101
5.10	Before and after line cuts of DC hysteresis images at a height of $50 \mu\text{m}$	103
5.11	Before and after line cuts of DC hysteresis images at a height of $15 \mu\text{m}$	105
5.12	Meissner state image and line cut of YBCO film on STO.	107
5.13	Remanence image of YBCO/STO film after peak field of 223 mOe.	109
5.14	Comparison of Meissner state field profile with Vodolazov <i>et al.</i> predictions.	111
5.15	Remanence image of YBCO/STO film after peak field of 57.4 Oe.	116
5.16	Magnetic field profiles of the remanence critical state in YBCO films.	117
6.1	Successive vortex avalanches in to Josephson-junction array, zero field cooled.	121

6.2	Successive vortex avalanches in to Josephson-junction array, the external field has been ramped to $4.8 \Phi_0$ per unit cell.	122
6.3	Successive vortex avalanches in to Josephson-junction array, the external field has been ramped to $2.4 \Phi_0$ per unit cell.	123
6.4	Magnetic field images taken between vortex avalanches, at $\Phi_{\text{ext}} = 2.52 \Phi_0$ per unit cell of the array.	124
6.5	Magnetic field images taken between vortex avalanches, at $\Phi_{\text{ext}} = 2.64 \Phi_0$ per unit cell of the array.	125
6.6	Magnetic field images taken between vortex avalanches, at $\Phi_{\text{ext}} = 2.76 \Phi_0$ per unit cell of the array.	126
6.7	Schematic of shunted Josephson junction.	133
6.8	Alpha step scan for ratchet samples. Opposing asymmetric sawtooth ratchets.	134
6.9	Alpha step scan for ratchet samples. Unidirectional asymmetric sawtooth ratchets.	135
A.1	Detail of cold flange heat sinking	138
A.2	Sketch of probe detailing major parts	139
A.3	SQUID electronics output <i>vs.</i> SQUID temperature	141
A.4	Optical micrograph of SQUID chip and washer	144
A.5	Circuit schematic for SQUID electronics digital phase detector. . .	145
A.6	SQUID electronics frequency response	148
B.1	Arrangement of coordinate systems in probe and images.	159
C.1	Detail of sample contacts	166
C.2	Detail of SQUID contacts	166

Chapter 1

Introduction

1.1 The Meissner effect

Superconductors are characterized by an extremely interesting suite of magnetic properties. Meissner and Oschenfeld first described superconductors as perfect diamagnets; a superconductor will develop a magnetization to oppose any magnetic field applied to it [1]. Screening currents which develop around the outside of the superconductor cause this magnetization. However, there is an upper bound on the amount of current that a superconductor may carry, the critical current density J_c . When the current density in a superconductor reaches this critical current density, superconductivity ceases and the superconductor becomes a normal metal. A sufficiently large magnetic field, known as the critical field H_c , may be applied to cause a superconductor to become a normal metal. In the simplest picture, this happens when the induced screening currents exceed J_c .

It was later discovered that, for certain materials, a superconductor would act as a Meissner diamagnet up to an external field H_{c1} but would then admit magnetic flux in quantized units known as vortices. For $H > H_{c1}$ the superconductivity is preserved until the external field increases to a still higher second

critical field, H_{c2} , where the superconductivity is destroyed. While in the Meissner state, *i.e.* below H_{c1} , the magnetization of the superconductor is reversible.

Above H_{c1} the magnetization is typically no longer reversible. This irreversibility arises due to mechanisms that trap vortices in the superconductor, *i.e.* pinning, or some mechanism which provides a barrier to flux entry and exit, *i.e.* the geometrical barrier [2] or the Bean-Livingston barrier [3]. Once vortices are introduced into the superconductor, the physical properties change quite dramatically: the superconductor may not carry transport current without loss and there may be strong non-linearities in the superconductor's AC response.

1.2 Types of superconductors

Two generic categories describe superconductors: type I and type II. As discussed above, a type I superconductor does not allow vortices to penetrate and has only one critical field, H_c while a type II superconductor will allow vortices to penetrate and has two critical fields, H_{c1} and H_{c2} .¹

Superconductors can also be loosely categorized by their transition temperature. The low T_c superconductors were known first and are often elemental, *i.e.* mercury, niobium, aluminum, etc., or metal alloys with T_c up to about 24 K. The high T_c superconductors are the cuprate materials, which were discovered in the 1980's. The cuprate superconductors may have transition temperatures much higher than the low T_c materials, up to about 150 K. The theory of Bardeen Cooper and Schreiffer (BCS) [5] explains the phenomena of superconductivity in low T_c materials but seems to fail to adequately describe the nature of supercon-

¹for a more complete description, see Tinkham [4], p. 134.

ductivity in the high T_c materials.

The phenomenological Ginzburg-Landau theory [6] describes the normal metal-superconducting transition by means of a complex order parameter,

$$\Psi(\vec{r}) = |\Psi(\vec{r})| e^{i\varphi(\vec{r})}. \quad (1.1)$$

The original BCS theory said that the symmetry of Ψ is spherical or of the so-called s -wave type. There are numerous proposed theories for high T_c superconductors, which give different predictions for the symmetry of $\Psi(\vec{r})$, so a measurement of the symmetry of $\Psi(\vec{r})$ can provide insights into the nature of high T_c superconductivity. As will be discussed later in this thesis, measurements of the magnetic properties may yield valuable clues into the symmetry of the order parameter.

1.3 Structure of the thesis

This thesis is organized into chapters detailing different aspects of my work. This introductory chapter is designed to highlight what is well known about the magnetic properties of superconductors and how that knowledge of magnetic properties relates to what is known about the fundamental nature of superconductivity. Chapter 2, *Josephson-junction arrays as models of multiply connected superconductors*, discusses why Josephson-junction arrays are particularly useful for experimentally studying different magnetic phenomena, and describes numerical models for studying and interpreting magnetic phenomena seen in arrays. Chapter 3, *Paramagnetic Meissner effect in Josephson-junction arrays*, discusses our experimental observation of the paramagnetic Meissner effect using a scanning SQUID microscope (SSM) to measure Josephson-junction arrays. Chapter 4, *A*

model of the paramagnetic Meissner effect in multiply-connected superconductors, describes a model which captures all of the important features of the paramagnetism in Josephson-junction arrays. This model is applicable to any multiply-connected superconductor. Chapter 5, *Magnetic penetration into $\text{YBa}_2\text{Cu}_3\text{O}_{7-\delta}$ thin films*, describes recent experiments using the SQUID microscope to observe the magnetic flux penetration into YBCO thin films, both in the Meissner state and in the critical state. Here we also discuss the special Rolled Annealed Biaxially Textured Substrate (RABiTSTM)² from Oak Ridge National Labs, and their potential applications for long superconducting wires. Chapter 6, *Prospective*, discusses some of the interesting phenomena which we observed, but chose not to pursue, in favor of the work discussed. The purpose of this chapter is to explain to others what might be interesting and fruitful future work.

The appendix of this thesis consists primarily of a technical description of the experimental apparatus as well as the experimental technique. This is meant to serve as a source of documentation for many of the parts of the experiment, particularly the computer program which controls the scanning mechanism and data acquisition system.

²RABiTS is a registered trademark of Oak Ridge National Laboratory.

Chapter 2

Josephson-junction arrays as models of multiply-connected superconductors

2.1 Introduction

A typical sample of superconductor takes one of two general forms, a single crystal, or a polycrystal. Single crystals do not have grain boundaries and by studying them we may learn many of the intrinsic superconducting properties. However, only small single crystals can be grown. This poses a problem industrially and experimentally. In industry, material must be manufactured in quantity (*e.g.* for wires) and fabricated into devices (*e.g.* Josephson junctions) which cannot easily be done with a single crystal. Experimentally, samples often need to be fabricated in a particular fashion which may be very difficult or impossible to do with a single crystal.

Photolithographic techniques make thin film samples ideal candidates for study because samples may be fabricated of arbitrary geometry. The use of thin films adds several wrinkles to the study of superconductors. Thin films are polycrystalline and typically composed of randomly oriented grains. In high

T_c superconductors these grains can be quite disruptive, acting as Josephson junctions while in low T_c the grain boundaries may not matter at all to the current flow. The grain boundaries behave as Josephson junctions—two islands of superconductor joined by a weak link. Depending upon deposition conditions, superconducting grains may be randomly oriented and it may be difficult to disentangle which sample properties result from granularity and which result from island properties.

Josephson-junction arrays are the quintessential multiply-connected superconductor. They can be photolithographically realized and the equations that govern Josephson-junction arrays are simple and well known.¹ Because of the control that photolithography gives over sample fabrication, Josephson-junction array samples may provide important insight into the properties of granular superconductors. By proper choice of Josephson-junction array design one may create samples to study the interrelationship between geometry and material parameters of multiply-connected superconductors.

2.2 Single plaquette of Josephson-junction array

Before analyzing the entire array in detail, I consider the constitutive elements of the array: superconducting islands joined by weak links, shown in Fig. 2.1. The simplest component of the array is a single plaquette, a loop, which for our arrays consists of four Josephson junctions, but in general may consist of N

¹See the review article by Newrock *et al.*[7] for a more complete discussion of Josephson junctions and Josephson-junction arrays.

Josephson junctions. By looking at a single loop we can begin to directly compare experiment and analytical results. By contrast a n entire array may only be solved numerically, even though the equations are known. Additionally, remnants of the single loop behavior may be seen at the level of the entire array [8, 9], so an understanding of the single-loop will be important to aid in understanding the entire array. Indeed the single-loop model has been used many times in the literature in an attempt to explain phenomena primarily associated with the paramagnetic Meissner effect [10, 11, 12, 13, 14].

2.2.1 RCSJ model

Fig. 2.2 shows the simple circuit model commonly used to model a single Josephson junction² This represents the so called Resistively and Capacitively Shunted Junction (RCSJ) model of a Josephson junction, with a capacitive channel resulting from the physical overlap between the two islands of superconductor and a resistive channel due to quasiparticle tunneling. The third channel, the \times , represents the Josephson channel which obeys the Josephson relations [15]

$$I = I_c \sin \gamma \quad (2.1)$$

$$V = \frac{\Phi_0}{2\pi} \frac{d\gamma}{dt} \quad (2.2)$$

in which I is the current through the junction, I_c is the critical current of the junction, V is the voltage across the junction and Φ_0 is the flux quantum. The parameter γ is the gauge-invariant phase difference across the junction, defined as

$$\gamma = \Delta\varphi - \frac{2\pi}{\Phi_0} \int \vec{A} \cdot d\vec{\ell} \quad (2.3)$$

²See Tinkham [4], p. 206 or Newrock *et al.*[7], p. 275.

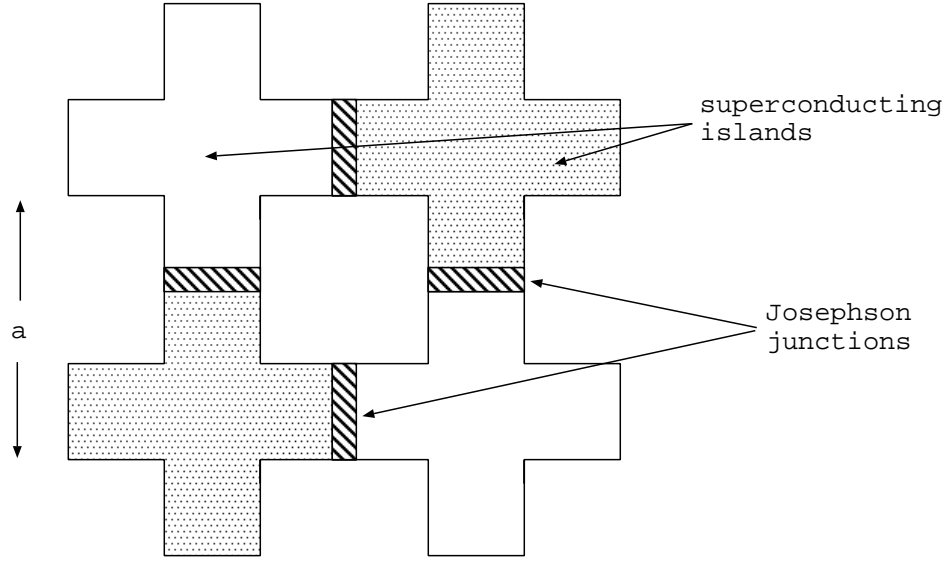


Figure 2.1: One plaquette of a Josephson-junction array. The cross shaped islands of superconductor are in two layers (white and speckled). At the cross overlap a junction is formed (cross-hatched region). The unit cell size is a .

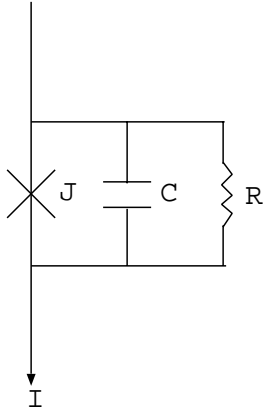


Figure 2.2: A schematic showing the various elements which go into modeling a single Josephson junction in the RCSJ model. The \times represents the Josephson element, while a resistive and a capacitive channel shunt the junction. The current through the junction would be measured as indicated.

where $\Delta\varphi$ is the difference in the phase of the superconducting order parameter across the junction, \vec{A} is the vector potential through the junction and the integral is taken from one side of the junction to the other. If the capacitance can be neglected the model reduces to the so-called Resistively Shunted Junction (RSJ) model.³

In the RCSJ model the current I through the junction, resistor and capacitor must obey

$$I = I_c \sin(\gamma) + \frac{1}{R} \frac{\Phi_0}{2\pi} \frac{d\gamma}{dt} + C \frac{\Phi_0}{2\pi} \frac{d^2\gamma}{dt^2} \quad (2.4)$$

where R is the quasi-particle or shunt resistance and C is the junction capacitance. Around a closed loop of superconductor, fluxoid quantization holds

$$\sum_j \gamma_j = 2\pi n - 2\pi \frac{\Phi}{\Phi_0} \quad (2.5)$$

in which j indexes each junction in the loop, n is the quantization number and Φ is the total flux Φ threading the loop. In addition the loop has a self inductance L which relates the total flux to the flux applied to the loop, Φ_{ext} ,

$$\Phi = \Phi_{\text{ext}} + LI \quad (2.6)$$

Here we have assumed that there is no external source of current, so I flows through each junction. To simplify we assume that by symmetry all N junctions in the loop are equivalent (we will discuss the asymmetric case in the section on unidentical junctions, section 2.2.6) so that

$$\gamma = \frac{2\pi}{N} \left(n - \frac{\Phi}{\Phi_0} \right). \quad (2.7)$$

For convenience we next transform our equations to a dimensionless form with

³See Tinkham [4] p. 202 or Newrock *et al.*[7] p. 275.

the substitutions [16]:

$$\begin{aligned}
\beta_\ell &= \frac{2\pi}{\Phi_0} L I_c \\
\beta_c &= \frac{2\pi}{\Phi_0} I_c R^2 C \\
\tau &= \frac{2\pi}{\Phi_0} I_c R t \\
i &= I/I_c \\
\phi &= \Phi/\Phi_0 \\
\phi_{\text{ext}} &= \Phi_{\text{ext}}/\Phi_0.
\end{aligned} \tag{2.8}$$

We apply these substitutions to (2.4)-(2.7) to obtain a single dimensionless equation,

$$\phi = \phi_{\text{ext}} + \frac{\beta_\ell}{2\pi} \left\{ \sin \left[\frac{2\pi}{N} (n - \phi) \right] - \frac{2\pi}{N} \frac{d\phi}{d\tau} + \left(\frac{2\pi}{N} \right)^2 \beta_c \frac{d^2\phi}{d\tau^2} \right\}, \tag{2.9}$$

which is a second order differential equation in time.⁴ The time evolution of γ and n can be quite complicated and will be discussed shortly.

The analysis of (2.9) proceeds in two different cases, that in which ϕ_{ext} is a constant or that in which ϕ_{ext} is a function of time. To relate to our experiments we will concern ourselves primarily with the former, where $d\phi_{\text{ext}}/d\tau = 0$. For the RSJ model the last term in (2.9) drops out, reducing the equation to a first order differential equation in time, greatly simplifying the analysis.

2.2.2 The meaning of the quantum number n

Before continuing further we must discuss the meaning and importance of the quantum number n . The importance of this cannot be over-stressed because there has been a tendency in the literature to ignore the quantum number by

⁴Eqn. (2.9) has no $dn/d\tau$ term because n is a discrete variable.

setting $n = 0$ (see *e.g.* Ref. [17]).⁵ Consider a solid loop of superconductor, at any given point, the value of the order parameter (*c.f.*(1.1)) must be single valued. This requires that

$$\oint \nabla \varphi \cdot d\vec{\ell} = 2\pi n, \quad (2.10)$$

with the integral taken around any closed path enclosing the center of the loop.⁶ If $n = 0$, φ remains unchanged after going around the loop. If $n \neq 0$, φ has changed by $2\pi n$ after going around the loop.

Now consider taking the solid superconducting loop and breaking it to add a Josephson junction. We have to modify (2.10) to take into account this break in the loop. After accounting for any flux in the loop we obtain

$$\gamma = 2\pi n - \frac{2\pi}{\Phi_0} \oint \vec{A} \cdot d\vec{\ell}, \quad (2.11)$$

the one-junction analog of (2.5).

One very interesting thing has happened: we have abstracted the quantum number away from a superconducting loop property to instead apply only to the gauge invariant phase difference across the *junction*. Suppose a single fluxoid enters the loop, one of two things can happen, n can increase by one or γ decreases by 2π . Either results in the same effect: balancing the increase in $\oint \vec{A} \cdot d\vec{\ell}$. The implication of this is clear for modeling the array: choose either $-\infty < \gamma < \infty$ and fix n , or limit $0 \leq \gamma < 2\pi$ and increment n whenever γ reaches its limits.

There are multiple equivalent ways to choose starting values of γ and n for a numerical model. Two equivalent starting values (primed and unprimed) will

⁵A useful discussion of the proper definition of n is given in the appendix of Ref. [18], which reaches similar conclusions to those drawn here, through slightly different means.

⁶This is not the rigorous definition, but serves for the present purpose (it is a special case) with minimal confusion.

always be related through

$$\begin{aligned} n' &= n - (\gamma \bmod 2\pi) \\ \gamma' &= \gamma - 2\pi n \end{aligned} \tag{2.12}$$

For example $n = 0$ and $\gamma = -2\pi$ is equivalent to $n' = 1$ and $\gamma' = 0$.

As we allow the model to evolve in time we now have the choice to fix n and allow γ total freedom, or restrict $0 < \Delta\gamma \leq 2\pi$ and increment n .

For a loop with more than one junction, things become somewhat trickier since the gauge invariant phase difference across each junction need not in general be the same (a point conveniently neglected in (2.7)), though the quantization rule, (2.5), must still be obeyed for the entire loop. To illustrate this point, consider the following scenario with symmetric junctions *à la* (2.7): $\beta_\ell \gg 1$, $N > 1$ and compare $n = 0$ and $n = 1$ for $\phi_{\text{ext}} = 0$. Different results occur, $\phi = 0$ or $\phi > 0$. *By fixing the value of n we cannot access all of the possible solutions.*

2.2.3 Time independent external field

To analyze (2.9) we perform the standard stability analysis [19] to find that steady state solutions take the form of

$$\phi = \phi_{\text{ext}} + \frac{\beta_\ell}{2\pi} \sin \left[\frac{2\pi}{N} (n - \phi) \right]. \tag{2.13}$$

The right hand side can result in either single or multiple solutions, depending upon the value of β_ℓ . The crossover point depends upon N , and the solutions are single-valued for $\beta_\ell < N$ and multi-valued for $\beta_\ell \geq N$. Fig. 2.3 shows (2.13) plotted for large $\beta_\ell = 30$ which demonstrates that for a given ϕ_{ext} there are many different solutions for ϕ possible. The solutions for different values of n

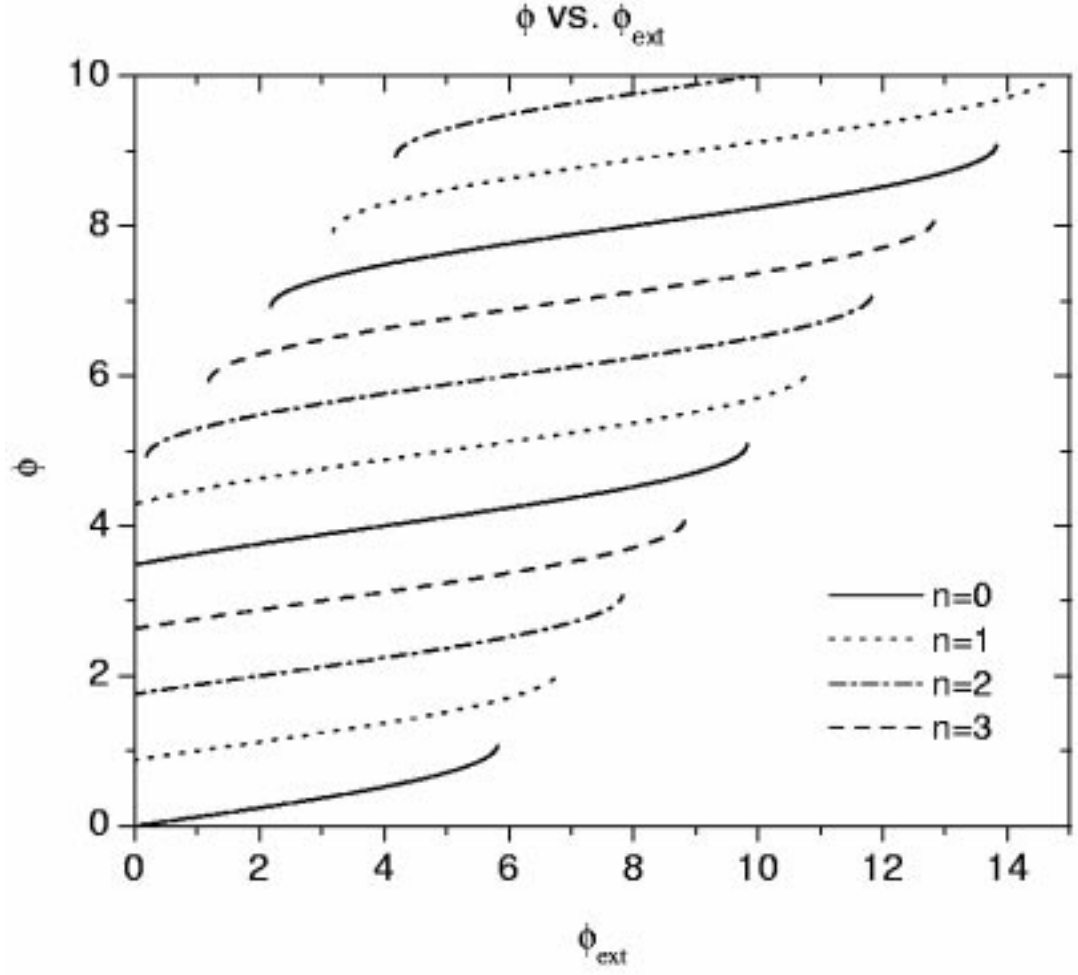


Figure 2.3: ϕ plotted against ϕ_{ext} from (2.13) for $\beta_\ell = 30$ and $N = 4$ for different values of the quantization number n .

are sometimes referred to as the different “branches” of the solution. For each of these branches, only the positively sloped parts are plotted, because these are the physically realizable solutions, which will be discussed below.

π -junctions

Another interesting possibility is the presence of an intrinsic phase shift in the order parameter across the junction. This phase shift may occur if *e.g.* the junction is formed from misaligned grains of a superconductor with *d*-wave symmetry. If the intrinsic phase shift across all the junctions sums to π , (2.13) becomes modified to

$$\phi = \phi_{\text{ext}} + \frac{\beta_\ell}{2\pi} \sin \left[\frac{2\pi}{N} (n - \phi) - \pi \right]. \quad (2.14)$$

This effect is commonly described as due to the presence of π -junctions. The important physical difference between (2.13) and (2.14) is that at $\phi_{\text{ext}} = 0$, (2.13) allows the loop to have zero magnetization while (2.14) forces the loop to be magnetized. These two cases have been confirmed experimentally in two junction SQUIDs [20, 21].

Instead of plotting ϕ *vs.* ϕ_{ext} as in Fig. 2.3 it is useful to also consider a plot of the normalized magnetization $\phi_{\text{mag}} = \phi - \phi_{\text{ext}}$ *vs.* ϕ_{ext} since it is the magnetization that is often measured experimentally. This is shown in Fig. 2.4. If we consider (2.13), immediately one important fact springs forth: the larger β_ℓ the steeper the magnetization curves. This implies that small variations in the external flux may create large variations in the total flux of the single loop. Furthermore, it is clear from Fig. 2.4 that the single loop is equally likely to be either paramagnetic or diamagnetic over the entire range of ϕ_{ext} .

Sigrist and Rice [13, 14] discussed the differences between (2.13) and (2.14)

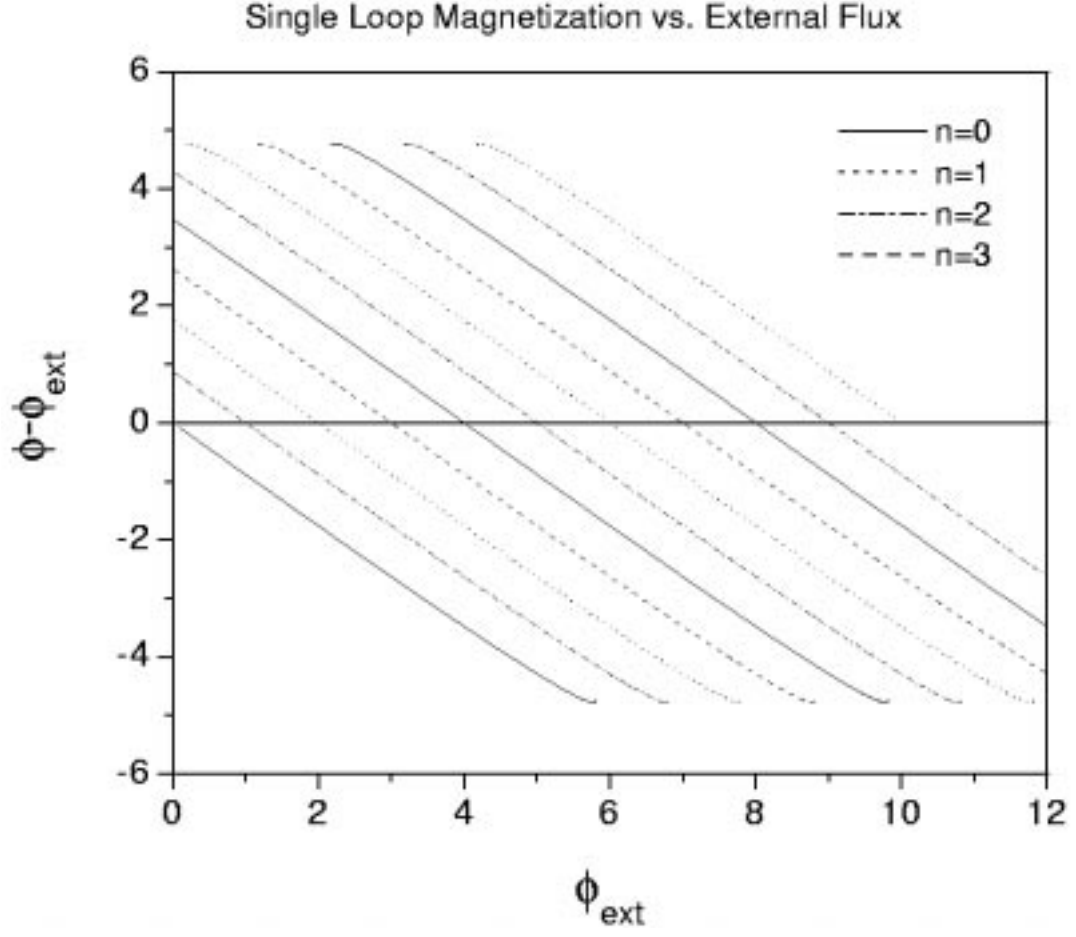


Figure 2.4: Normalized magnetization of a single loop, ϕ_{mag} , plotted against the external flux ϕ_{ext} applied to the loop for $\beta_{\ell} = 30$ and $N = 4$ for different values of the quantization number n .

vis-à-vis *s*-wave and *d*-wave superconductivity for $N = 1$ and concluded that observation of paramagnetism at $\phi_{\text{ext}} = 0$ provided evidence of a π -junction in the loop. However, they failed to account for the possibility that $\beta_\ell \gg N$ in (2.13) in which case there are possible paramagnetic (and diamagnetic) solutions for ϕ at $\phi_{\text{ext}} = 0$ even in the absence of π -junctions.

(2.13) does not tell the entire story. For $\beta_\ell > N$ it specifies a multivalued solution with both positive and negative slope. The solutions with positive slope are seen experimentally, while those with negative slope are never seen. This can be understood by continuing the stability analysis of (2.9).

In the case of the RSJ model, (2.9) reduces to

$$\phi = \phi_{\text{ext}} + \frac{\beta_\ell}{2\pi} \left\{ \sin \left[\frac{2\pi}{N}(n - \phi) \right] - \frac{2\pi}{N} \frac{d\phi}{d\tau} \right\} \quad (2.15)$$

whose Jacobean has a single eigenvalue⁷ of

$$\lambda = -\frac{N}{2\pi} \left\{ \frac{2\pi}{\beta_\ell} + \frac{2\pi}{N} \cos \left[\frac{2\pi}{N}(n - \phi) \right] \right\} \quad (2.16)$$

For $\beta_\ell < N$, λ will always be negative, hence any direction in ϕ from (2.9) is a stable direction. This means that the loop can settle into any value of ϕ for a given ϕ_{ext} which solves (2.15). Additionally, the solution to (2.15) is single valued, so there is no ambiguity as to the state of the loop.

In the case when $\beta_\ell > N$, λ may change sign depending upon the particulars of the situation and λ will be negative for

$$\cos \left[(n - \phi) \frac{2\pi}{N} \right] > -\frac{N}{\beta_\ell}. \quad (2.17)$$

For $\lambda < 0$ the directions from the fixed point solutions are stable directions so that the loop will stay in such a configuration. When $\lambda > 0$ the directions are

⁷For a complete discussion of the stability analysis, see Ott [19], p. 108.

unstable; should any small thermal fluctuation occur, a loop on the unstable fixed point solution will leave, and be driven even further from the unstable solution.

To illustrate this point, consider the first time derivative of (2.15),

$$-\left\{1 + \frac{\beta_\ell}{N} \cos \left[(n - \phi) \frac{2\pi}{N} \right] \right\} \frac{d\phi}{d\tau} = \frac{\beta_\ell}{2\pi} \frac{d^2\phi}{d\tau^2} \quad (2.18)$$

which takes the form of a moving particle experiencing a drag force. The “drag coefficient”

$$-\left\{1 + \frac{\beta_\ell}{N} \cos \left[(n - \phi) \frac{2\pi}{N} \right] \right\}$$

takes a special form that is dependent upon ϕ , the position variable. Additionally, the drag coefficient changes sign: Instead of exerting drag, and slowing the particle, it pushes the particle and accelerates it away from ϕ . Conversely, when the drag coefficient is negative, the particle slows toward ϕ . The condition for this switch over occurs at exactly the same place as the switch over described for the eigenvalues above.

In the case of the RCSJ model, including β_c in (2.13), makes the eigenvalues of the Jacobean more complicated, but the same underlying behavior given by (2.17) occurs. The difference is that now while solutions are still attracting or repelling, there are two types, depending on whether or not the eigenvalues are complex or real. The eigenvalues themselves are given by

$$\lambda_{\pm} = \frac{N}{4\beta_c\pi} \pm \frac{N}{4\beta_c} \sqrt{1 + 8\pi \frac{\beta_c}{\beta_\ell} + 2\pi\beta_c \cos \left(\phi \frac{2\pi}{N} \right)} \quad (2.19)$$

The eigenvalues will be purely real when

$$\cos \left[(n - \phi) \frac{2\pi}{N} \right] > -\frac{1}{2\pi\beta_c} - \frac{N}{\beta_\ell}. \quad (2.20)$$

For sufficiently small β_ℓ and β_c the eigenvalues will always be real and there will only be stable directions to the fixed point. Additionally (2.20) reduces to the

previous results for over damped junctions, if $\beta_c \rightarrow 0$. For large enough β_ℓ and β_c the fixed point solutions will have two unstable directions. There is a range in between these two possibilities in which the fixed point solutions have one stable and one unstable direction. The unstable direction always dominates in (2.19) and the fixed point is a repulsor.

2.2.4 Time-dependent external field

The single loop may also be put into a time-varying external field. The simplest case which may be considered, and the only case considered here, is that of a sinusoidal driving field

$$\phi_{\text{ac}}(\tau) = \phi_{\text{ext}} \sin(\omega\tau) \quad (2.21)$$

We can substitute (2.21) for ϕ_{ext} in to (2.9) and then analyze the result in different cases. It is useful to make the definition

$$\omega_0^{-2} = \frac{\pi}{8} \beta_\ell \beta_c, \quad (2.22)$$

where ω_0 corresponds to the dimensionless natural frequency of the system if the non-linear Josephson-junction term is ignored. To see why this definition of ω_0 is useful, consider rewriting (2.9) in the form

$$\frac{\pi}{8} \beta_\ell \beta_c \frac{d^2 \phi}{d\tau^2} = -\phi + \phi_{\text{ext}} \sin(\omega\tau) - \frac{\beta_\ell}{4} \frac{d\phi}{d\tau} + \frac{\beta_\ell}{2\pi} \sin \left[(n - \phi) \frac{2\pi}{N} \right] \quad (2.23)$$

which is clearly the form of a forced, damped harmonic oscillator with an additional non-linear term.

Quasi-static case

The quasi-static case is associated with $\phi_{\text{ext}} \ll \beta_\ell/2\pi$ and $\omega \ll \omega_0$. In this case the solutions are basically what we expect for the static case. The system

is driven so slowly and with such low amplitude that it is always essentially in equilibrium.

Large driving amplitude

An interesting situation occurs when $\phi_{\text{ext}} \gg \beta_\ell/2\pi$. Here ϕ_{ext} drives the loop so hard that the non-linear term is irrelevant. This case corresponds to the loop responding simply as a harmonic oscillator.

2.2.5 Gibbs free energy of single loop stable solutions

Assuming that the loop is able to achieve thermodynamic equilibrium (which we have not generally assumed) the most favorable solution given by (2.13) would be the solution with the lowest Gibbs free energy. The Gibbs free energy in this case is $dG = -Id\Phi_{\text{ext}}$ [22, 23] which is easily determined numerically. This yields a series of Gibbs free energies for each possible solution to (2.13), with the lowest Gibbs free energy corresponding to the solution which has ϕ closest to ϕ_{ext} . For the ϕ *vs.* ϕ_{ext} curves in Fig. 2.3 with $\beta_\ell = 30$, the Gibbs free energy curves are plotted in Fig. 2.5.

2.2.6 Non-identical junctions

If we ignore the symmetry arguments which resulted in (2.9) then for N junctions in an isolated loop, for we will have N equations to solve. For each junction, (2.6) implies

$$\phi = \phi_{\text{ext}} + \frac{\beta_{\ell_i}}{2\pi} \sin \gamma_i \quad (2.24)$$

in which β_{ℓ_i} is the β_ℓ parameter of the individual junction, and accounts for individual junction variations in I_c in the static case. In addition, the quantization

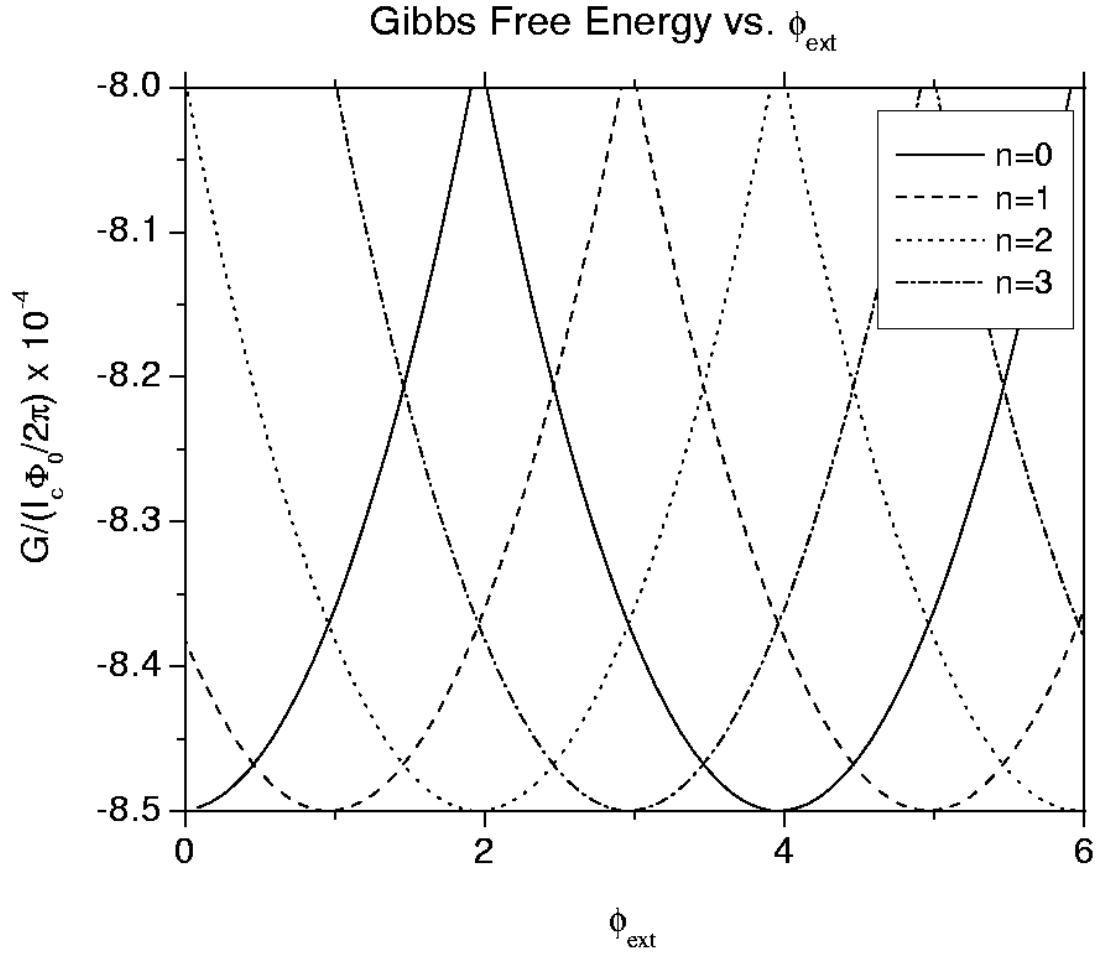


Figure 2.5: Gibbs free energy calculated for a four-junction loop with $\beta_\ell = 30$.

rule, (2.5), still holds. We now substitute (2.24) for ϕ to arrive at an equation for each junction,

$$n - \phi_{\text{ext}} - \frac{1}{2\pi} \sum_i \gamma_i - \frac{\beta_{\ell_i}}{2\pi} \sin \gamma_i = 0. \quad (2.25)$$

The system must be solved numerically. If one of the β_{ℓ_i} is much larger than the others, then the loop behaves primarily as a loop with $N - 1$ junctions. For variance in β_{ℓ_i} on the order of 10%, there is little change in the outcome, compared to the results for the symmetric loop. This means that experiments on loops or Josephson-junction arrays with critical current variations on the order of 10% or less should exhibit behavior similar to a uniform loop or array. Furthermore, models incorporating uniform critical currents are significantly easier to implement.

This is significant because if small variations do not affect the results very much, then we expect that for a real Josephson-junction array variations in the junction parameters on the order of 10% will have only a small bearing on the observations of those arrays.

2.3 Complete model of entire array

To study the entire array, we take the same basic equations which describe a single loop and scale them up. In this section we will consider a generic square lattice of $N \times M$ Josephson junctions, as depicted in Fig. 2.6. Josephson junctions in the vertical wires⁸ of the array are described by gauge-invariant phase difference $\theta_{j,k}$ and in the horizontal wires by $\gamma_{j,k}$, while $I_{j,k}$ describes the loop current flowing

⁸The wires of the array are often referred to as “branches,” while the loop currents are sometimes referred to as “mesh” currents.

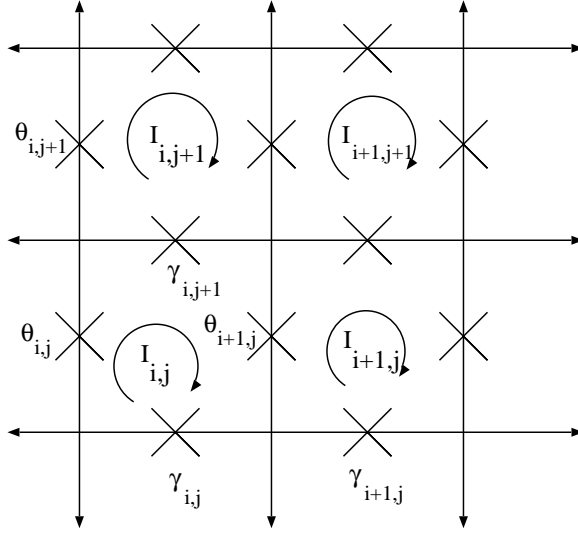


Figure 2.6: Schematic arrangement for a square lattice Josephson-junction array showing the variables used to describe each plaquette and junction in the array. The positive direction for the loop currents are clockwise, as indicated by the arrows, positive $\theta_{i,j}$ and $\gamma_{i,j}$ are measured in the vertical and horizontal direction respectively.

around each plaquette in the array. Considering loop currents simplifies the analysis by eliminating the need to consider Kirchhoff's laws at each intersection point of the array. For simplicity, consider here that the junctions are identical. With this arrangement, we may write an equation describing the current through each junction, using the normalizations from the single loop case,

$$i_{j,k} - i_{j,k-1} = \sin \gamma_{j,k} + \frac{d\gamma_{j,k}}{d\tau} + \beta_c \frac{d^2 \gamma_{j,k}}{d\tau^2} \quad (2.26)$$

$$i_{j,k} - i_{j-1,k} = \sin \theta_{j,k} + \frac{d\theta_{j,k}}{d\tau} + \beta_c \frac{d^2 \theta_{j,k}}{d\tau^2} \quad (2.27)$$

as well as a quantization condition for each loop of the array,

$$\theta_{j,k} + \gamma_{j,k+1} - \gamma_{j,k} - \theta_{j+1,k} = 2\pi n_{j,k} - 2\pi \phi_{j,k}. \quad (2.28)$$

To fully define the array requires one further relation, the total flux $\Phi_{i,j}$ threading the i, j plaquette,

$$\phi_{j,k} = \phi_{\text{ext}} + \frac{\beta_\ell}{2\pi} \sum_{j',k'} m_{j,k,j',k'} \phi_{j',k'} \quad (2.29)$$

in which $m_{j,k,j',k'}$ is the mutual induction matrix between plaquette (j, k) and (j', k') normalized to the self-inductance of a single plaquette, L .

The system detailed in Eqns. (2.26) to (2.29) may also be condensed into a Hamiltonian

$$\mathcal{H} = \frac{1}{2} \beta_\ell \sum_{j,k} m_{j,k,j',k'} \phi_{j,k} i_{j,k} + \sum_{j,k} (1 - \cos \gamma_{j,k}) + \sum_{j,k} (1 - \cos \theta_{j,k}), \quad (2.30)$$

where \mathcal{H} is normalized to $\Phi_0 I_c / 2\pi$. The sum in the first term is taken over each plaquette in the array while the sums in the final two terms are taken over each junction in the array. This Hamiltonian will later be useful for investigating the energy landscape of the array.

There have been many approaches to the solution of these equations [8, 24, 25, 26, 27, 28] but perhaps the most important result for the discussion here stems

from work by Phillips *et al.*[29] in which they show the importance of utilizing the full mutual induction matrix in order to achieve accurate results.

2.3.1 Mutual induction matrix

Because the full-induction matrix is just a geometrical property of the array it can in principle be computed. Phillips *et al.* put forth one method to do this, on which this discussion will be based. There are two cases to consider when computing the matrix, the near field, in which the physical extent of the plaquettes must be accounted for, and the far field, in which the plaquettes behave as current loops composed of infinitesimal wires.

Near field

We begin by modeling the array as a series of blocks (see Fig. 2.7(a)) and making the assumption that the current density is uniform throughout the blocks. Each block has a uniform cross-sectional area a . The mutual induction matrix is then,

$$M_{j,k,j',k'} = \frac{1}{a^2} \frac{\mu_0}{4\pi} \oint \oint d\ell_{j,k} d\ell_{j',k'} \int_A \int_{A'} \frac{da_{j,k} da_{j',k'}}{|\vec{r}_{j,k} - \vec{r}_{j',k'}|} \quad (2.31)$$

which follows simply from Faraday's Law.⁹ The integrals $\oint d\ell$ are taken around the two plaquettes of interest, the integrals $\int_A da$ are taken over the facial area of each block in the integration and μ_0 is the magnetic constant. (2.31) cannot in general be integrated analytically, but can be integrated numerically for the plaquettes of interest.

⁹A very clear discussion is given in Ramo, Whinnery and van Duzer[30], pp. 187-189.

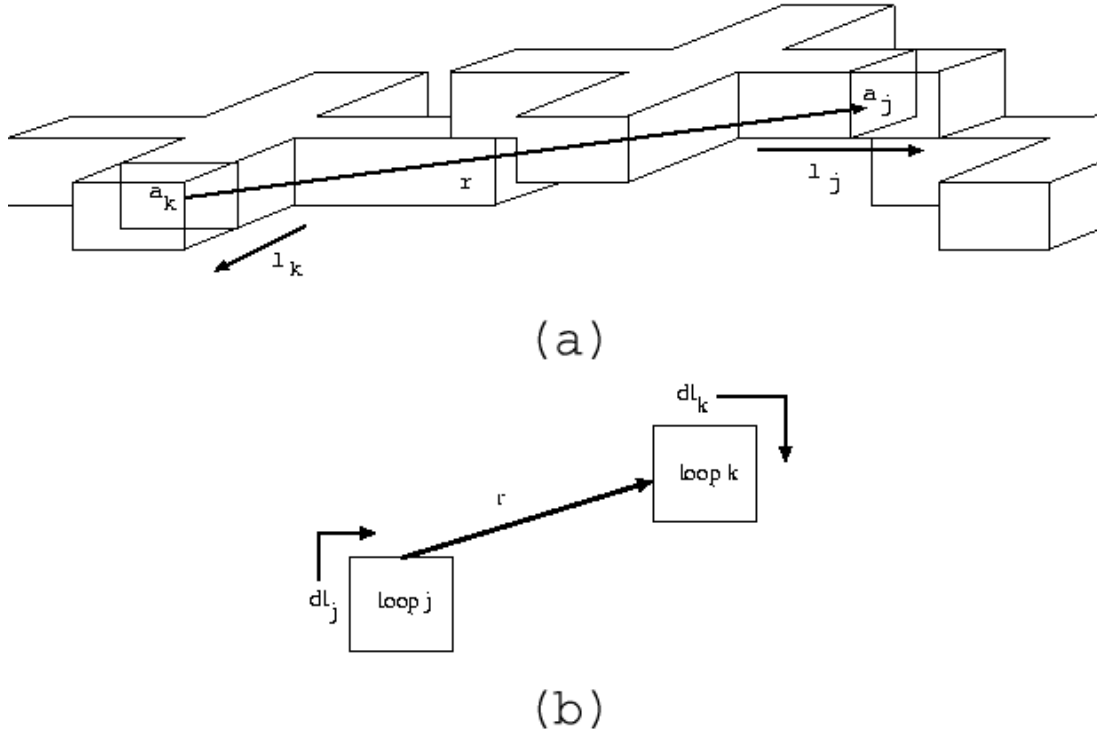


Figure 2.7: Schematic of the block arrangement used to compute the mutual induction matrix. (a) indicates the arrangement used for the near field, with a_i representing the face of the block being integrated over, ℓ_i representing the length around the loop integrated over, and r representing the radius vector between the two blocks in the integration. (b) indicates the arrangement used to compute the mutual inductance in the far field. r represents the radius vector between the two loops and $d\ell_i$ represents the direction of the integration around each loop.

Far field

In the far field (2.31) simplifies greatly to, as shown in Fig. 2.7(b),

$$M_{j,k,j',k'} = \frac{\mu_0}{4\pi} \frac{16\sqrt{p}}{\sqrt{(j-j')^2 + (k-k')^2}}, \quad (2.32)$$

in which p is the area of the plaquette, which may be computed in a straightforward manner.

It is complicated to compute the mutual induction matrix, but for a given problem we only need to compute the mutual induction matrix once.

Chapter 3

Paramagnetic Meissner effect in Josephson-junction arrays

3.1 Introduction

Type I superconductors traditionally behave as perfect diamagnets; this is the Meissner effect, first described by Meissner and Ochsenfeld [1] in 1933. This means that the magnetic induction \vec{B} inside a superconductor is always zero. Consequently the magnetization of a superconductor in a magnetic field \vec{H} is given by (in MKS units)

$$\vec{M} = -\vec{H}. \quad (3.1)$$

In general, perfect diamagnetism holds true up to a certain critical field H_c at which the superconductor turns into a normal metal.

3.1.1 Paramagnetic Meissner effect in high T_c superconductors

Recently, experiments by Braunisch *et al.* [31, 32] demonstrated that the superconductor $\text{Bi}_2\text{Sr}_2\text{CaCu}_2\text{O}_y$ (BSCCO) could be paramagnetic. This effect has

variously been referred to as the “paramagnetic Meissner effect” (PME) or the “Wohleben effect.” The former has become accepted and will be used here. It was further argued, following the work of Sigrist and Rice [13, 14], that this paramagnetism provided evidence for d -wave superconductivity in BSCCO. We discussed in section 2.2.3, p. 14 that a π -junction may cause a superconducting loop to have a paramagnetic moment. A π -junction would result from grain misalignment in a superconductor with a d -wave order parameter. After the publication of Braunisch *et al.*, others began to report paramagnetism in high T_c superconductors. For example, Reidling *et al.* reported PME in $\text{YBa}_2\text{Cu}_3\text{O}_{7-\delta}$ [33]; Schliepe *et al.* in BSCCO [34]; Önbaslı *et al.* in $\text{HgBa}_2\text{Ca}_2\text{Cu}_3\text{O}_x$ (HgCCO) [35]; and Okram *et al.* in $\text{Nd}_{2-x}\text{Ce}_x\text{CuO}_y$ (NCCO) [36].

3.1.2 Paramagnetic Meissner effect in low T_c superconductors

The continuing reports of PME solely in high T_c materials bolstered the belief that PME resulted from d -wave superconductivity, until the report of PME in conventional thick niobium disks by Thompson *et al.* [37], by Kostić *et al.* [38] and later in niobium thin films by Terentiev *et al.* [39]. Further Geim *et al.* [40] reported PME in mesoscopic aluminum disks. Since niobium and aluminum are known to be s -wave, this discredited the d -wave explanation for PME and caused a public controversy.¹

We measured $\text{Nb} - \text{Al}_2\text{O}_3 - \text{Nb}$ Josephson-junction arrays in order to investigate this controversy.² It is well known that niobium Josephson-junction

¹See Ref. [37] and the post-publication comments in Ref. [41] and Ref. [42].

²The research results of this work on PME in Josephson-junction arrays have lead to several

arrays have no π -junctions. Additionally Josephson-junction array fabrication takes place lithographically so we have great control over the design of the sample. Highly ordered samples can be made photolithographically in contrast to many of the granular high T_c samples. This makes our defect occurrence, *e.g.* J_c variations, no more than 10%. Additionally, measurements of AC susceptibility by Araujo-Moreira *et al.* [11] and Barbara *et al.* [12] demonstrated that Josephson-junction arrays might exhibit PME.

3.2 Our samples

The Josephson-junction array samples discussed here were fabricated at Westinghouse[46] by Martin Forrester and consist of unshunted Nb – Al₂O₃ – Nb Josephson junctions in arrays of 30×100 and 100×150 Josephson junctions.³ The array design is the same as described in the previous chapter (chapter 2, p. 6, Fig. 2.1). An optical micrograph of a few unit cells of the array is shown in Fig. 3.1. The unit cell size of each array is $46 \mu\text{m}$ with a wire width of $10 \mu\text{m}$. The niobium film is 200 nm thick and patterned into two layers of crosses. At the cross overlap a Josephson junction of $5 \mu\text{m}$ by $5 \mu\text{m}$ is formed. The calculated self-inductance of each loop of four junctions is $L = 64 \text{ pH}$ and the measured critical current density at 4.2 K is $J_c = 600 \text{ A/cm}^2$.⁴ The unit cell size is comparable to the typical grain size seen in BSCCO samples [31, 32, 48] which exhibit PME.

publications, Refs. [43, 44, 45, 9].

³The arrays come from batches 10 and 11 and are designated JJA-10-30 for the 30×100 and JJA-11-150 for the 100×150 .

⁴See Ref. [47] for a discussion of the self-inductance in this case.

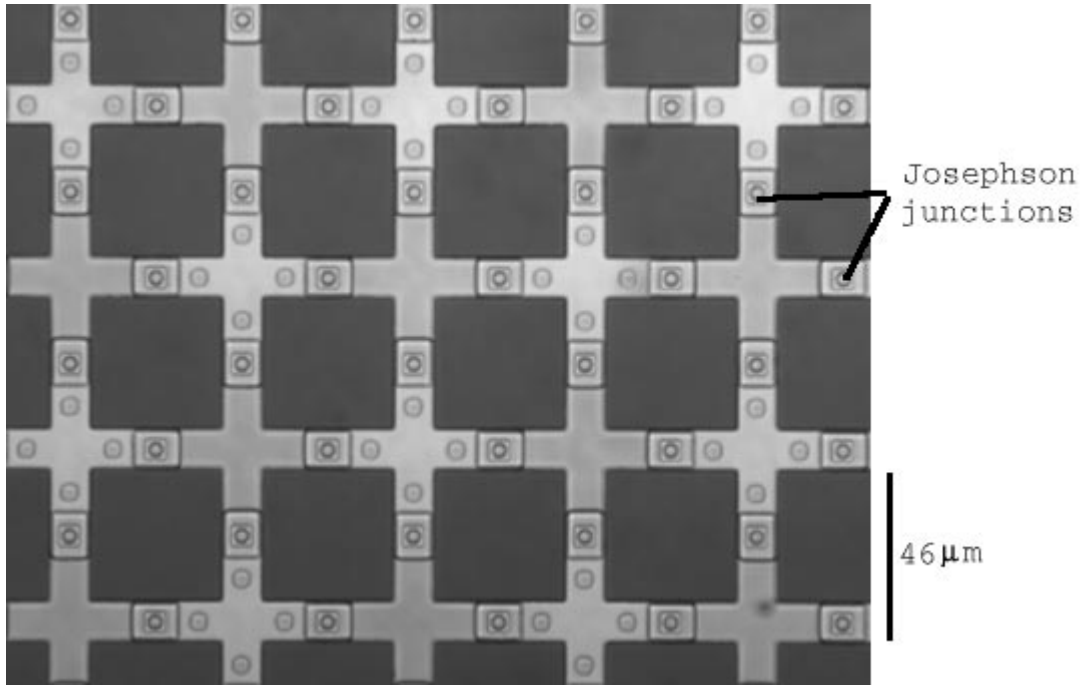


Figure 3.1: Optical micrograph of several unit cells of the array showing the crosses and locations of Josephson junctions. The unit cell size is $46\text{ }\mu\text{m}$ and the wires are $10\text{ }\mu\text{m}$ across.

3.3 Experimental technique

Kirtley *et al.* [48] used a scanning SQUID microscope (SSM), described in Ref. [49], to image the BSCCO samples from Braunisch *et al.* [31, 32] and investigate the spatial distribution of paramagnetism in paramagnetic-superconducting BSCCO. This elegant experiment provided inspiration for our work.

Our SSM has improvements over Kirtley’s that make it ideally suited to this type of experiment.⁵ Our probe has a larger scanning range, as well as thermal isolation between the SQUID and the sample (since they are not in direct contact). Kirtley *et al.* were unable to scan to the edges of their sample, due to scanning stage restrictions. We are able to scan over our entire sample, which proved to be crucial to our analysis of the origin of PME.

The benefits of the SSM over more conventional magnetic measurement techniques are legion. The primary benefits arise from the fact that the measured data are spatially resolved and the measurable field strengths are so low. Theories of PME provide forms for the flux distribution near the edges;⁶ experimental verification of these theories requires measurements of spatially-resolved magnetization. Other experimental techniques such as scanning Hall probe microscopy or Magneto-Optical Indicator Films (MOIF) may be used to provide spatially resolved information. However, both Hall probes and MOIF are not sensitive to the magnetic field levels of interest in our arrays. One flux quantum per unit cell of the array has an average magnetic field of 10^{-3} G and we will typically measure signals on the order of fractions of a single flux quantum.

To run the experiment, Josephson-junction array samples are placed on the

⁵For a description of the experimental probe see appendix A.

⁶Theories of PME are discussed in the introductory material to chapter 4.

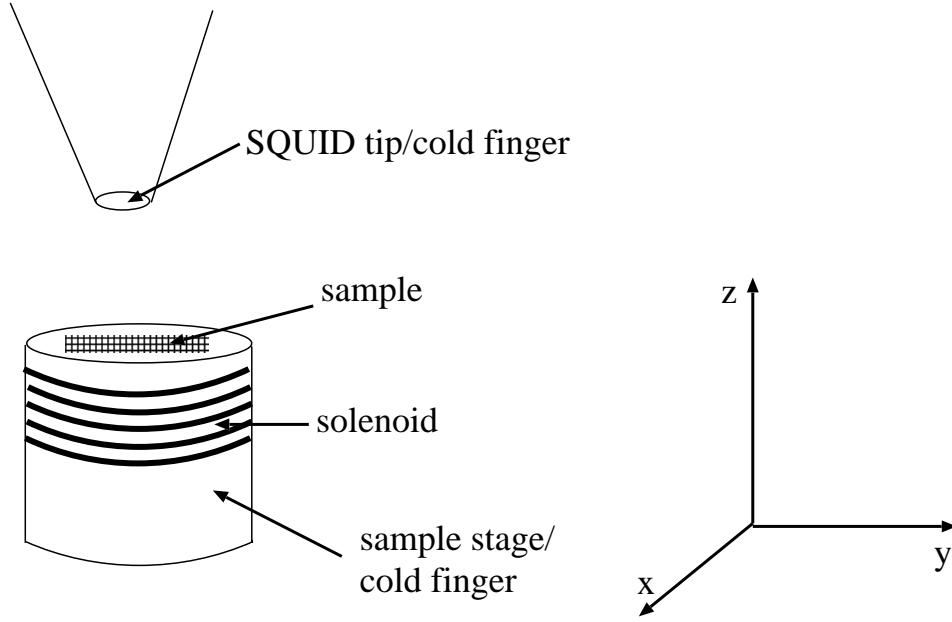


Figure 3.2: Experimental arrangement of sample Josephson-junction array and SQUID at the cold end of the scanning SQUID probe. The sample moves in x and y under the SQUID. Output signal from the SQUID is measured point by point as the sample is scanned to generate an image of the magnetic induction over the sample. The SQUID-sample separation is generally around $50\text{ }\mu\text{m}$.

end of the cylindrical sample stage cold finger, as shown in Fig. 3.2. The cold finger is a 10 mm diameter sapphire rod around which a solenoid is wound. This solenoid provides the external flux Φ_{ext} to the sample.

Prior to any measurement, the SQUID is adjusted to insure that no flux is pinned in the body. This is accomplished by first thermal cycling the SQUID to remove trapped flux. The SQUID is then scanned over a superconducting sample (a technique developed in Ref. [20]) to observe if there is still flux trapped in the SQUID, noting the sample response as the SQUID is moved over the sample. Eliminating the flux in the SQUID minimizes the interaction between the SQUID and the sample and eliminates false signals that may result from sample response to flux in the SQUID.

With the system cold, we cannot easily know precisely how far apart the SQUID and the sample are. To insure the SQUID does not collide with the sample, we rely on clues from the processed data. Sadly, many samples were lost due to the fact that the probe provides no means to measure the separation *in situ*. For a typical scan discussed here, the SQUID – sample separation is between 40 and 60 μm . We infer this because the lattice of the array is 46 μm and we can just begin to resolve array features in the data at this separation. For our purposes we do not need to have unit cell resolution of the array, nor will the exact measure of the SQUID – sample separation affect the results.

After flux is removed from the SQUID, the sample is moved so that the SQUID is far away (greater than 10 mm, in x and y , not z) in order to avoid any possible interference between the SQUID and the sample during field cooling. Fig. 3.11 shows the effect of zero field cooling the sample with the SQUID positioned over the middle of the 30×100 Josephson-junction array. Flux became trapped in

the sample in a similar pattern to the wire arrangement on the surface of the SQUID tip, *c.f.* Fig. A.4. It was found that turning off the SQUID, field cooling and then reactivating the SQUID tended to trap flux in the sample when the feedback circuit was adjusted. To avoid this problem the SQUID was moved far away from the sample until it had no noticeable effect when the sample was zero field cooled.

In practice, I begin taking measurements by heating the sample above $T_c = 9.2\text{ K}$ to 13 K . We then apply an external flux to the sample and remove the heat source. The sample cools in field to 4.2 K and the measurement begins.

Each measurement of a magnetization image consists of four scanning passes of the SQUID over the sample in different situations. Each scanning pass produces an image of the flux threading the SQUID at a particular point in space above the sample. Fig. 3.3 through Fig. 3.6 shows representative images of the four scanning passes made over the sample to produce the magnetization image. We wish to compute the magnetization of the sample. In MKS units,

$$\vec{M} = \left(\vec{H} - \frac{1}{\mu_0} \vec{B} \right). \quad (3.2)$$

The magnetization vector \vec{M} can be related to a flux through an area

$$\Phi_{\text{mag}} = \mu_0 \int_A \vec{M} \cdot d\vec{a} \quad (3.3)$$

just as \vec{B} and \vec{H} are associated with a flux through a particular area

$$\Phi = \int_A \vec{B} \cdot d\vec{a} \quad (3.4)$$

$$\Phi_{\text{ext}} = \mu_0 \int_A \vec{H} \cdot d\vec{a}. \quad (3.5)$$

so that (3.2) can be expressed in terms of flux

$$\Phi_{\text{mag}} = \Phi - \Phi_{\text{ext}}. \quad (3.6)$$

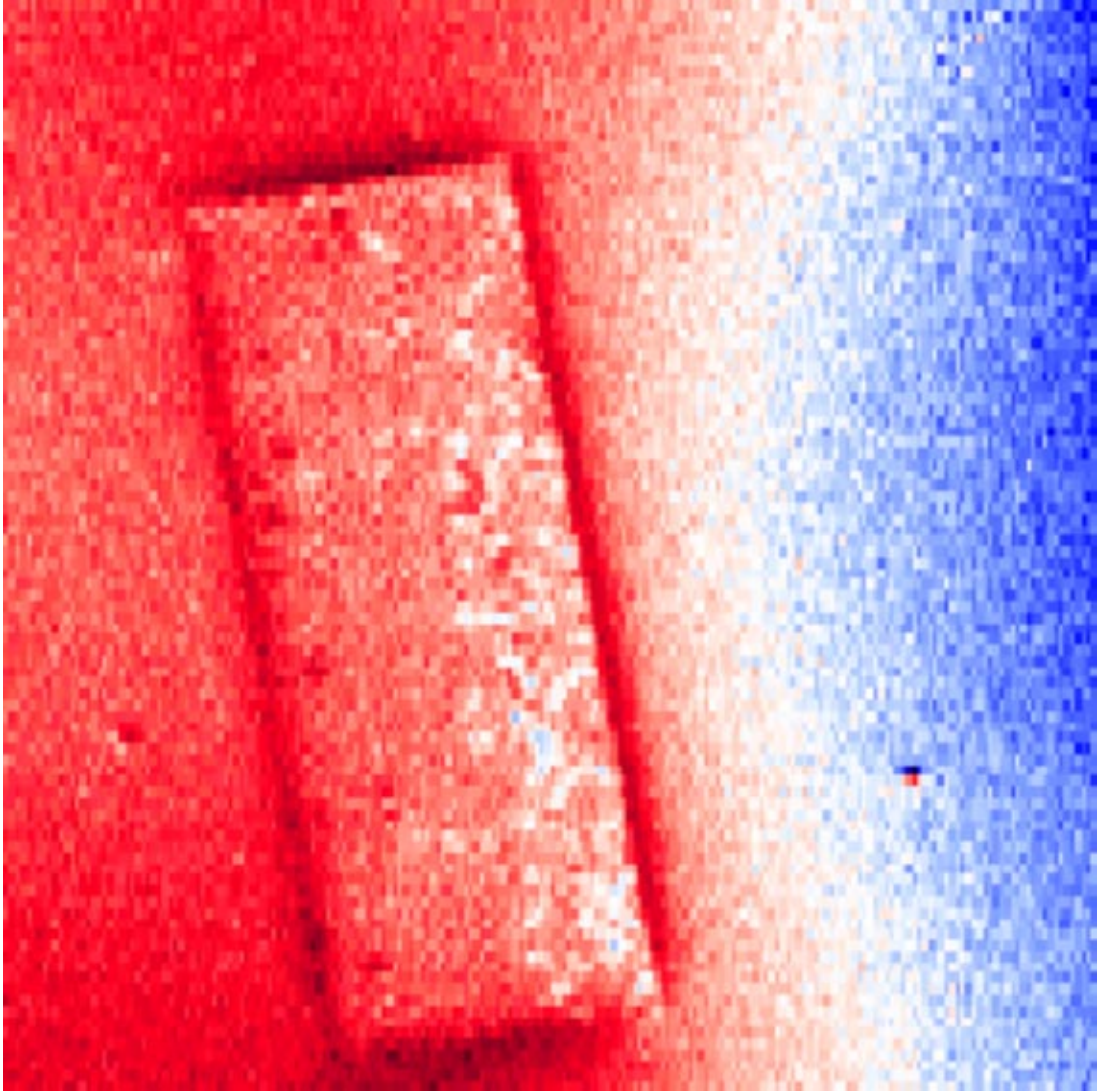


Figure 3.3: Magnetic image of sample after field cooling in $\phi_{\text{ext}} = 4.8$, $T = 4.2$ K. The colors range from blue (low) to red (high) for a total flux difference of $0.17 \Phi_0$ per unit cell of the array. Each image is 5×5 mm square.

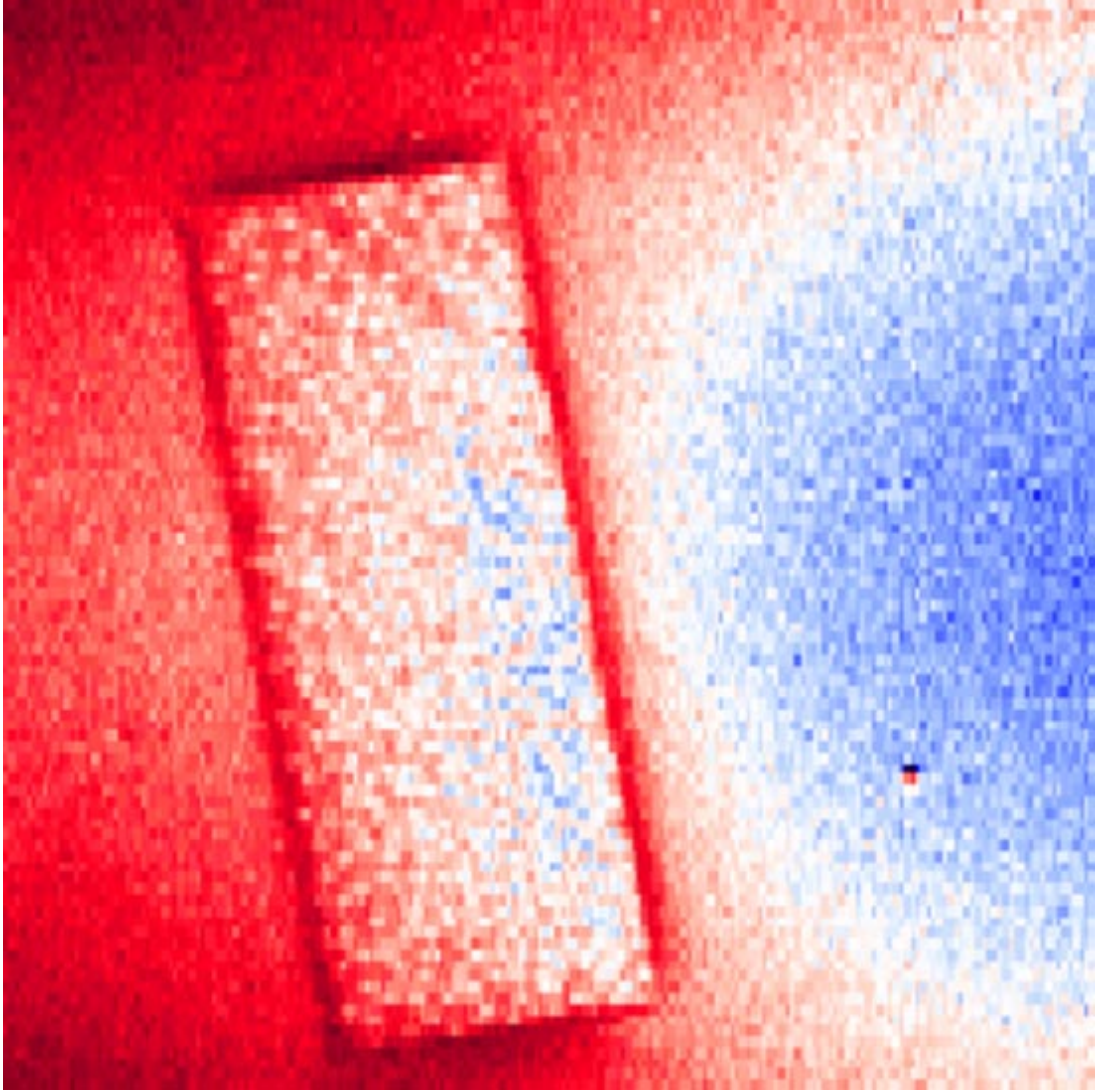


Figure 3.4: Magnetic image of zero field cooled sample, $T = 4.2$ K. The colors range from blue (low) to red (high) for a total flux difference of $0.17 \Phi_0$ per unit cell of the array. Each image is 5×5 mm square.

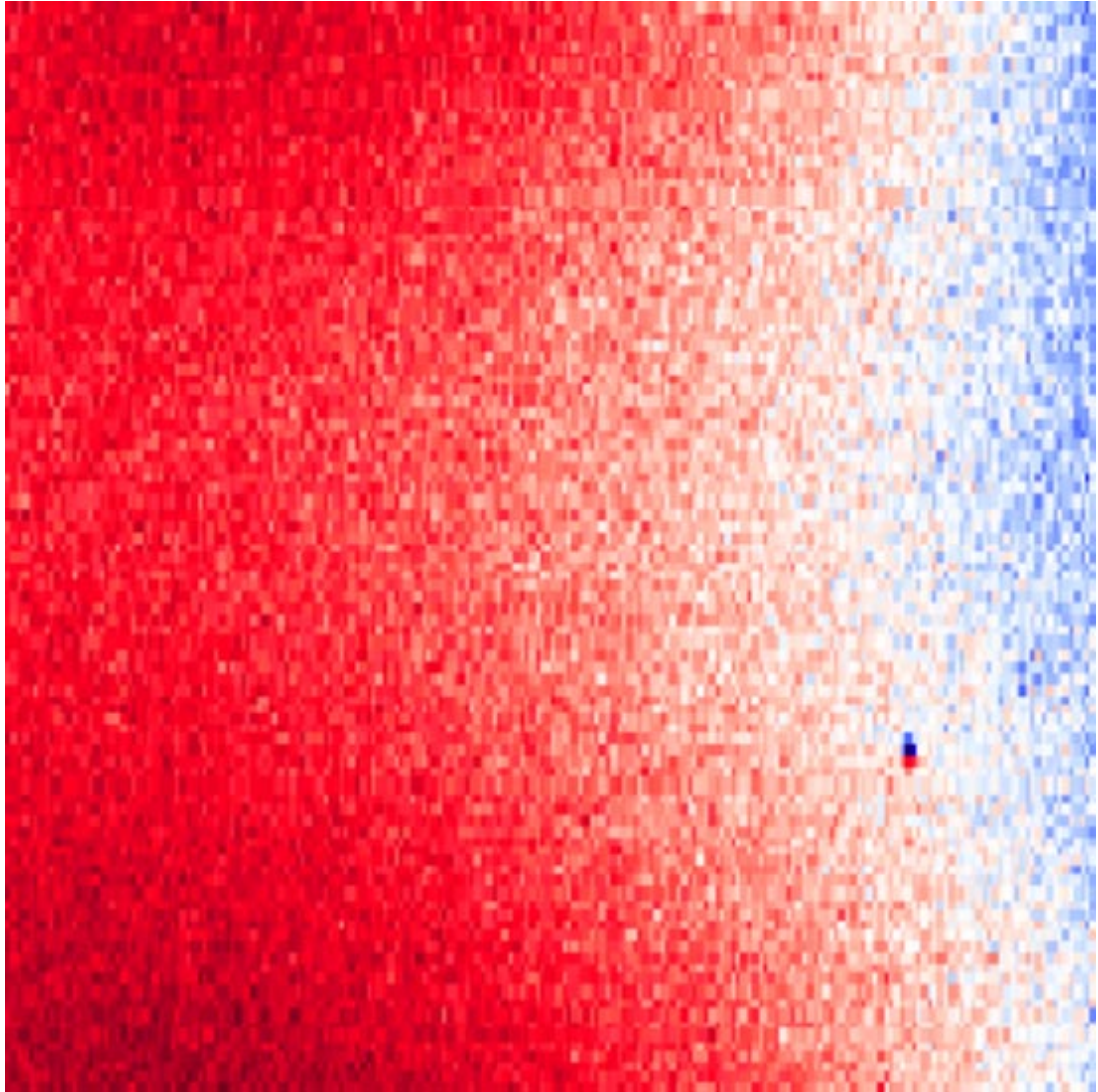


Figure 3.5: Magnetic image of $\phi_{\text{ext}} = 4.8$, $T = 13$ K. The colors range from blue (low) to red (high) for a total flux difference of $0.17 \Phi_0$ per unit cell of the array. Each image is 5×5 mm square.

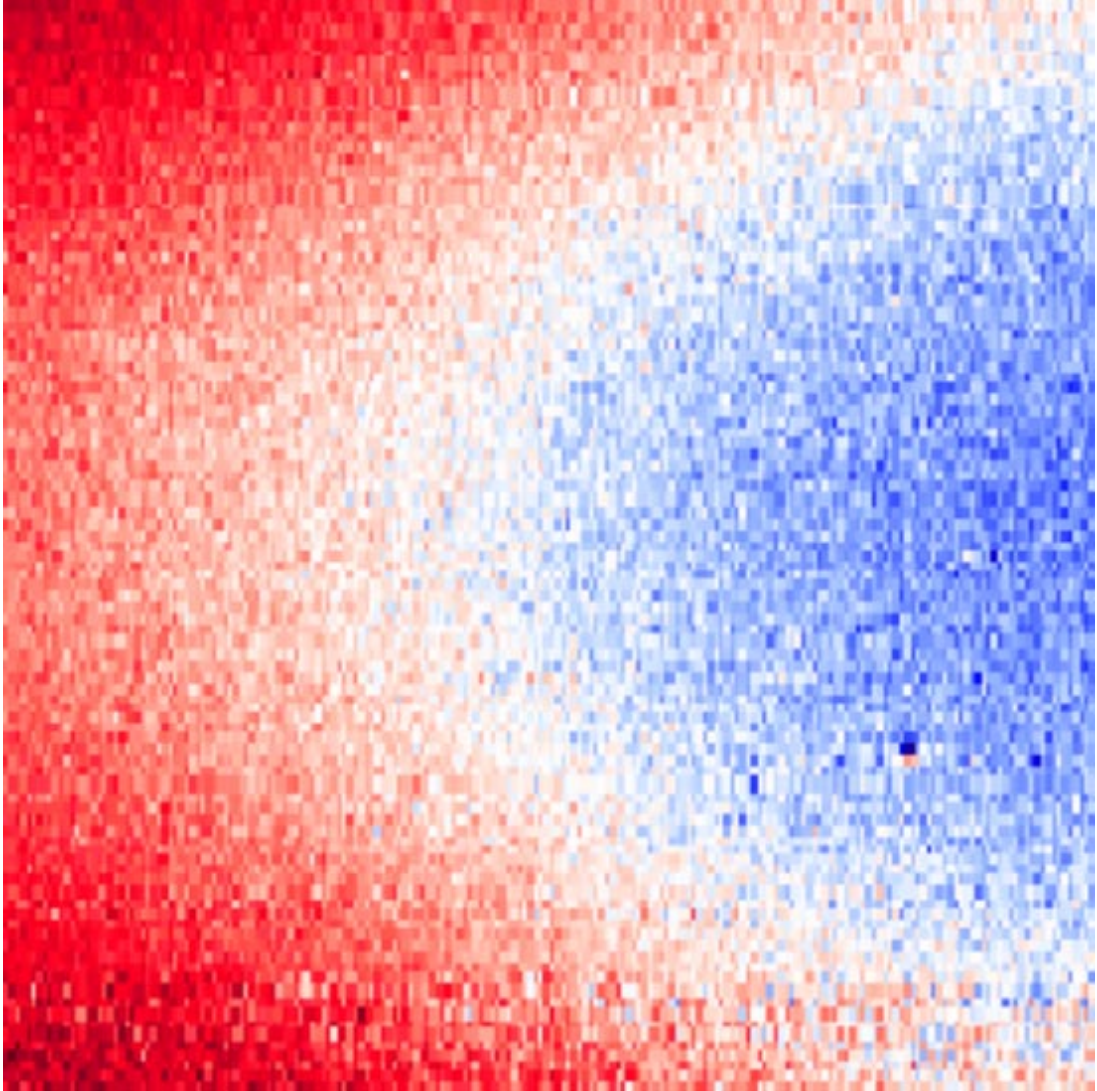


Figure 3.6: Magnetic image of zero field, $T = 13$ K. The colors range from blue (low) to red (high) for a total flux difference of $0.17 \Phi_0$ per unit cell of the array. Each image is 5×5 mm square.

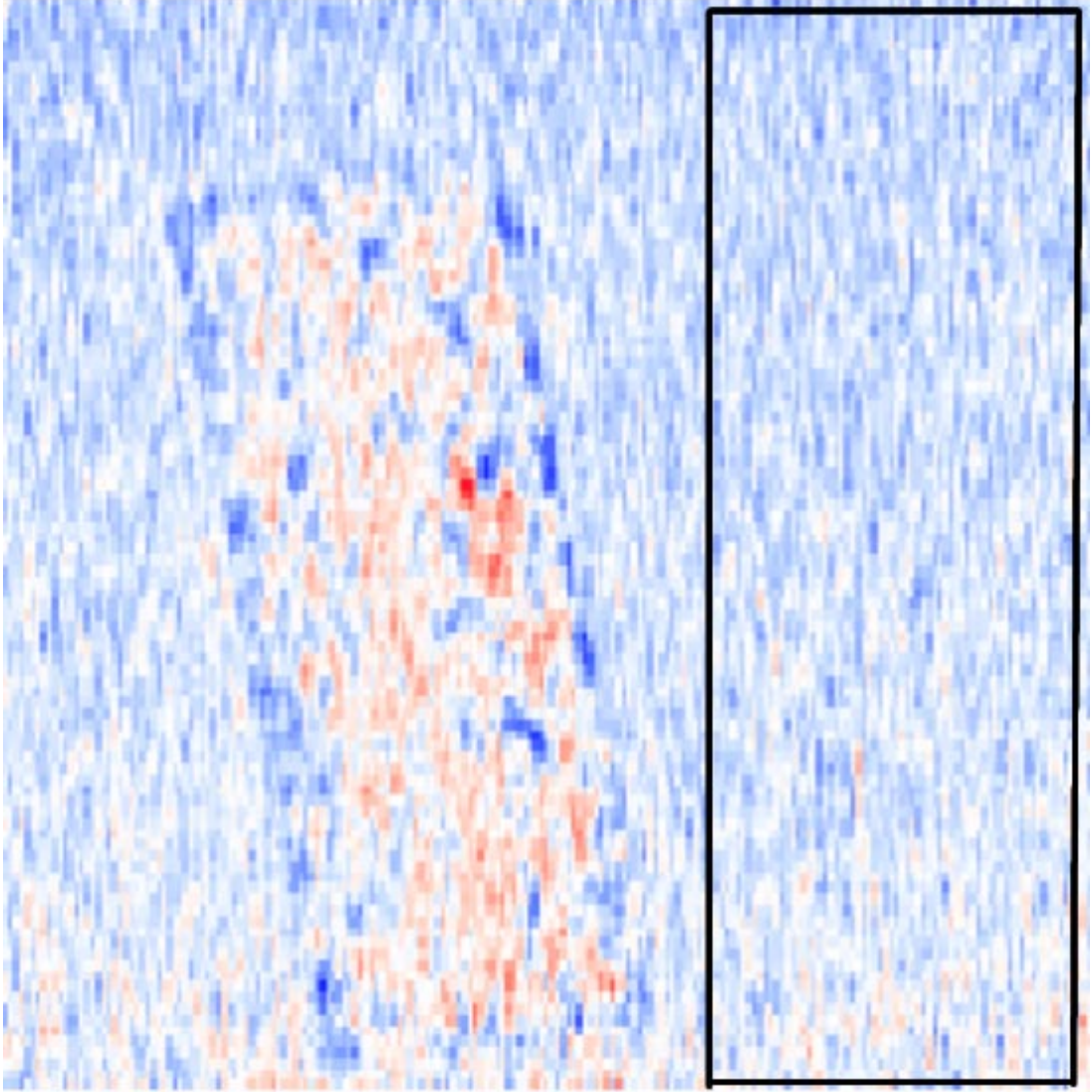


Figure 3.7: Magnetization of 30×100 junction array after field cooling in $\phi_{\text{ext}} = 4.8$. The color ranges from red, $\phi_{\text{mag}} = 0.45$ (paramagnetic) to blue, $\phi_{\text{mag}} = -0.45$ (diamagnetic). The long side of the array is 4.6 mm long.

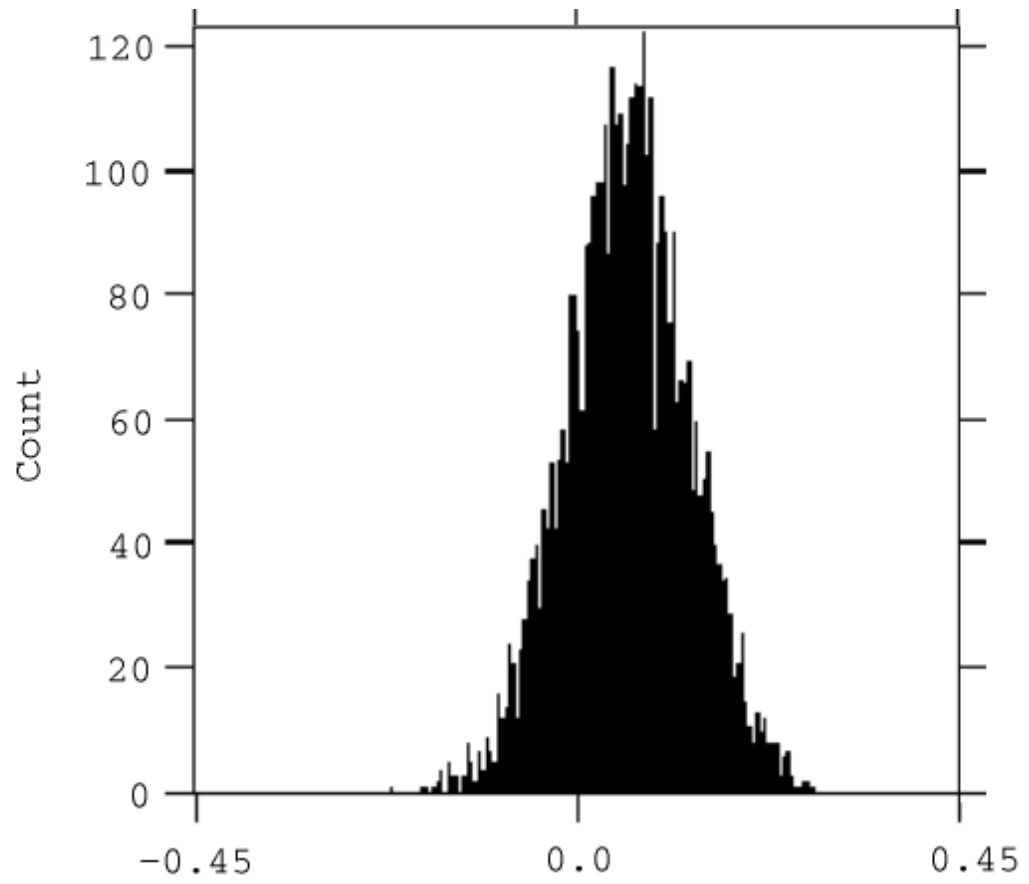


Figure 3.8: Histogram of the magnetization data shown in the magnetization image, Fig. 3.7.

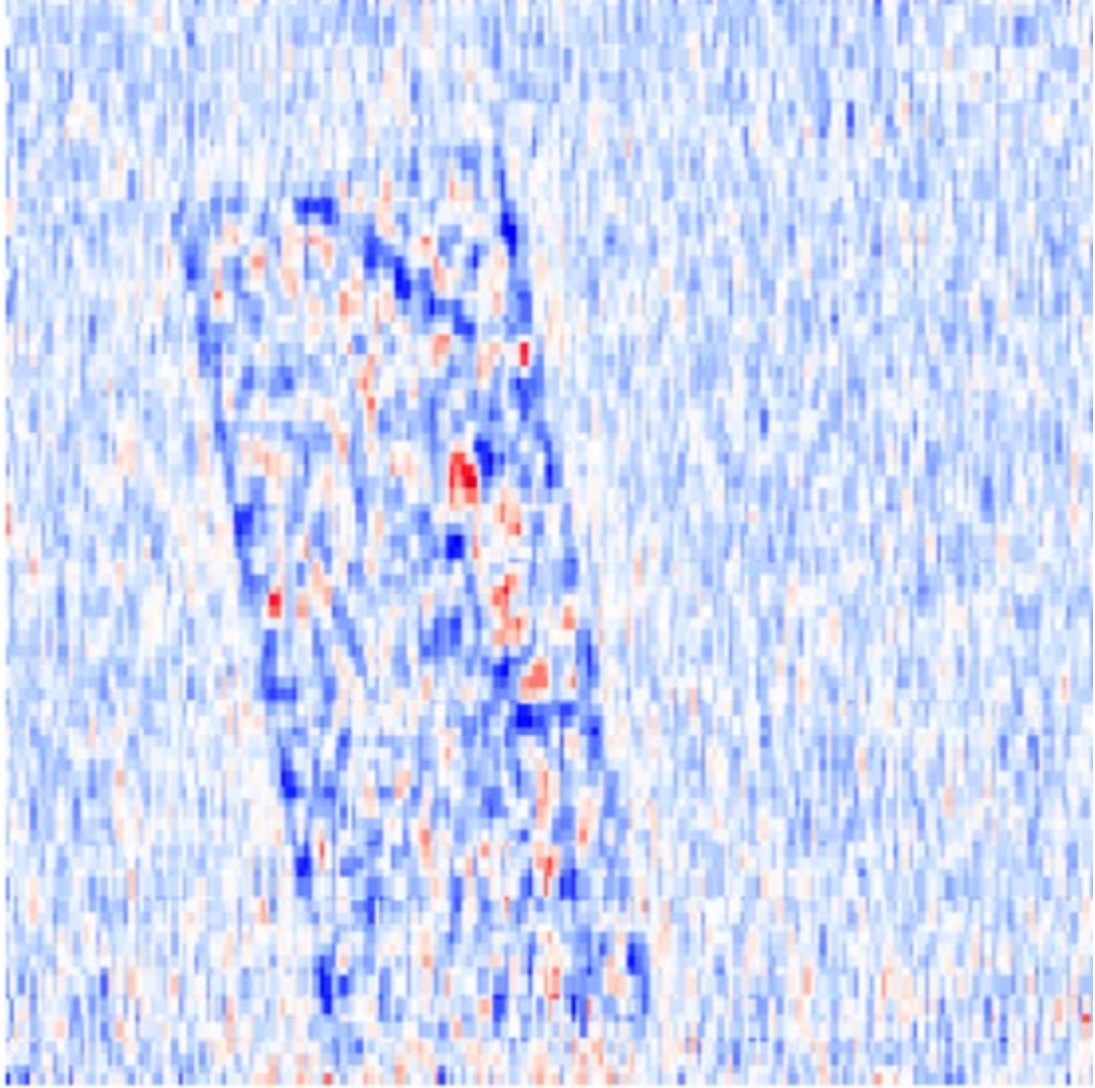


Figure 3.9: Magnetization of 30×100 junction array after field cooling in $\phi_{\text{ext}} = 1.2$. The color ranges from red, $\phi_{\text{mag}} = 0.45$ (paramagnetic) to blue, $\phi_{\text{mag}} = -0.45$ (diamagnetic). The long side of the array is 4.6 mm long.

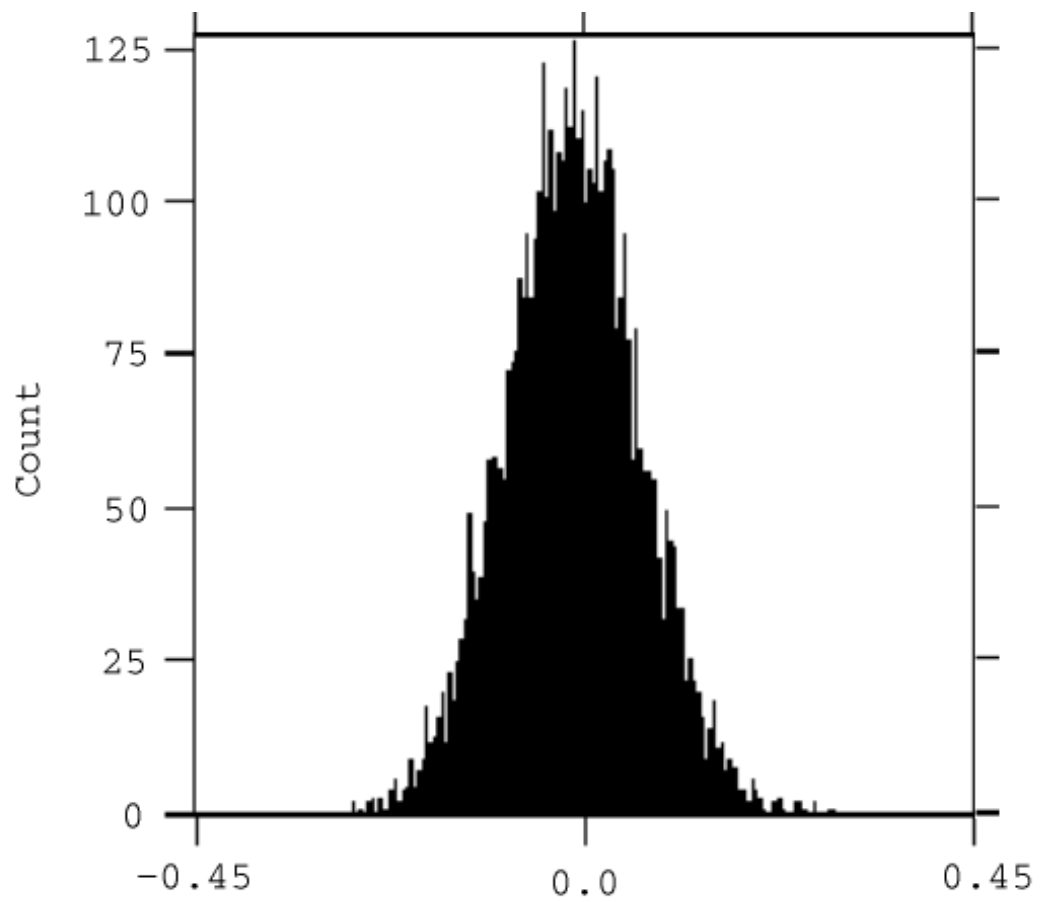


Figure 3.10: Histogram of the magnetization data shown in the magnetization image, Fig. 3.9.

If there were no systematic position-dependent errors, we would need only measure the field-cooled image to get Φ and the image of the field at 13 K to get Φ_{ext} . However, friction in the plastic scanning mechanism generates heat that does not dissipate quickly into the liquid helium bath and warms both the SQUID and the sample by slightly less than 1 K. This change in the sample temperature does not matter. The sample never warms to the point where thermal activation can overcome the energy barriers due to the array's Hamiltonian, (2.30). Conversely, the heating of the SQUID is important.

Fig. A.3 shows how the SQUID output changes during a 1 K temperature change. This change is comparable to the signal level shown in Fig. 3.3 through Fig. 3.6, so the heating of the SQUID must be considered in order to validate the results. This heating effect depends upon the sample position because the friction changes during different parts of a scan. Consequently, each image of the sample will measure two things, the real flux threading the SQUID Φ and a false “flux” distribution $\Phi_{\text{Friction @ 4.2 K}}$ due to the position-dependent heating. The false flux distribution will be different at different temperatures since the sample's temperature causes a noticeable heat load on the SQUID.

It is further possible that after eliminating the flux from the SQUID that there might be some background flux impinging upon the sample. This is clear in the zero field-cooled image, Fig. 3.4, in which some array response is evident despite the lack of applied field. This false flux signal will be a time-independent $\Phi_{\text{background}}$ in all the images in Fig. 3.3 through Fig. 3.6 and will just subtract out.

The total field-cooled flux in Fig. 3.3 thus contains three sources, the real Φ , a false flux reading in the SQUID due to friction, and the background flux, so

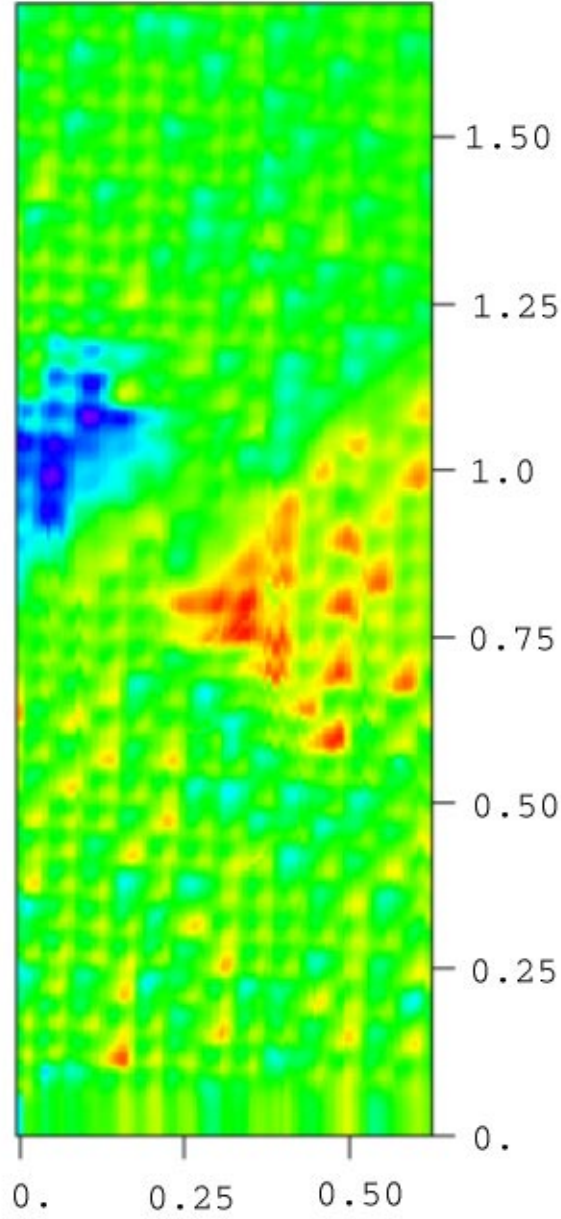


Figure 3.11: Zero field cooled magnetic image of 30×100 Josephson-junction array, with the SQUID positioned in the middle of the sample during cooling. The color scale represents a range from purple (low) to red (high) of $8\Phi_0$ per unit cell of the array and the x and y units are shown in millimeters. The flux trapped in the array is due to the currents flowing in the SQUID and feedback coil wires on the SQUID tip. The smeared out data near $x = 0$ is a mechanical artifact.

that

$$\Phi_{\text{FC}} = \Phi + \Phi_{\text{Friction @ 4.2 K}} + \Phi_{\text{background}}. \quad (3.7)$$

The total zero field-cooled flux in Fig. 3.4 also contains a false flux signal due to friction and the background flux

$$\Phi_{\text{ZFC}} = \Phi_{\text{Friction @ 4.2 K}} + \Phi_{\text{background}}. \quad (3.8)$$

The total measured high-temperature flux in Fig. 3.5 also contains a false flux due to friction. The magnitude is different because the SQUID sees a different heat load due to the higher temperature of the sample,

$$\Phi_{\text{HT}} = \Phi_{\text{ext}} + \Phi_{\text{Friction @ 13 K}} + \Phi_{\text{background}}. \quad (3.9)$$

The measured zero-field, high-temperature flux in Fig. 3.6 is

$$\Phi_{\text{ZHT}} = \Phi_{\text{Friction @ 13 K}} + \Phi_{\text{background}}. \quad (3.10)$$

Eqns. (3.7) - (3.10) combine to give the total sample magnetization

$$\Phi_{\text{mag}} = \Phi - \Phi_{\text{ext}} = (\Phi_{\text{FC}} - \Phi_{\text{ZFC}}) - (\Phi_{\text{HT}} - \Phi_{\text{ZHT}}). \quad (3.11)$$

Fig. 3.7 shows the magnetization image resulting from the four passes given in Fig. 3.3 through Fig. 3.6 after applying (3.11) to the data. The red colors in the image represent $M > 0$, a paramagnetic magnetization and the blue colors represent $M < 0$, a diamagnetic magnetization. Qualitatively the interior of the array is more *red* than blue, hence it is paramagnetic.

For each scan, data are collected every $5 \mu\text{m}$ in the x direction and every $50 \mu\text{m}$ in the y direction. The discrepancy between data collection in x and y direction results from the scanning mechanism. The scan lines are in the x direction while the raster lines are in the y direction. Each image in Fig. 3.3 through Fig. 3.6 took

approximately 45 minutes to complete. Each magnetization measurement must be completed before the liquid helium boils out of the Dewar, which has a hold time of 11 to 12 hours. In order to make several magnetization measurements to check consistency it would be prohibitive to increase the amount of time required for each scan.

3.4 Experimental results

3.4.1 30×100 junction array

We first looked at a 30×100 Josephson-junction array performing field cooled measurements of the type described above in Section 3.3. We determined that the array could be either paramagnetic or diamagnetic depending upon the cooling field. Fig. 3.7 through Fig. 3.10 demonstrates the results of field cooling for the array for two external fields, $\phi_{\text{ext}} = 1.2$ and $\phi_{\text{ext}} = 4.8$. The colors in Fig. 3.7 and Fig. 3.9 represent the magnetization in the image at each point. The colors range from red, $\phi_{\text{mag}} = 0.45$ (paramagnetic data) to blue, $\phi_{\text{mag}} = -0.45$ (diamagnetic data).⁷ By looking at the images in Fig. 3.7 we can qualitatively see that the array is overall paramagnetic, since it is more red, although the magnetization is clearly quite complicated. In Fig. 3.9 the array is overall diamagnetic, since it is more blue.

There is an additional important feature to note which appears in all of the magnetization images collected, regardless of the overall array magnetization. The array always has a diamagnetic screening current (shown in the images as a blue loop) around the outside edge, *c.f.* Fig. 3.7 and Fig. 3.9.

⁷Recall the definitions made in (2.8) that $\phi = \Phi/\Phi_0$.

In order to make a quantitative analysis, we looked at histograms of the individual magnetization images. For this 30×100 array, we looked only at the bottom one third of the array because scratches were accidentally introduced into the array *in situ* which produce anomalous results. The extent of the anomalous magnetization due to the scratches matches up well with the actual extent of the scratches as observed under the optical microscope. Because of the close correlation between the location of the scratches in the magnetic and optical images, it was concluded that the scratches did not affect the magnetization results very far from the area of the scratches.

Histograms for Fig. 3.7 and Fig. 3.9 are shown in Fig. 3.8 and Fig. 3.10 respectively. These two histograms are representative of the histograms generated for all the data on this array. For Fig. 3.7, field cooled at $\phi_{\text{ext}} = 4.8$, the mean of Fig. 3.8 is $\langle \phi_{\text{mag}} \rangle = 0.068$ with a standard deviation of $\sigma = 0.15$, clearly greater than zero, so the array is overall paramagnetic. Similarly for Fig. 3.9, field cooled at $\phi_{\text{ext}} = 1.2$, the mean of Fig. 3.10 is $\langle \phi_{\text{mag}} \rangle = -0.016$ with a standard deviation of $\sigma = 0.16$, clearly less than zero, so the array is overall diamagnetic. Interestingly, the histogram data for all of the cooling fields have similar widths, $\sigma \approx 0.15$.

In each magnetization image, Fig. 3.8 and Fig. 3.10, a region, indicated by a box, was analyzed to determine the magnetization of the background. We carried out this analysis by generating histograms for the background, similar to the histograms for the array. These background histograms are shown in Fig. 3.12 and Fig. 3.13 respectively. It is readily apparent from the comparison that the width of the background histograms is approximately one-half that of the array histograms, and that the mean of the background histograms is $\langle \phi_{\text{mag}} \rangle = 0.00$

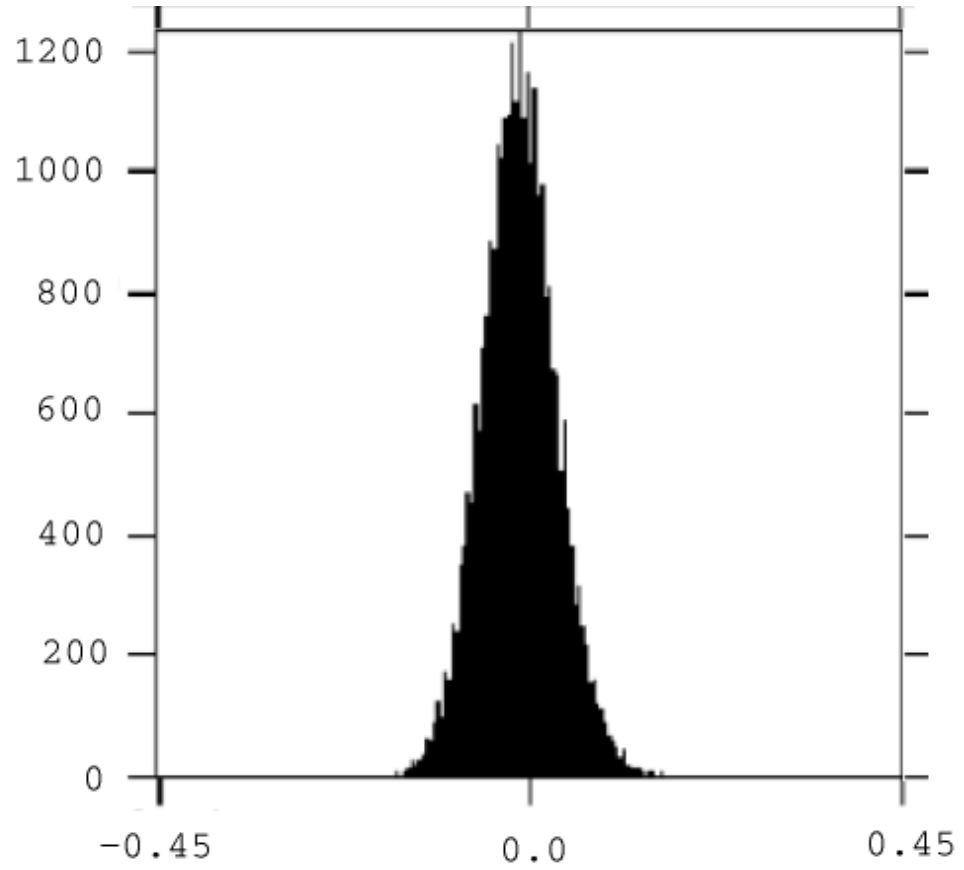


Figure 3.12: Histogram of background magnetization for $\phi_{\text{ext}} = 4.8$, from Fig. 3.7.

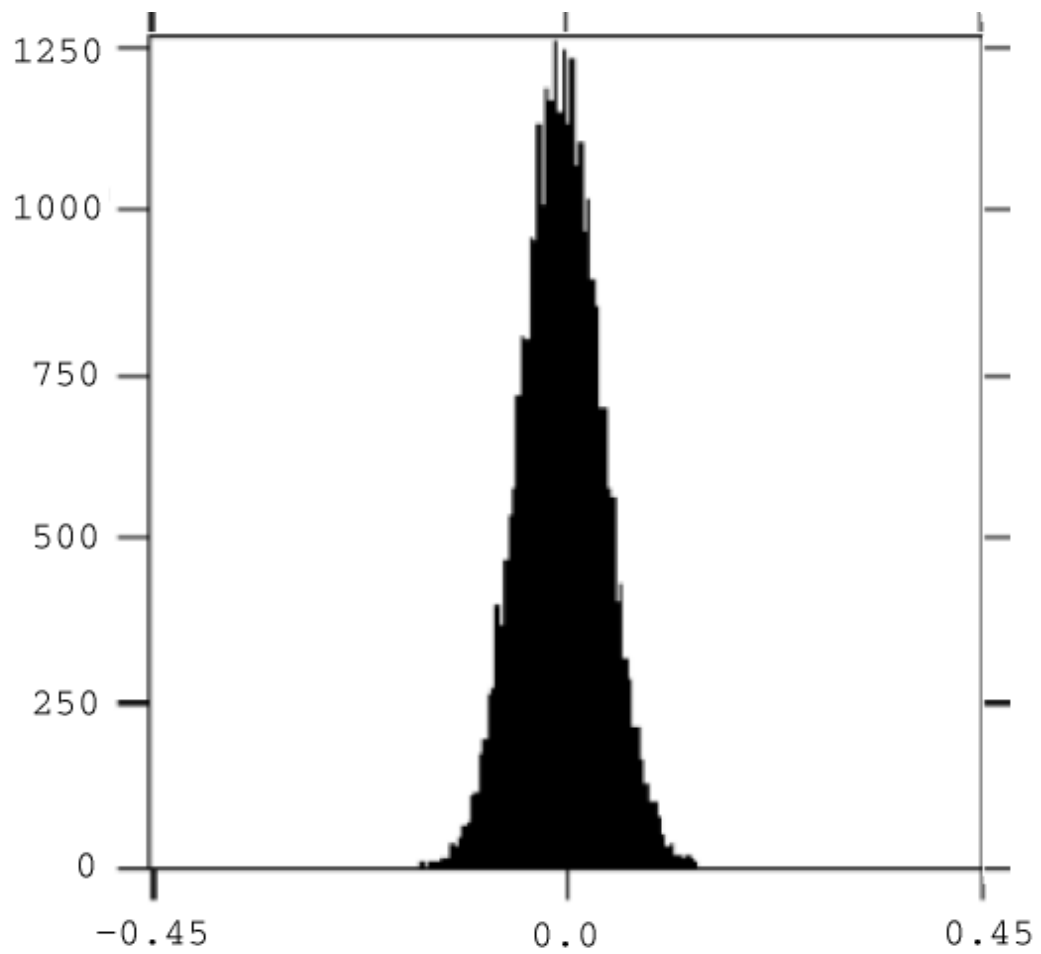


Figure 3.13: Histogram of background magnetization for $\phi_{\text{ext}} = 1.2$, from Fig. 3.9.

with a standard deviation of $\sigma = 0.08$, in contrast to the array histograms which have clear non-zero mean values and $\sigma = 0.15$.

We have repeated the same types of measurements on this array for many different values of the cooling field. These results are summarized in Fig. 3.14, which shows the measured mean magnetization of the array plotted versus the cooling field used. Note that the array magnetization is multivalued for some values of the cooling field. More importantly, although the array may be diamagnetic for small values of ϕ_{ext} , it is increasingly paramagnetic with increasing values of the external field. Note that the magnetization curves, as discussed in chapter 2, p. 14, are very steep for a single loop, so small variations in ϕ_{ext} may lead to large variations in ϕ_{mag} which could lead to our multivalued solutions. Additionally, we can see from (2.13) that a single loop has many different solutions for a given ϕ_{ext} so it is not unreasonable to think that the array might have multivalued solutions for a given ϕ_{ext} as well. In fact because the array is more complicated than a single loop, one might expect it to likely be frustrated during field cooling and to end up in different states for the same cooling field.

The range of flux in Fig. 3.10 (zero field, $T = 13$ K) is $0.17 \Phi_0$ per unit cell of the array, so we can be confident that the actual gradient of the background field is at least this small, meaning that the array sees flux uniform to $\phi_{\text{ext}} \pm 0.17$. This variation in ϕ_{ext} corresponds to a potential variation in magnetization of ± 0.05 by comparing with (2.13).

Because of the large number of data points that went into computing the averages for Fig. 3.8 we find a mean paramagnetic response of $\phi_{\text{mag}} = 0.063 \pm 0.005$. and for Fig. 3.10 we find a mean diamagnetic response of $\phi_{\text{mag}} = -0.016 \pm 0.005$. This is a larger variation than the control we have with the current source

to the solenoid, a Keithley 224 programmable current source [50].

3.4.2 100×150 junction array

In addition to the 30×100 junction array, we were interested to see what effect the geometry of the sample might have upon the measured magnetization because some theories predict that the size of the sample is important to the paramagnetic response [40, 51]. For this purpose, we chose to look at an array of 100×150 Josephson junctions. This array was otherwise exactly the same as the previous 30×100 junction array and the magnetization measurements were carried out in the same way.

An image showing a paramagnetic state of the larger array is shown in Fig. 3.15 with the corresponding histogram shown in Fig. 3.16. In this data set, for an applied field of $\phi_{\text{ext}} = -11.0$ the response was paramagnetic, $\phi_{\text{mag}} = -0.099 \pm 0.005$. There were no *in situ* scratches accidentally introduced into this array, however, there was some noise in the SQUID output, present as the straight horizontal line, in the top of the image, so we were able to analyze the magnetization histogram for the entire array, except for the noisy region.

The results from this measurement compare favorably with the results made on the smaller array. In Fig. 3.17 the large array mean magnetization is plotted against the cooling field. In agreement with the previous results on the smaller array, we see that the array magnetization increases with increasing external field. The magnitude of the magnetization is comparable. Additionally, as is evident in Fig. 3.15 the array, to which an external field of $\phi_{\text{ext}} = -11$ has been applied, has a diamagnetic screening current (colored red in this figure) around the outside. This diamagnetic screening current is again visible in all the images of the large

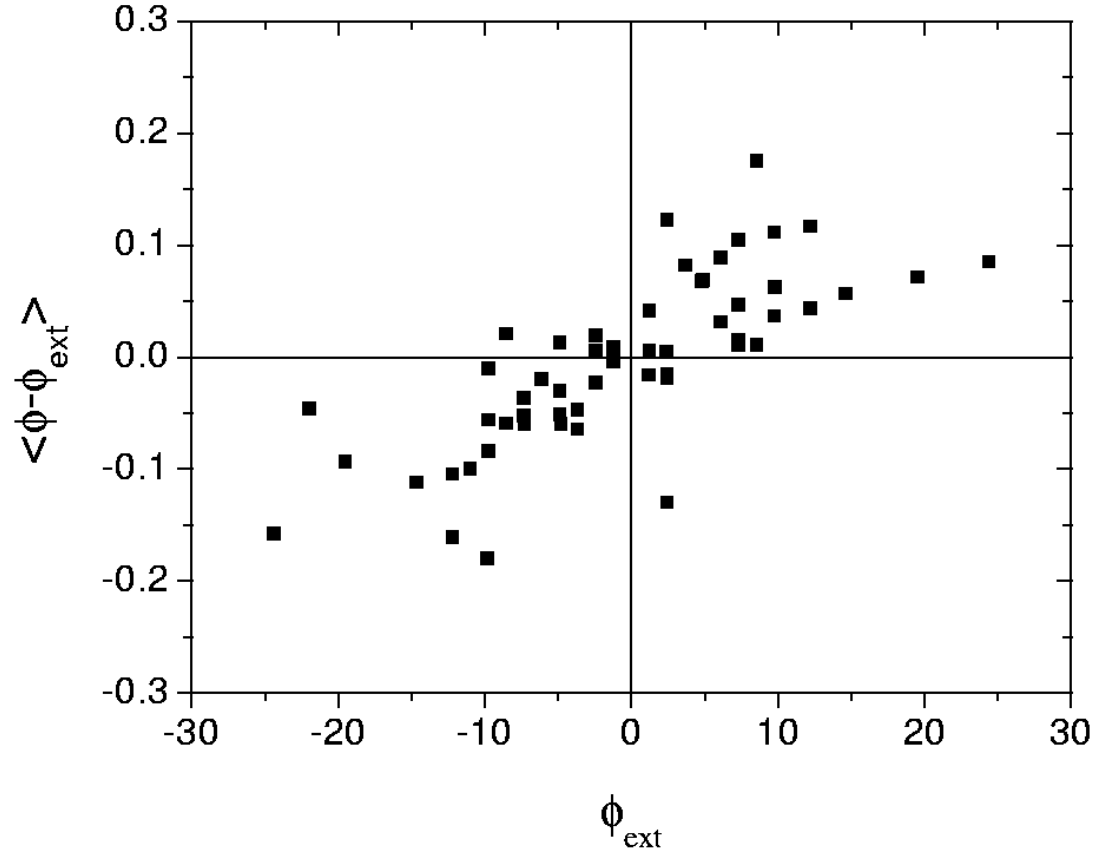


Figure 3.14: Measured mean magnetization for 30×100 junction array plotted versus cooling field. The error in each data point is less than the size of the symbol.

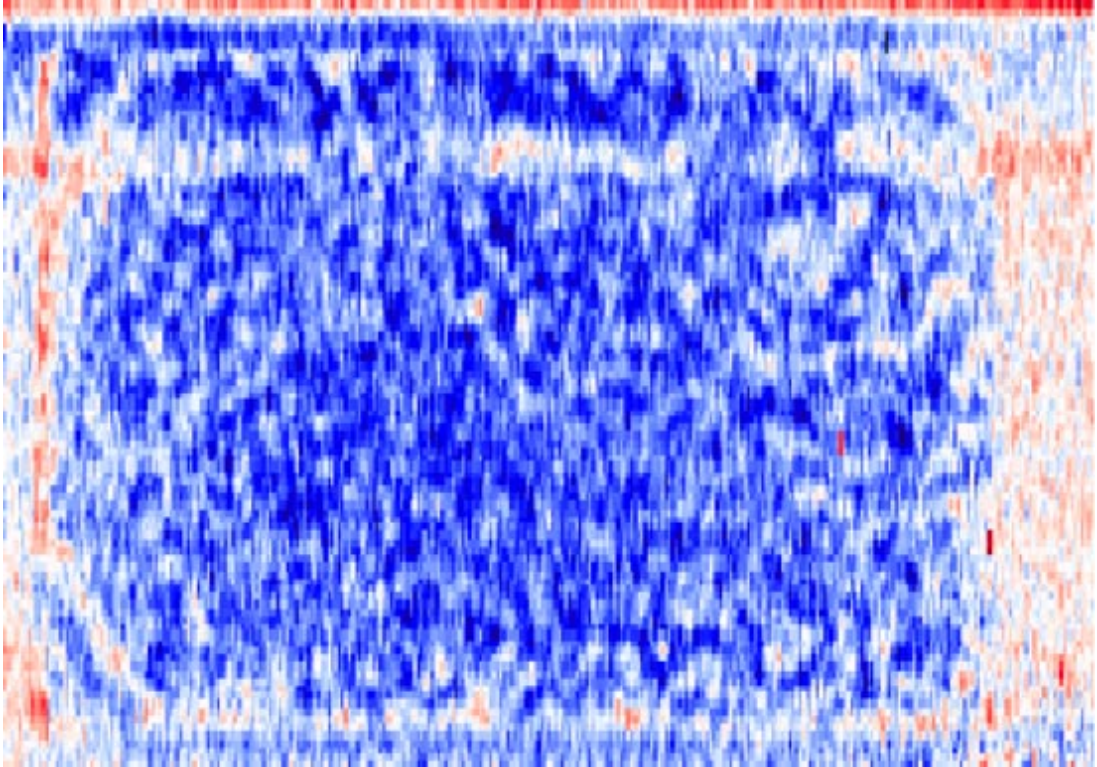


Figure 3.15: Representative paramagnetic image for the 100×150 junction array. The array was field cooled in a field of $\phi_{\text{ext}} = -11.0$. The color scale ranges from blue ($-0.45 \Phi_0$) to red ($0.20 \Phi_0$) and the short side of the array is 4.6 mm long.

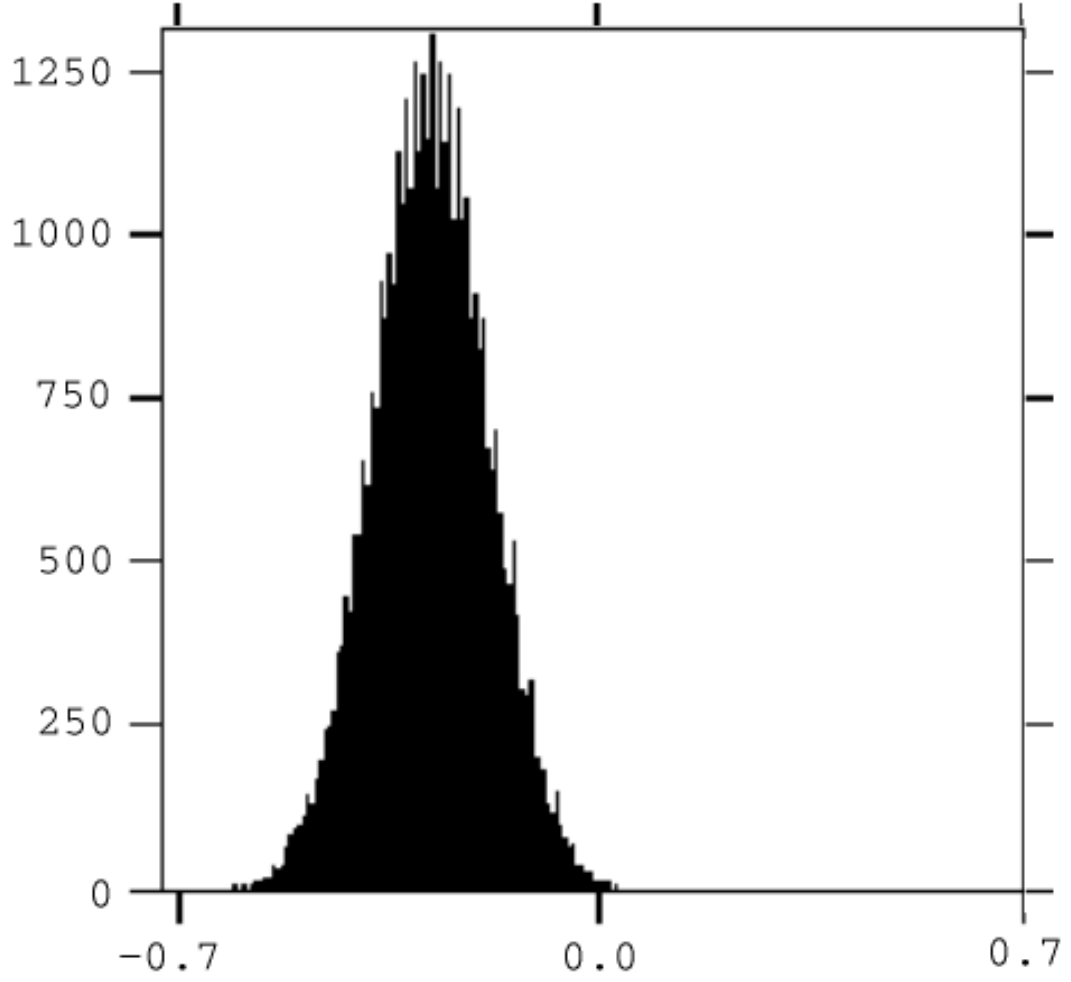


Figure 3.16: Paramagnetic histogram shown in Fig. 3.15. The array was field cooled in a field of $\phi_{\text{ext}} = -11.0$. The color scale ranges from blue ($-0.45 \Phi_0$) to red ($0.20 \Phi_0$) and the short side of the array is 4.6 mm long.

array.

3.5 Summary of magnetization measurements

Arrays of 30×100 and 100×150 junctions were measured in field-cooling experiments using a scanning SQUID microscope. The results on the arrays are very similar, both in magnitude of array magnetization and in average magnetization dependence upon external field. The next chapter will explain the various phenomena observed here and reconcile them with the ideas presented in chapter 2.

In both cases the array magnetization increases with increasing external field, and the array is preferentially paramagnetic. This is in contrast to the single-loop model which predicts equally that the the single loop will be either paramagnetic or diamagnetic equally often.

The magnetization internal to the array takes on a somewhat complicated, randomly distributed arrangement. The magnetization at the edge is always diamagnetic, regardless of the internal magnetization.

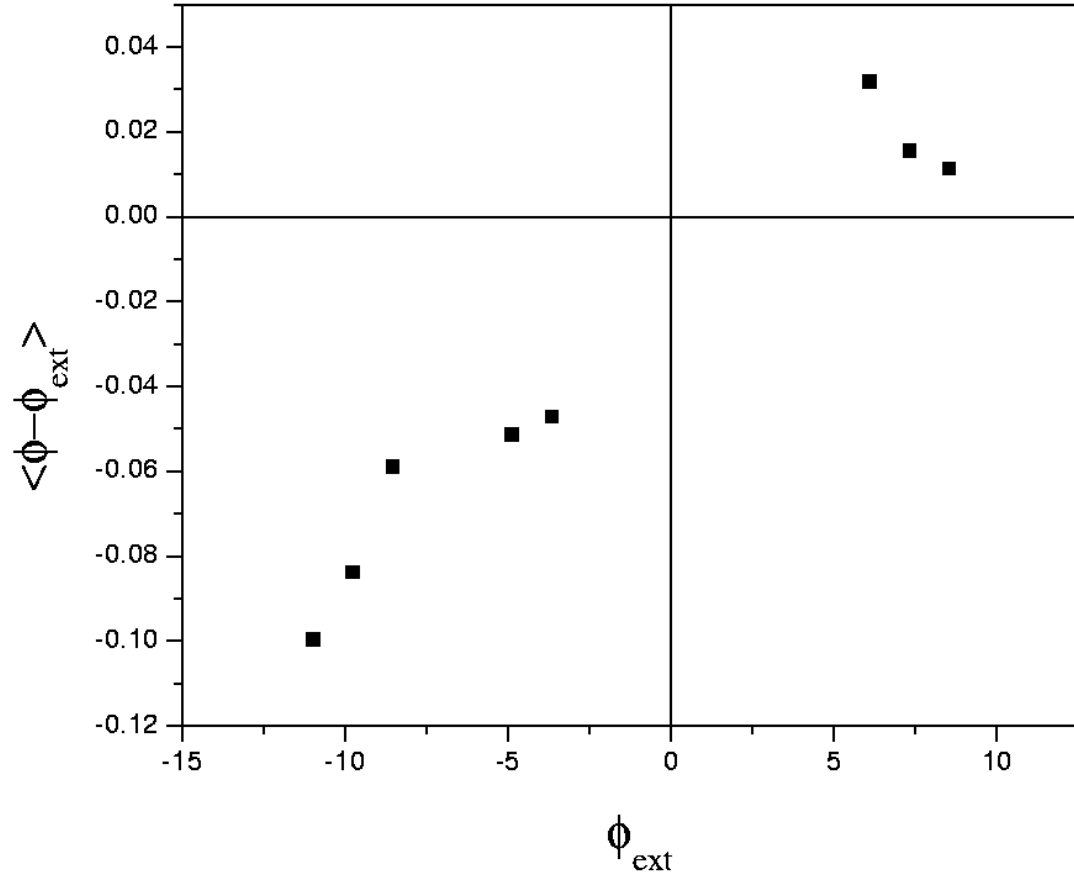


Figure 3.17: Measured mean magnetization versus cooling field for the 100×150 Josephson-junction array. The error for each data point is smaller than the size of the symbol.

Chapter 4

A model of the paramagnetic Meissner effect in multiply-connected superconductors

4.1 Introduction

As discussed in chapter 3, there have been many observations of PME in superconductors. In addition to these experimental observations, there have also been several theoretical attempts to explain the PME in these superconductors.

4.1.1 π -junction models

The first attempt to describe PME in high T_c superconductors came from Sigrist and Rice [13, 14], who argued that the presence of π -junctions in a superconductor would cause it to be paramagnetic. They further argued that π -junctions would come about due to a d -wave order parameter coupled with misaligned grains in the superconductor. This idea is basically the single loop model as discussed in chapter 2 (section 2.2, p. 6, (2.14)). There we discussed at length that Sigrist and Rice was incomplete because they chose a value of β_ℓ that was too small. Had they chosen a larger value of β_ℓ they would have seen that paramagnetism would

be possible at zero external flux for a loop with no π -junctions. They attributed PME only to the presence of a π -junction in the loop, and hence evidence for d -wave superconductivity. Sigrist and Rice proposed this theory before the first observation of PME in low T_c superconductors [37] and so were perhaps a bit overzealous in interpreting the implications.

4.1.2 Josephson-junction array models

Since Sigrist and Rice based their work on the idea of a single superconducting loop, others began to try to model a superconductor as various types of Josephson-junction arrays. One model, by Dominguez *et al.* [17], contained several flaws; they treat the case of a Josephson-junction array with randomly distributed π -junctions, but do not treat the case of an array without π -junctions, essentially repeating the mistake of Sigrist and Rice. Dominguez *et al.* reached the similar conclusion that the presence of π -junctions allows the sample to behave paramagnetically.

Models of this type were also studied by Auletta *et al.* [52] who modeled the array as a series of concentric loops of Josephson junctions including the mutual inductance between the loops. Additionally, Chandran [26] performed similar calculations using a square array and a full mutual induction matrix. Both Auletta *et al.* and Chandran use simplified models for the Josephson junctions which ignore the capacitance of the junction (RSJ model). Importantly, both treat only the case of *no* π -junctions, eliminating the problems with the Sigrist and Rice and the Dominguez *et al.* models. Remarkably, they were able to recreate the temperature-dependent magnetization during a model field cooling experiment and show that it compares favorably with the previously reported experimental

results (*c.f.* Braunisch *et al.* [31, 32]). However, neither report on the spatial distribution of the magnetization over the array, which we have directly measured here.

More recently, De Leo *et al.* [9], used an RCSJ Josephson-junction array to dynamically model the field-cooling process, and obtained results remarkably similar to the experimental results discussed in chapter 3. The relationship between this model and the experiment will be discussed in more detail in section 4.5.3.

4.1.3 Flux compression

In a departure from the Josephson-junction array model of PME, Koshelev and Larkin [51] proposed the flux compression model. The flux compression model relies on the superconductor having a spatial variation in T_c , such that the exterior of the sample becomes superconducting before the interior of the sample. Because the exterior becomes superconducting first, it effectively traps flux in the center of the sample, and compresses the trapped flux (hence “flux compression”) as the superconducting region grows from the outside-in. This trapped flux, and the screening currents required to keep the flux trapped, create a positive magnetic moment, the paramagnetic Meissner effect. An important aspect of the flux compression model is that it gives specific predictions for the flux and current distribution throughout the sample – something that can easily be tested with the SQUID microscope.

A phenomena related to the flux compression model is the “giant vortex state” model [53, 54]. It may be appropriate for mesoscopic superconductors, such as the aluminum disks measured by Geim *et al.* [40], but does not apply to the macroscopic situations discussed here.

4.1.4 Pinning and surface barriers

In addition there are other proposed models which essentially rely on defects in the superconductor to create the PME. One may imagine, *e.g.* that surface damage to the superconductor pins flux during the field cooling process and causes the sample to be paramagnetic. It has additionally been proposed that some type of surface barrier may result in flux trapping in the sample [55], or that Andreev bound states at the surface of the superconductor [56] may result in paramagnetism.

4.2 Comparison of experimental data to various models

Simple models involving π -junctions do not apply to the niobium Josephson-junction array samples that were measured. It has clearly been demonstrated that niobium, an *s*-wave superconductor, exhibits PME in the absence of π -junctions. Furthermore, it is clear from the discussion of the single loop in chapter 2 that a single loop of Josephson junctions, without any π -junctions, can in theory be paramagnetic after field cooling.

The various Josephson junction models treating PME in an array model of superconductivity have great merit, but do not provide any spatially resolved data to which we might compare our array data. Additionally, we cannot practically measure the sample magnetization *vs.* temperature during the field cooling process, in order to compare with their models. In order to do this we would need to stop and image the array many different times as we cool it through T_c to 4.2K. In principle we can do this, but we cannot maintain temperature stability

near T_c in order for these scans to be more interesting than the scans presented herein. However, the spatially resolved data we obtain is extremely useful for the comparison with many of these theories, and, as we will show, motivates our explanation for the phenomena of PME.

Based on our experimental observations we can clearly rule out the flux compression model as untenable. Our data looks nothing like the proposed flux distribution for a sample exhibiting flux compression and in fact looks quite random. This is really not surprising since we do not expect any of the requirements of flux compression to be met in our experiment. First, our sample is well grounded thermally to the sapphire rod of the sample stage in the experiment. Furthermore, because of the photolithographic uniformity we do not expect that the outermost islands of the array would have a T_c *higher* than the inner islands. In fact in our arrays, we expect there to be no preference for deposition errors near the edges. However, in thin film samples we might expect deposition errors to cause the sample edge to have defects which would tend to *lower* the sample T_c .

Indeed, the primary features of our experimental data are not predicted by any of the published theories of PME. We always observe a diamagnetic region around the edge of the sample in addition to a region of Gaussian distributed flux inside, but generally with a paramagnetic mean. Finally, the paramagnetism of the array appears to increase with increasing external field.

4.3 Mean field theory of Josephson-junction array

A very simple approximation is to assume that each loop in the Josephson-junction array behaves identically, and sees a mean field due to the response of the other loops in the array. This may be expressed as

$$-(\phi - \phi_{\text{ext}}) = \left. \frac{dG}{d\phi_{\text{ext}}} \right|_{\phi_{\text{ext}} + \lambda(\phi - \phi_{\text{ext}})} \quad (4.1)$$

where the coupling parameter $\lambda = \sum_{i \neq j} M_{i,j}/L$, and $M_{i,j}$ is the mutual inductance matrix. In practice, the summation must be cut off at the physical size of the array considered. We solved (4.1) numerically and found that the a paramagnetic array actually has its paramagnetism *enhanced* slightly by the mean field. Conversely, a diamagnetic array becomes more diamagnetic under the influence of the mean field. Fig. 4.1 shows the effect of this mean field on the array magnetization. The figure shows the magnetization of a simple single loop (solid line) and the magnetization of a single loop under the influence of the mean field (dashed line) from which it's clear that the magnetization of the loop is enhanced a small amount under the influence of the mean field.

The mean field model thus fails to agree with Fig. 3.14 and Fig. 3.17 which show a preference for paramagnetic response.

4.4 Array screening

The presence of the diamagnetic screening current flowing around the outside edge of the array must be accounted for in any realistic model. The array could accomplish this diamagnetic screening in one of two ways.

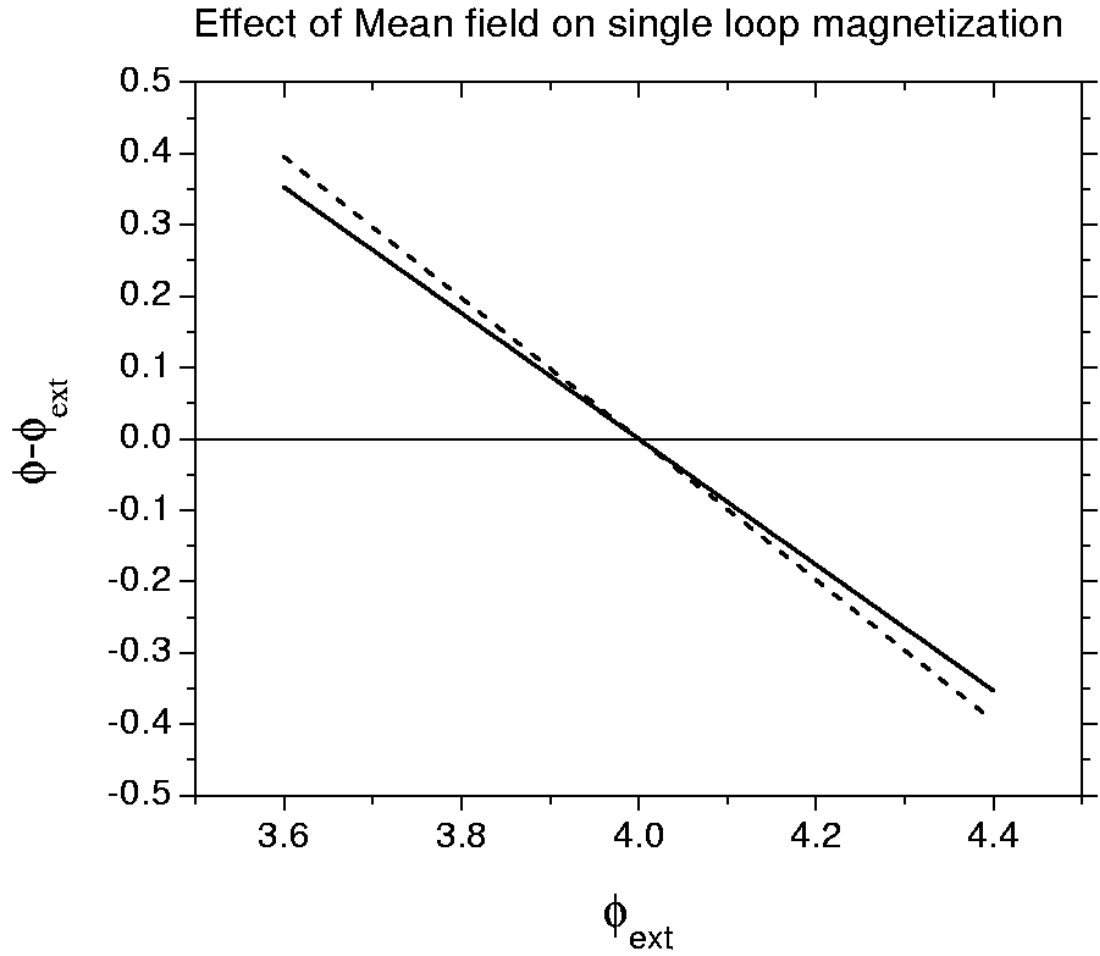


Figure 4.1: Effect of the mean field due to the surrounding plaquettes in the array on a given test plaquette. Plaquette magnetization plotted *vs.* ϕ_{ext} for the case of a single loop without the mean field (solid line) and the case of the single loop in the presence of the mean field (dashed line).

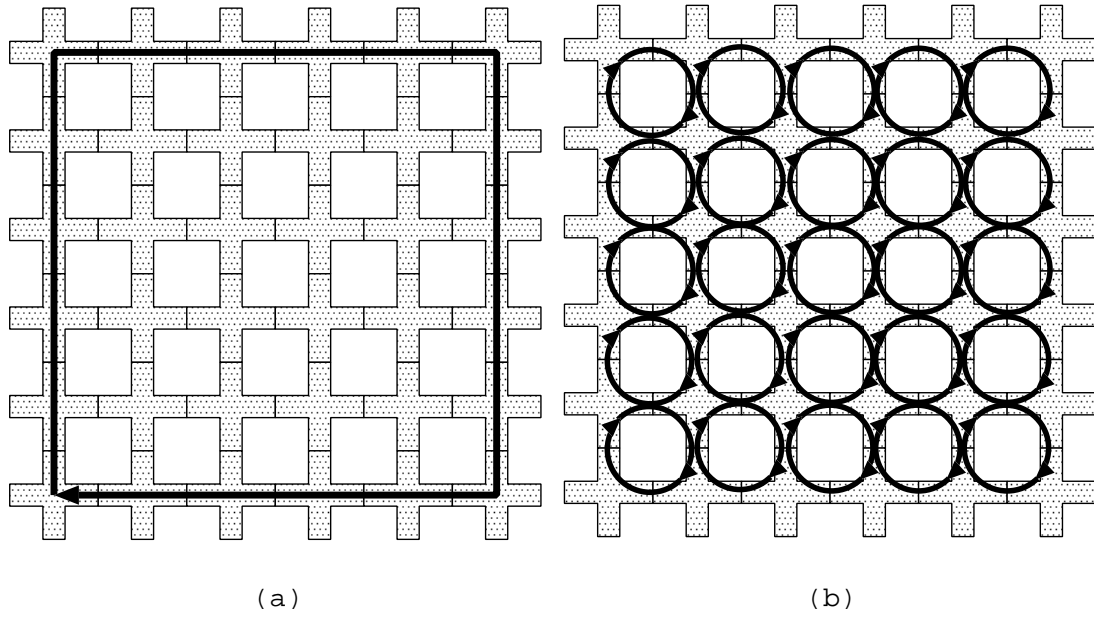


Figure 4.2: Different ways to generate Meissner screening in an array. (a) A large loop of many Josephson junctions around the outside edge of the array. (b) Each loop of many Josephson junctions around the outside edge of the array. (b) Each plaquette screens flux from the its own interior, and hence screening flux from the entire array.

First, the array, of size $N \times M$, may generate a screening current flowing around the outside edge of the array (large loop screening); in effect creating a large loop of $2(N + M)$ junctions around the outside of the array. Fig. 4.2(a) depicts this situation. This picture is similar to how a bulk superconductor might screen, with current flowing just around the outside edge and nowhere else inside. We want to know the maximum external field that this large loop can screen. To do this, we need to know how the self inductance of a square grows as the wire size grows.

4.4.1 Self-inductance of square loop

The self-inductance of a current loop may be defined from¹

$$LI = \Phi \tag{4.2}$$

in which Φ is the flux induced in the current loop due to the current I and L is the self-inductance.

A straightforward approach to the calculation of the self-inductance of a square loop is to determine the flux via the vector potential $\vec{A}(\vec{x})$ which is determined from the current flowing around the loop. For a square loop it is convenient to discretize the loop into four wires (each side of the square) and compute the vector potential due to each wire segment. With the vector potential we compute the flux using

$$\Phi = \oint \vec{A} \cdot d\ell \tag{4.3}$$

¹See Landau and Lifshitz[57], pp. 136-139 for an excellent discussion of the self inductance. They reach similar conclusions as to those drawn here.

around the entire square. The geometry for this calculation is shown schematically in Fig. 4.3.

The vector potential for a current distribution may be determined from²

$$\vec{A}(\vec{x}) = \frac{\mu_0}{4\pi} \int_V \frac{\vec{J}(\vec{x}')}{|\vec{x} - \vec{x}'|} d^3 \vec{x}' \quad (4.4)$$

in which $\vec{J}(\vec{x})$ is the current density distribution and V is over the entire volume of the current density. We assume that the current density distribution is small in extent and may be treated as a constant so that (4.4) may be reduced to

$$\vec{A}(\vec{x}) = \frac{\mu_0 I}{4\pi} \oint \frac{d\ell'}{|\vec{x} - \vec{x}'|}. \quad (4.5)$$

If we consider the vector potential due to one single side of the square, \overline{AB} , in Fig. 4.3, the integration in (4.5) becomes

$$\vec{A}(x, y) = \frac{\mu_0 I}{4\pi} \hat{y} \int_{y_1}^{y_2} \frac{dy'}{\sqrt{(x - x_1)^2 + (y - y')^2}}. \quad (4.6)$$

This integrates to become

$$A_y(x, y) = \frac{\mu_0 I}{4\pi} \left\{ \sinh^{-1} \left(\frac{y - y_2}{x - x_1} \right) - \sinh^{-1} \left(\frac{y - y_1}{x - x_1} \right) \right\}. \quad (4.7)$$

We have implicitly assumed that the point (x, y) in (4.7) is outside of the wire. If we define the halfwidth (or radius) of the wire to be W this implies that $W \ll |y_2 - y_1|$. Similarly we can compute the vector potential due to each of the remaining three wire segments of the square. With these four components to the vector potential we may compute total flux due to the current numerically through (4.3) and the self inductance through (4.2).

²This derives from Maxwell's equations and the definition of the vector potential $\vec{B} = \nabla \times \vec{A}$. See Jackson[58], pp. 173-176 for a complete discussion of the derivation. This form implies the choice of the Coulomb gauge, $\nabla \cdot \vec{A} = 0$.

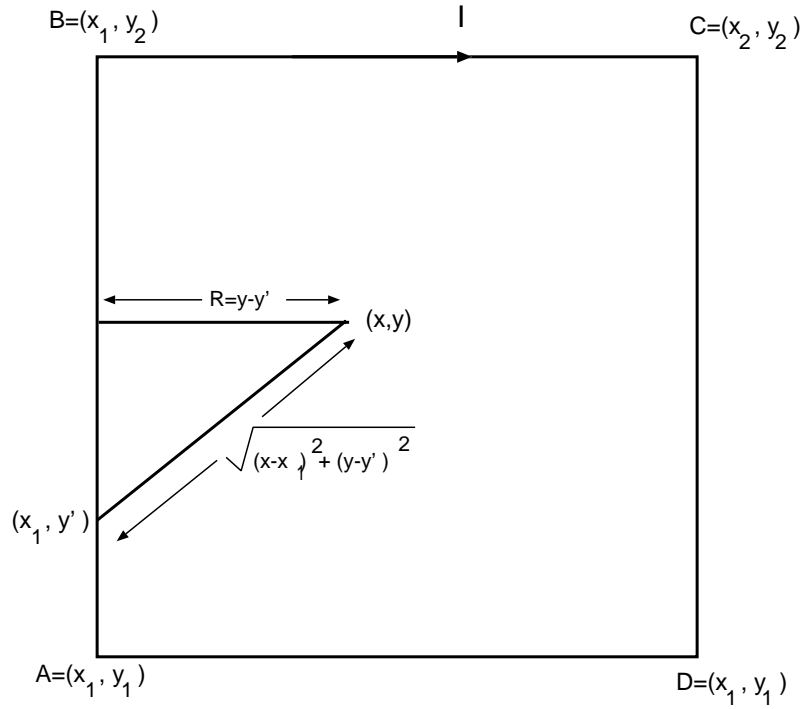


Figure 4.3: Geometry for calculation of square loop self inductance. The half width of the wire W is not shown here, and is taken as much smaller than the distance between any of the vertices of the square, *i.e.* $W \ll |y_2 - y_1|$.

We expect the self inductance to go to zero as the area of the loop goes to zero in this model. However, in the limit of zero area, the model described here is no longer valid. Instead, see Jaycox and Ketchen [47] for a discussion of the self inductance of a finite width wire loop.

We expect that as the loop grows arbitrarily large, the self inductance will grow linearly. In this limit, we can neglect the finite size of the wire width making up the square and use Ampere's Law to simply compute the magnetic induction due to the current as

$$B(r) = \frac{\mu_0 I}{2\pi r}, \quad (4.8)$$

r being the distance from the wire. Furthermore, the area of the square grows like r^2 . Therefore the self-inductance grows like

$$LI \propto BA \propto \frac{1}{r} r^2 = r \quad (4.9)$$

or linearly with the size of the square. When we compute the self inductance numerically, this is exactly the dependence we find. The computed self inductance is plotted in Fig. 4.4 for a range of square sizes similar to our overall array size.

4.4.2 Screening due to large loop around edge of array

A single plaquette may screen flux from itself up to³

$$B_{\max} = \Phi_0 \beta_\ell / 2\pi a^2 \quad (4.10)$$

In the previous section we discussed how the self inductance of a square loop grows linearly with the size of the loop. Because of this linear dependence on β_ℓ

³Recall, from (2.8), that $\beta_\ell = 2\pi L I_c / \Phi_0$ in which L is the self inductance of a single plaquette and I_c is the critical current of a single junction.

a large current loop around a $M \times N$ array can screen a maximum external field of

$$B_{\max} = \frac{\Phi_0 \beta_\ell}{2\pi a^2 (NM)^{1/2}}, \quad (4.11)$$

which assumes that $M \approx N$.

4.4.3 Screening due to single plaquettes

The second possibility for screening in the array is that each individual plaquette screens flux from itself. As mentioned above, the maximum external field screened from a single plaquette is

$$B_{\max} = \Phi_0 \beta_\ell / 2\pi a^2. \quad (4.12)$$

In this picture, flux will not penetrate the array until flux is able to penetrate a single plaquette. The maximum field in this case is always greater, and substantially greater for extremely large arrays than the maximum flux of (4.10), making this difference quite easy to discern experimentally. There are two ways to think of the screening in this case. Both of these are shown in Fig. 4.5.

In Fig. 4.5(a) each plaquette of the array sets up a screening current to shield out the external flux. One might assume that the opposing currents internal to the array will cancel, reducing this case to the large loop case shown in Fig. 4.2. However, there is a crucial distinction to be made. The current is flowing in niobium wires of width $10\,\mu\text{m}$, but niobium has a London penetration depth of $900\,\text{\AA}$ at 4.2 K. Fig. 4.6 shows this situation schematically for two adjacent plaquettes. The screening current for one plaquette does not cancel the screening current for the adjacent plaquette because the screening currents are flowing only within the penetration depth, and there is no physical overlap between the two

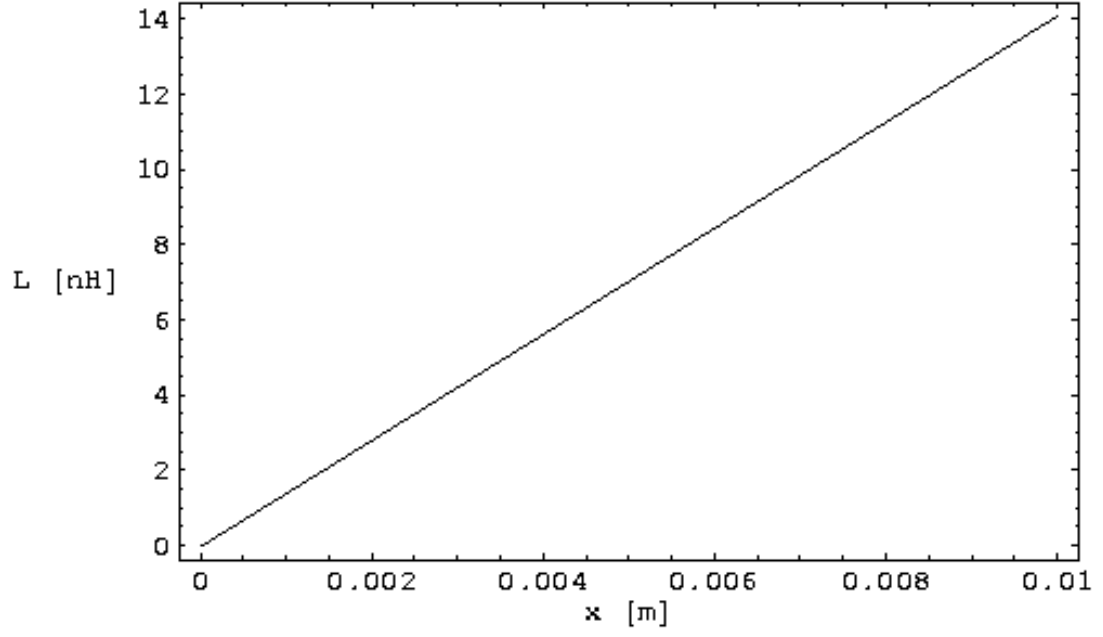


Figure 4.4: Computed self inductance of a square current loop.

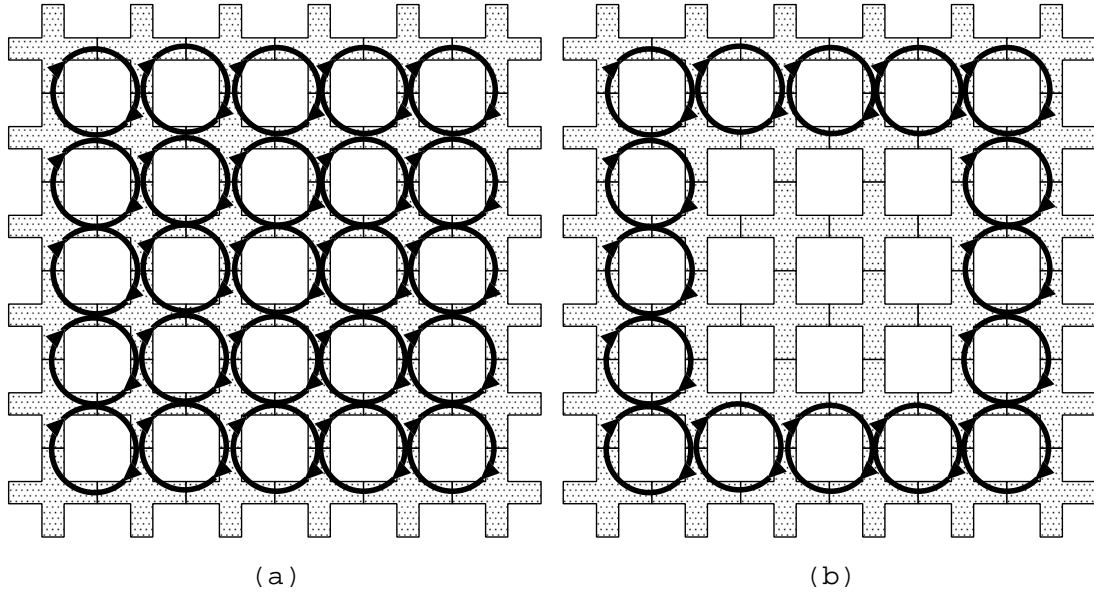


Figure 4.5: Possible different array screening configurations. (a) Every plaquette of the array screening. (b) Only the outside edge plaquettes of the array screening.

currents.

AC susceptibility measurements by Araujo-Moreira *et al.*[11] demonstrated the distinction between large loop screening and single plaquette screening and showed that the arrays generate single plaquette screening. They showed that the array did not respond hysteretically to a driving external field until the amplitude of the external field was increased above approximately four flux quanta per unit cell. For the $\beta_\ell = 30$ used here this indicates that single plaquettes of the array are screening. Furthermore, we have observed the onset of flux penetration into our array, initially in the Meissner state, and noticed that the flux does not penetrate until the external field is ramped from zero to exceed two to four flux quanta per unit cell of the array. By contrast, (4.10) predicts $\Phi_{\max} = 0.09 \Phi_0$ per unit cell.

4.4.4 Outer diamagnetic current

The previous section presented evidence that the array screens flux using the single plaquette screening model, as distinct from the large loop screening model. We observed (*c.f.* Fig. 3.7 and Fig. 3.9 in all of the field-cooling images that the array always generated a diamagnetic screening current around the outside edge. To generate an overall diamagnetic screening current, and have each plaquette screen individually, one may initially think that the array behaves as is shown schematically in Fig. 4.5(a). We discussed previously how the currents do not cancel in this model. However, the currents are confined within the wires, which are $10 \mu\text{m}$ wide, and we cannot resolve features smaller than about $50 \mu\text{m}$ so we cannot identify these currents internal to the array.

To generate the configuration in Fig. 4.5(a) we find that the energy stored

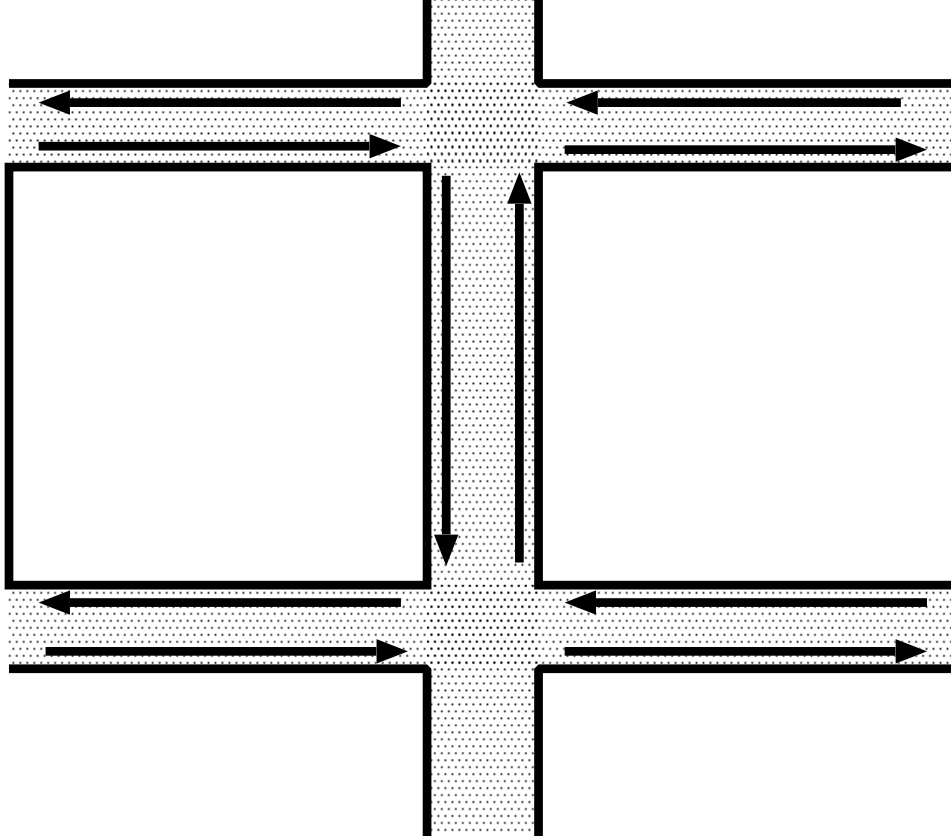


Figure 4.6: Close up view of two adjacent plaquettes with screening currents. The geometry is for our experimental array. The wire width is $10\,\mu\text{m}$ and the penetration depth for niobium is $900\,\text{\AA}$. Because of the difference of the length scales, the internal currents (indicated by the arrows) do not cancel, and the array must actually generate a loop of current flowing around each plaquette

magnetically due to all the plaquette current loops in the array is

$$E_{\text{mag}} = NM \frac{1}{2} LI^2. \quad (4.13)$$

Additionally, there is a Josephson energy contribution to the energy from the junctions around the outside edge of the array

$$E_{J\text{tot}} = 2(M + N) E_J (1 - \cos \gamma), \quad (4.14)$$

in which $E_J = \hbar I_c / 2e$ is the Josephson coupling energy of the junction (note that the currents through the junctions cancel while the currents in the wires do not). This leads to a total energy of

$$E_{\text{tot}} = NM \frac{1}{2} LI^2 + 2(M + N) E_J (1 - \cos \gamma). \quad (4.15)$$

This total energy grows as $N \times M$, and for a large array can be quite substantial.

It turns out that it is possible to screen while having the total energy grow as $N + M$. This screening configuration is shown in Fig. 4.5(b). Here only the plaquettes on the outside edge of the array screen. This creates the observed external diamagnetic screening current. But we end up with a total magnetic energy of

$$E_{\text{mag}} = 2(N + M) \frac{1}{2} LI^2. \quad (4.16)$$

Additionally, there is a contribution due to the Josephson energy in the outside edge junctions, and also from the edge junctions just inside the screening plaquettes, as shown in Fig. 4.5(b).

In the inside edge junctions

$$E_{J\text{tot}} = \{2(N + M) + 2(N + M - 2)\} E_J (1 - \cos \gamma), \quad (4.17)$$

yielding a total energy of

$$E_{\text{tot}} = 2(N + M) \frac{1}{2} LI^2 + \{2(N + M) + 2(N + M - 2)\} E_J (1 - \cos \gamma). \quad (4.18)$$

This energy is smaller than the energy in the previous case, (4.15), in which all of the plaquettes screen. As the size of the array grows, this energy becomes more favorable (*c.f.* $N + M$ *vs.* $N \times M$).

Comparing (4.15) and (4.18) with the assumption that the gauge invariant phase difference is proportional to the total flux and that the array is square (*i.e.* $N = M$) we deduce that it will be energetically favorable for the array to screen with only the outside edge plaquettes when

$$\beta_\ell > \frac{4N - 1}{N^2 - 4N}, \quad (4.19)$$

valid for all $N > 2$. For the arrays we consider, this criteria is easily satisfied.

4.5 Consequences of edge loop screening

In the case shown in Fig. 4.5(b), with only the edge loops screening, in addition to the diamagnetic screening current flowing immediately around the outside edge, there also is a paramagnetic current flowing just inside the outside edge. This paramagnetic current is closer to the interior of the array than the diamagnetic current. The interior plaquettes of the array will respond to both the diamagnetic current and the paramagnetic current, but the paramagnetic current is closer to the interior plaquettes, so it will dominate the response of the interior plaquettes. Fig. 4.7 schematically shows this situation, depicting the external diamagnetic screening current and the interior paramagnetic current.

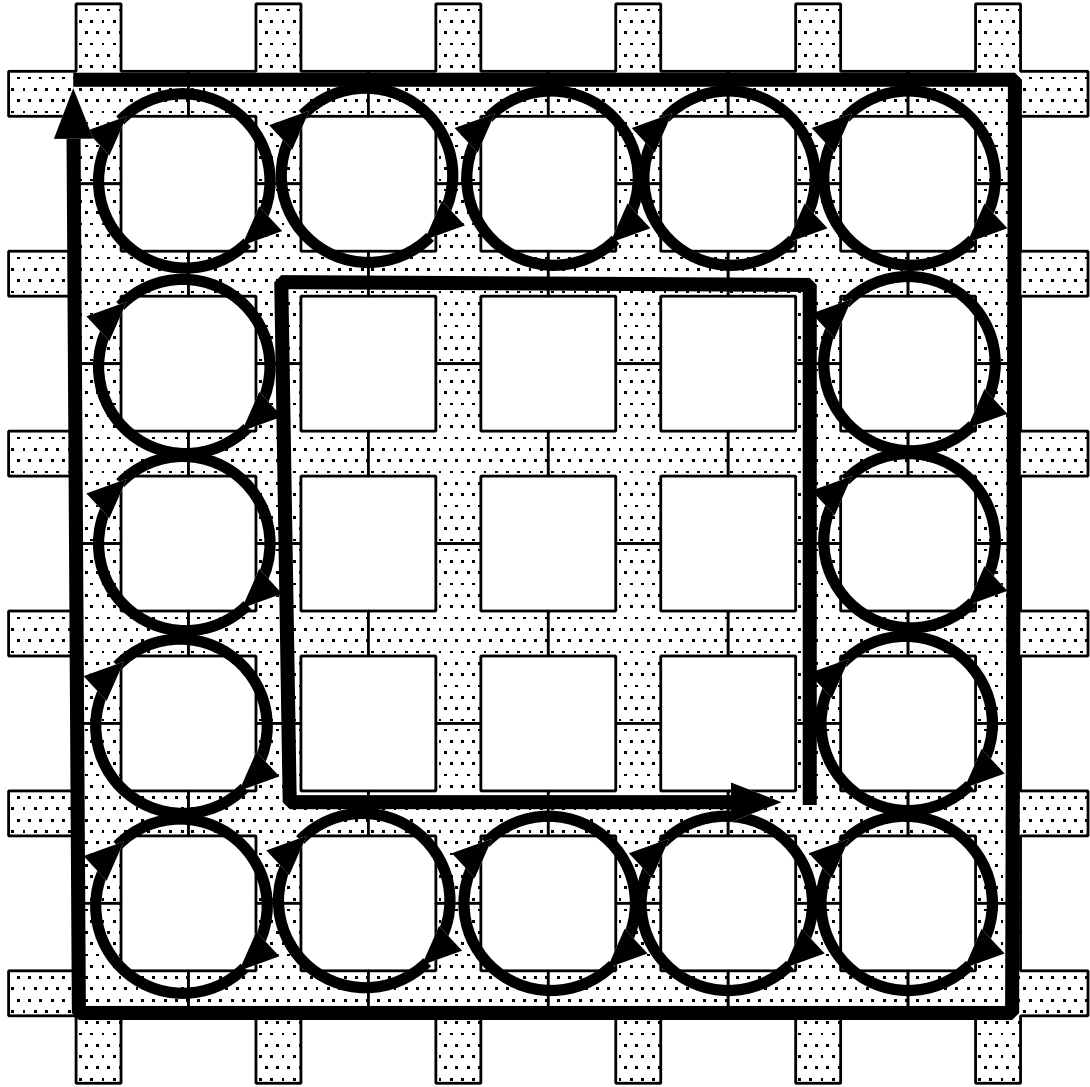


Figure 4.7: Schematic of interior and exterior plaquettes, with screening provided by external plaquettes only. The diamagnetic screening current flows around the outside edge of the array, while the paramagnetic current flows just inside the edge of the array.

4.5.1 Internal plaquette response to fields generated by external plaquettes

Simplistically each interior plaquette sees a field made up of the external field applied to it plus fields due to the diamagnetic and paramagnetic currents discussed above. The external flux that each interior plaquette sees is the real external flux, plus a flux contribution due to the edge plaquette currents, Φ_{screen} . If we analyze the interior plaquettes as single loops (chapter 2) the external flux we need to use is slightly modified

$$\Phi_{\text{ext}} \rightarrow \Phi_{\text{ext}} + \Phi_{\text{screen}}. \quad (4.20)$$

If we apply this modification to the magnetization relation for a single loop, shown in Fig. 2.4, we see that the entire magnetization curve for the single loop is shifted upward so that the single loop will more often be *paramagnetic*.

4.5.2 Array response to external field plus screening fields

We computed the screening flux over the entire interior of the array of the 30×100 array and determined the shift in the magnetization of each interior plaquette. We found that the minimum induced magnetization occurs in the central plaquette of the array and is approximately $\Phi_{\text{mag}} = 0.15 \Phi_0$. Furthermore, we determined the average induced magnetization over the entire interior of the array, and determine it to be $\langle \Phi_{\text{mag}} \rangle = 0.27 \Phi_0$. These numbers compare favorably with the observed average magnetization numbers seen in the array (*c.f.* Fig. 3.14).

Of course, this simple model does not capture many other important features experimentally observed in the array. It does not explain *e.g.* the apparent random distribution of flux over the interior of the array. Quite the contrary, it

predicts that the paramagnetism should be strongest near the edges of the array, and weakest in the center of the array. Furthermore, this simple model predicts that the array interior should be entirely paramagnetic while we observe that there are diamagnetic regions in the array interior. The ingredient missing from the simple model is that all the plaquettes influence each other – it is too simple to assume that only the edge plaquettes influence the interior ones.

4.5.3 Numerical array simulations

Numerical simulations of an array system, with no π -junctions, similar to ours, using the RCSJ model for the entire array (*c.f.* chapter 2, section 2.3, p. 21 and Eqns. (2.26) to (2.29)) have been carried out recently [9] and yield results that replicate quite well the experimentally observed flux distribution in the array.

In this simulation, De Leo *et al.* take a 10×40 Josephson-junction array and model the experiment by increasing in small steps

$$\beta_\ell = \frac{2\pi}{\Phi_0} L I_c(T) \quad (4.21)$$

and

$$\beta_c = \frac{2\pi}{\Phi_0} I_c(T) R^2 C \quad (4.22)$$

from zero at T_c to their final values at $T = 4.2$ K. By holding all the parameters constant except for I_c this amounts to increasing I_c as the temperature decreases. For the resistance R of the junction we chose the sub gap resistance, which gives a value of $\beta_c = 66$ at 4.2 K. The material parameters for our Josephson-junction array samples were discussed in section 3.2, p. 29 and we also used $\beta_\ell = 30$ at 4.2 K.

Fig. 4.8 shows the results of a field cooling simulation for a 10×40 Josephson-

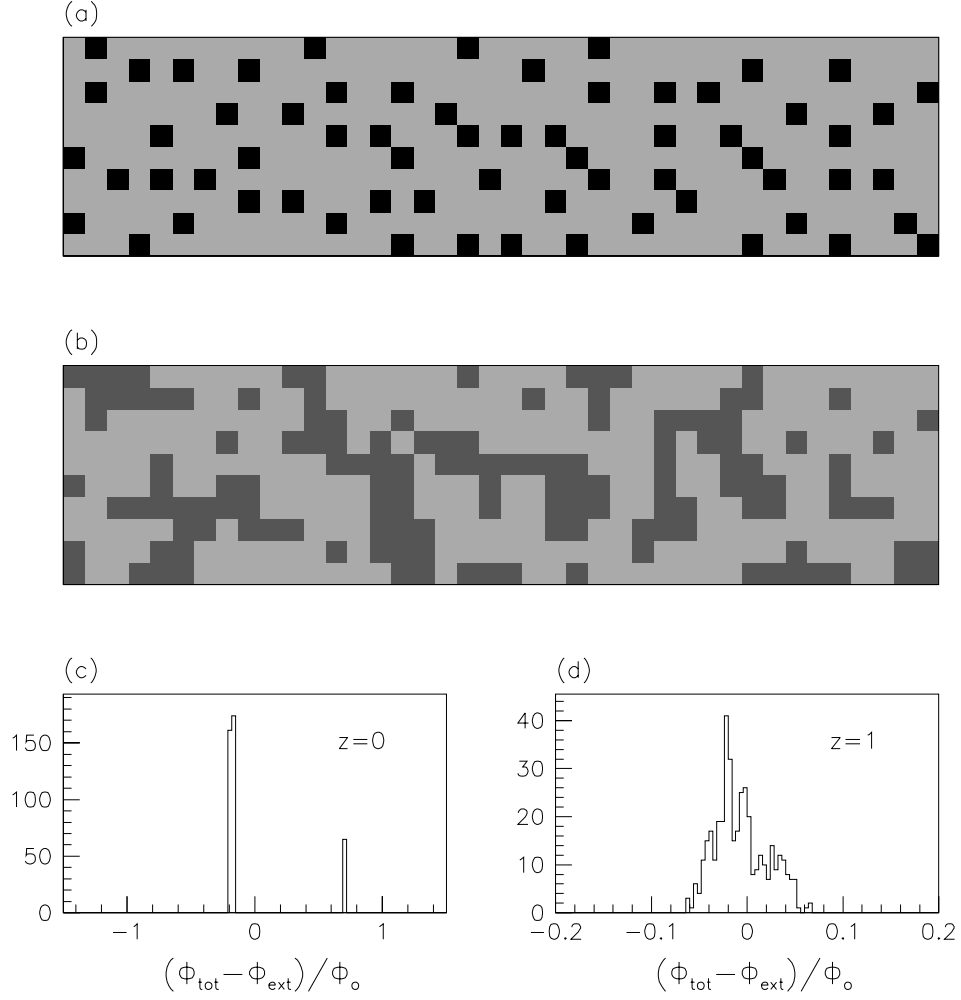


Figure 4.8: Modeled array magnetization for a 10×40 Josephson-junction array, field cooled in $\phi_{\text{ext}} = 4.8$. Dark grey represents paramagnetic plaquettes and light grey represents diamagnetic plaquettes. (a) The array magnetization at the surface of the array. (b) The array magnetization as measured at a height of one unit cell above the array. (c) Histogram of the array magnetization at the surface of the array. (d) Histogram of the array magnetization at a height of one unit cell above the array.

junction array. Dark grey represents paramagnetic plaquettes and light grey represents diamagnetic plaquettes. Fig. 4.8(a) shows the magnetization as measured at the surface of the array, and Fig. 4.8(c) shows a histogram of the same data. The spatial distribution of the magnetization in (a) is very suggestive of the data we measured (*c.f.* Fig. 3.7 and Fig. 3.9). However, the histogram in Fig. 4.8(c) is quite different from that measured in Fig. 3.8. What's truly striking about Fig. 3.8() however, is that the two peaks correspond almost exactly to the lowest and second lowest Gibbs free energy solutions for the single loop (*c.f.* chapter 2, section 2.2.5, p. 19).

Perhaps more interesting, Fig. 4.8(b) shows the simulated magnetization of the 10×40 array at a height of one plaquette. This is similar to the magnetization that a SQUID might measure at a height of one plaquette. Indeed the SQUID in our experiments was at a height of approximately one plaquette. Interestingly, the histogram shown in Fig. 4.8(d) closely resembles the experimental histogram in Fig. 3.10(.

Furthermore, De Leo *et al.* modeled the external field dependence of the array magnetization, shown in Fig. 4.9. Their results qualitatively resemble the results obtained in Fig. 3.14, providing good evidence that the properties of our array can be replicated simply from the equations describing a Josephson-junction array, without π -junctions.

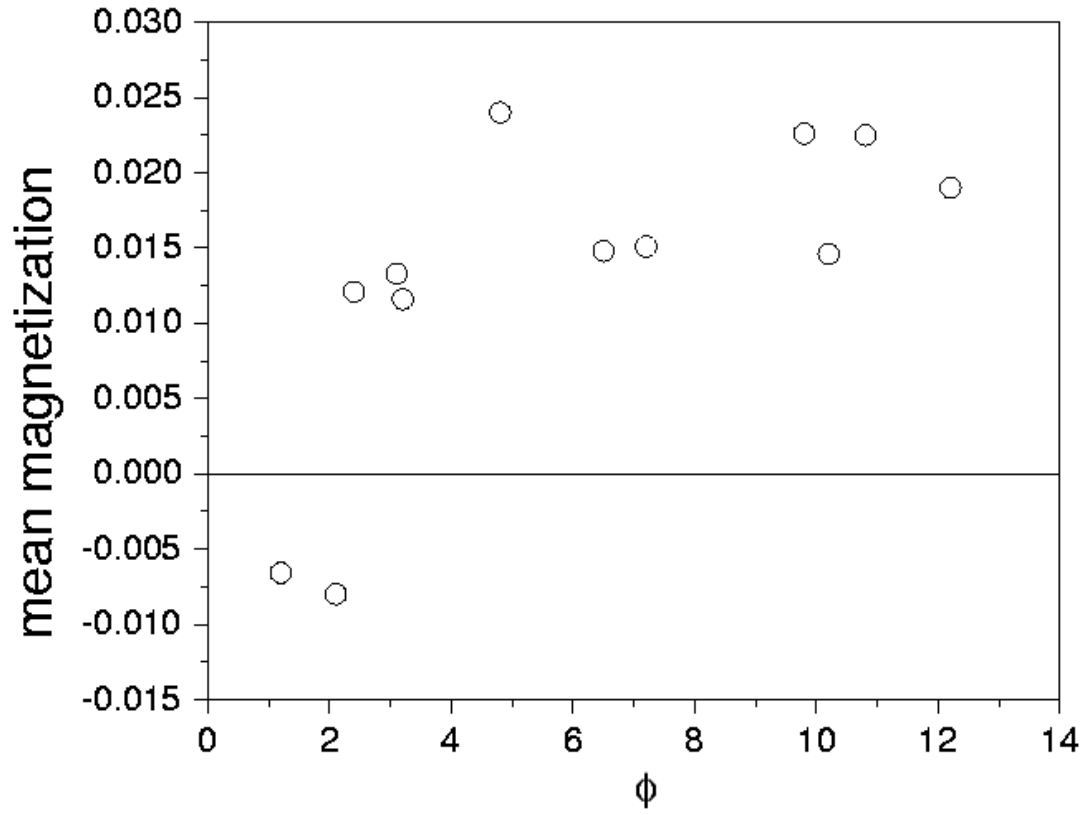


Figure 4.9: Simulated array magnetization *vs.* cooling field for the 10×40 Josephson-junction array. The frustration is Φ_{ext}/Φ_0 per unit cell of the array, and the mean magnetization is $\langle \Phi_{\text{mag}}/\Phi_0 \rangle$ per unit cell of the array.

Chapter 5

Magnetic penetration into $\text{YBa}_2\text{Cu}_3\text{O}_{7-\delta}$ thin films

5.1 Introduction

Substrates for superconducting thin films, which can be formed into arbitrarily long wires, similar to the RABiTS technology [59, 60, 61], may have important applications for motors, generators and electrical power transmission lines. It is therefore important to understand how such materials and superconductors deposited upon them respond to external magnetic flux. Additionally, because of their long, thin geometry, such deposited superconducting materials have an extreme demagnetizing factor ($\eta \rightarrow 1$) which causes the effective field at the edge of the sample to be greatly enhanced as compared to the applied field. This means that even small magnetic fields may have a strong affect on such materials.

5.1.1 Rolling-assisted, biaxially-textured structures

Rolling-Assisted, Biaxially-Textured Structures (RABiTS™)[59, 60, 61] have proven an interesting substrate for study. Conceived at Oak Ridge National Lab,¹ a RABiTS substrate is essentially a tape of nickel, with some buffer layers, carefully prepared so that the deposited superconductor (typically YBCO) has nearly perfect grain alignment. The YBCO films typically have a thickness of 1 μm and critical current densities of one to three mega-amps per centimeter squared.

Originally we were provided samples of YBCO on RABiTS in order to explore ways to increase the critical current density of the YBCO films. However, we soon found it useful to examine YBCO deposited simply on strontium titanate (STO), under the same conditions as the YBCO films on RABiTS. In this chapter we first discuss our examination of the RABiTS films and why we subsequently chose to look at YBCO deposited on STO.

An optical image of the YBCO/RABiTS sample² is shown in Fig. 5.1(a), from which one can glean many of the important parameters of the deposited YBCO film. The image shows the middle section of a sample that measures *in toto* 15 mm long. Additionally, because the sample substrate is primarily nickel and magnetized, the substrate curls up a bit, causing the sample to move out of camera focus in the image at the top and bottom edges. The sample also curls up slightly along the length of the sample, which is not evident in the image. Because of this curl, we mounted the sample using crystal binder to hold it flat onto a silicon wafer, in order to keep the sample level when positioned in the SSM probe.

¹We are grateful to H. R. Kerchner of Oak Ridge National Lab for providing the samples discussed in this chapter.

²ORNL sample designation f153cn6.

The sample in the image measures 3 mm from top to bottom. In particular we note that the YBCO grain size is about $50\text{ }\mu\text{m}$ and that there are small (diameter less than $10\text{ }\mu\text{m}$) holes in the YBCO film. These holes are not mentioned in any of the literature concerning YBCO on RABiTS. For comparison YBCO grown on STO using the same method (pulsed laser deposition) shows none of these small pinholes (*c.f.* Fig. 5.1(b)).

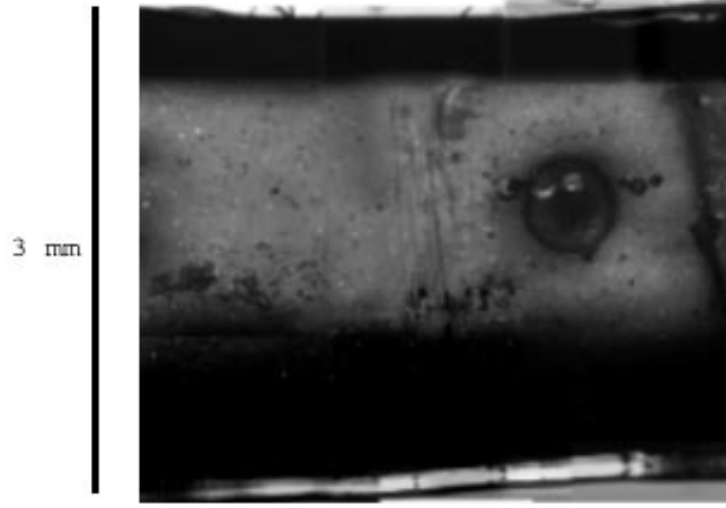
5.1.2 Magnetic penetration into YBCO films

Because RABiTS samples are deposited on nickel, they are ferromagnetic from room temperature down to 4.2 K. In order to distinguish properties of the YBCO films from properties of the RABiTS we also looked at magnetic penetration into YBCO films deposited on STO. An optical image of this sample is shown in Fig. 5.1(b). This particular sample³ is YBCO deposited on STO using the same deposition parameters used in making the YBCO on RABiTS sample discussed previously. Additionally, the YBCO/STO sample has been etched in the center to form a small microbridge in the center.

For our discussions, we use the sample geometry defined in Fig. 5.2, in which we apply the magnetic field along the z axis, parallel to the thickness d of the film. The width of the sample extends from $-W < x < W$ and the length of the sample extends in the y direction.

There has been significant theoretical discussion of this problem, in several different limits related to the film thickness and width. In the extreme thin film limit (film thickness much less than the penetration depth) Larkin and Ovchinnikov [62] made the first calculations and derived the integral equations necessary to

³ORNL sample designation 1a100899.



(a)



(b)

Figure 5.1: (a)Optical micrograph of YBCO deposited on RABiTS. The grains are observable and are about $50\text{ }\mu\text{m}$ across. Additionally, there are small holes evident in the film. These small holes are approximately $100\text{ }\mu\text{m}$ apart. (b) Optical micrograph of YBCO deposited on STO. There are none of the pin holes evident in the RABiTS image. This sample has a microbridge for transport measurements, patterned into the center via chemical etching. These are montage images, formed from several different pictures: straight horizontal and vertical lines are artifacts and not real features of the samples.

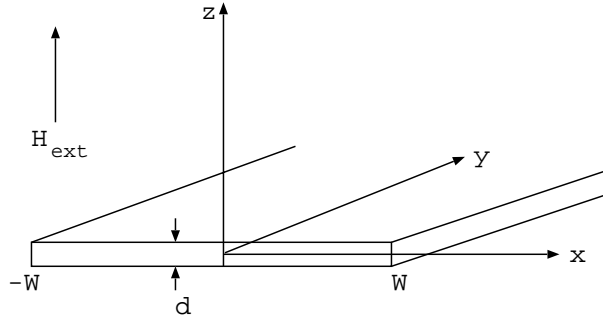


Figure 5.2: Sample geometry used in the experiment and discussion. The external field is applied along the z -axis, through the thickness of the film d . The sample width extends from $-W < x < W$, $W = 1.5 \text{ mm}$ and we treat the sample as infinitely long in the y direction.

be solved for the current distribution in the Meissner state. The geometry is as described above, with the sample infinitely long in the y direction, and a current distribution dependent only upon x . Dorsey [63] took the integral equations and derived analytic results valid over the entire width of the superconductor. For thicker films (film thickness comparable to or larger than the penetration depth) Brandt [64, 65, 66] and Brandt and Mikitik [67] have made considerable numerical progress in describing the current distributions over the cross-section of a superconducting slab and finally Vodolazov and Maksimov [68] have computed analytic expressions for the current distributions. Up to now, there have been no reported measurements of the current distribution nor magnetic field distribution in superconducting films in the Meissner state.

The onset of flux penetration into a superconducting slab has also been of considerable interest. There exists a large body of theoretical work, from the geometrical barrier ideas of Zeldov *et al.* [2] to the edge pinning ideas of Kuznetsov *et al.* [69] which discuss remanence in a superconducting slab. Furthermore, there have been experimental studies of the Bean critical state in a superconducting slab by Johansen *et al.* [70] using magneto optical indicator films (MOIF) and by Ferdeghini *et al.* [71] using a scanning Hall probe. (Because of the large demagnetizing factor, initial flux penetration occurs for very low applied fields and neither of these techniques are sensitive to fields in this range.)

5.2 YBCO on RABiTS

RABiTS tapes are primarily nickel [59, 60, 61] and it has been previously reported that they contain a Landau type domain structure [72, 73] in their cross-section. It is now known that this domain structure cannot exist [74, 75], so we do not

expect to find this type of domain structure. In fact, we do not find any sort of simple magnetic domain structure. We imaged a RABiTS substrate⁴ without any superconducting layer deposited, shown in Fig. 5.3, and we estimate the height of the SQUID to be between fifty and one hundred micrometers for this scan. It is clear from the image that the sample is tilted with respect to the plane of the SQUID. In the image, the signals are much clearer and stronger near the right side of the image, but fade out near the left edge of the sample. (We know the sample is tilted by making contact with the SQUID at different points and noting the difference in contact height.) The magnetic image clearly demonstrates that the spontaneous magnetization of the RABiTS film is very complicated. We did not attempt to demagnetize or magnetize the substrate in any particular fashion because we wanted to image the sample as it would (presumably) be if it were used commercially, as there is no discussion of special magnetic preparation in the literature.

Because of these measurements we realized that, using this type of substrate, we would be able to cool the sample in zero *external* field, but that the superconductor would always see an extremely strong field due to the magnetization of the substrate. Hence, the superconductor deposited on RABiTS cannot be cooled in zero field. We demonstrate this by showing, in Fig. 5.4, a nominally zero-field cooled image of YBCO deposited onto RABiTS. There have been reports claiming to observe a geometrical barrier [2] in YBCO/RABiTS [73]. However, it is not clear that this should be the case since the YBCO film on RABiTS never sees a uniform external field, and further because of the holes in the sample we expect flux pinning to be quite strong; the geometrical barrier requires extremely

⁴ORNL sample designation n020898.

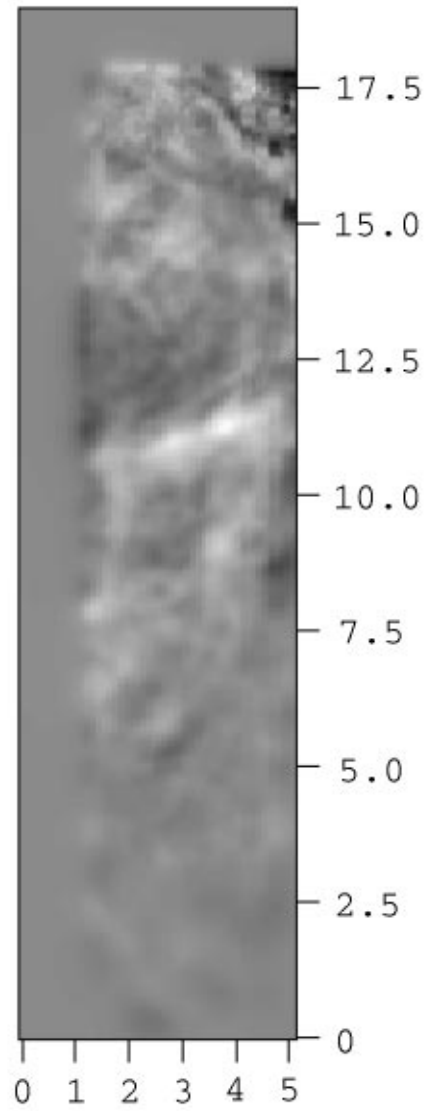


Figure 5.3: Magnetic image of bare RABiTS substrate with spatial units along the axes shown in millimeters. The grey scale ranges from black (low) to white (high) with a difference of 6.75 G. The image was taken at 4.2K. The SQUID height is not constant over the surface of the sample; it is closer on the right, and farther away on the left.

weak pinning (it was first observed in single crystals).

Because of the impossibility of zero field cooling, we decided to look at YBCO deposited onto STO instead of the RABiTS tapes,⁵ and investigate the existence of the geometrical barrier.

5.2.1 RABiTS AC susceptibility

In order to understand the basic mechanism involved with loss in YBCO on RABiTS when carrying current, we used the SQUID to perform a local measurement of the AC susceptibility at 500 Hz and 1 kHz. We use the same experimental arrangement shown in Fig. 3.2, except that instead of applying a DC field with the solenoid, we apply an AC field. We use an EG&G model 5210 lock-in amplifier[76] to measure the applied frequency component in the output from the SQUID electronics. From the lock-in amplifier we acquire two spatially resolved signals, the in phase component and the out of phase component

We can relate these two components to the real and imaginary parts of the AC susceptibility for the sample. In general the susceptibility is defined from $\vec{H} = \vec{\chi}\vec{M}$, in which $\vec{\chi}$ is the susceptibility, a tensor quantity, \vec{H} is the magnetic field, \vec{M} is the magnetization of the sample. If we assume that material is linear and isotropic, then $\chi = H/M$ and for a superconductor in the Meissner state $\chi = -1$.⁶

⁵See section 5.3, p. 104.

⁶We strive to use MKS units, in which the proper field relationship for various magnetic quantities is $\vec{B} = \mu_0(\vec{H} + \vec{M})$, throughout this discussion. A very useful chart for conversion between different electromagnetic unit systems is in Jackson [58], p. 819.

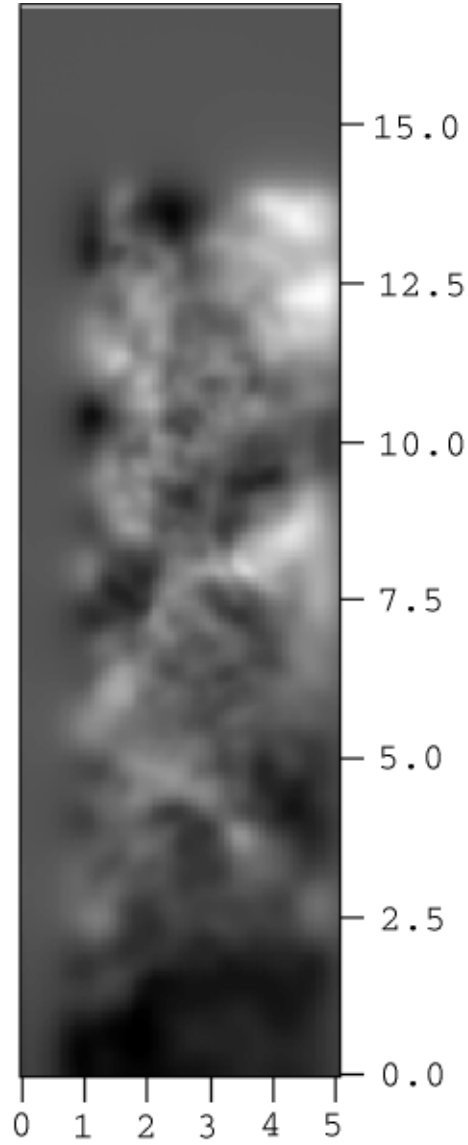


Figure 5.4: Magnetic image of YBCO on RABiTS, cooled in zero external field to 4.2 K, with the spatial units along the axes shown in millimeters. The grey scale runs from black (low) to white (high) with a range of 4.75 G. The plane of the sample is tilted with respect to the plane of the SQUID, causing the SQUID to be closer to the sample in the right of the image. This causes the image to appear washed out at the left hand side of the image.

The sample sees an external driving field of

$$H_{\text{ext}}(t) \hat{z} = H_{\text{ac}} \cos(\omega t) \hat{z} \quad (5.1)$$

The \hat{z} component of the sample magnetization may be expressed as a series of Fourier components related to the drive frequency, $\omega/2\pi$,

$$M(t) = H_{\text{ac}} \sum_{n=1}^{\infty} [\chi'_n \cos(n\omega t) - \chi''_n \sin(n\omega t)] \quad (5.2)$$

in which $\chi_n = \chi'_n + i\chi''_n$ is the complex susceptibility at each frequency component, $n\omega/2\pi$. We discuss only the first component, $n = 1$, (hereafter referred to as χ) though harmonic generation has been studied in some detail by others in bulk measurements [77, 78].

We measure with the lock-in amplifier two components at the driving frequency, $\omega/2\pi$, one which is in phase with the driving field and one which is $\pi/2$ out of phase with the driving field. These two components correspond to the real and imaginary components of χ . The real part, χ' , corresponds to Meissner screening currents within the sample, which are not lossy and the imaginary part, χ'' , corresponds to processes which cause loss, eddy currents in the substrate and hysteretic process in the superconductor or substrate.

We used a driving amplitude of 223 mOe for these measurements. A comparison of the sample response is shown in Fig. 5.5 and Fig. 5.6 for two excitation frequencies. The signals in these images consist of the YBCO response and the nickel response. In general the response of both the media must be considered together in a self-consistent manner, but we will discuss the effects separately first and some simplifications to the self-consistent problem second.

We can understand the eddy current generation in the substrate by considering Maxwell's equations and Ohm's Law. We start by taking the curl of Ohm's

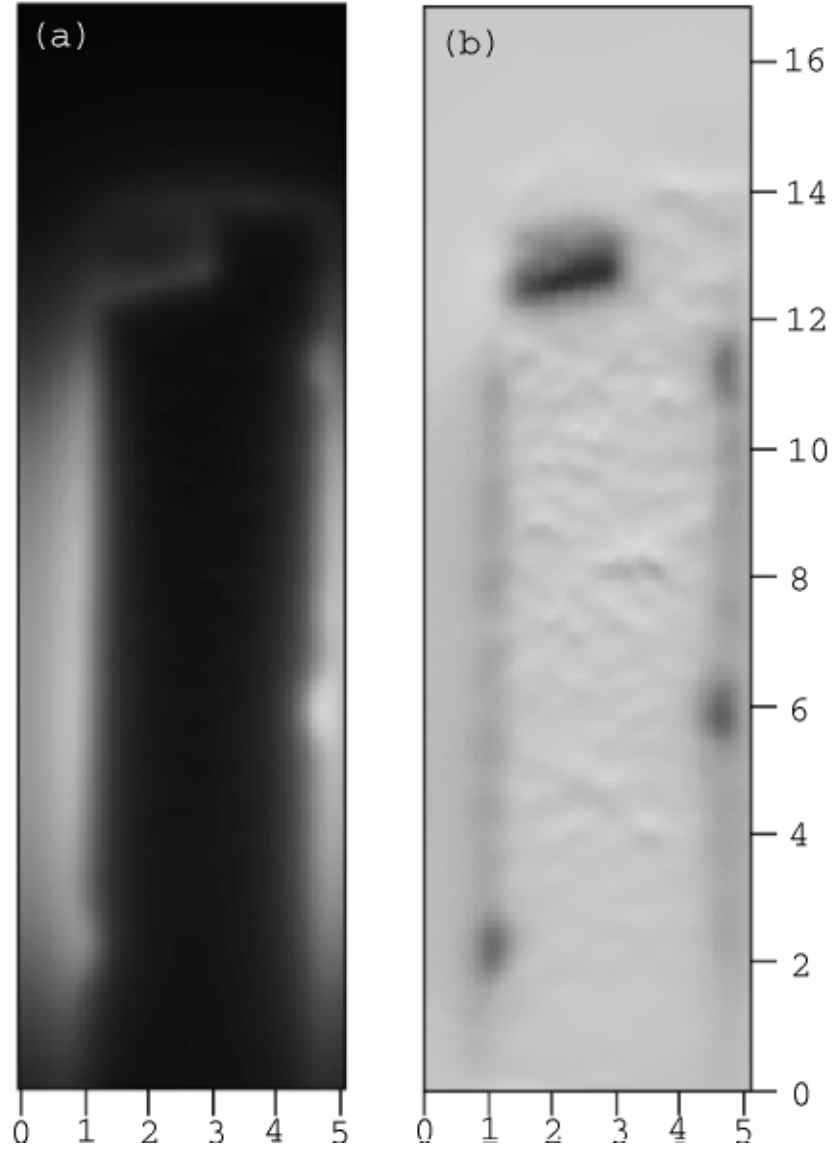


Figure 5.5: AC susceptibility images for the YBCO on RABiTS sample, zero-field cooled to 4.2 K, for an external excitation frequency 1 kHz and an amplitude of 223 mOe. The spatial dimensions along both axes are in millimeters. (a) The χ' image whose grey scale ranges from -0.015 G (black) to 0.25 G (white). (b) The χ'' image whose grey scale ranges from -0.045 G (black) to 0.01 G (white).

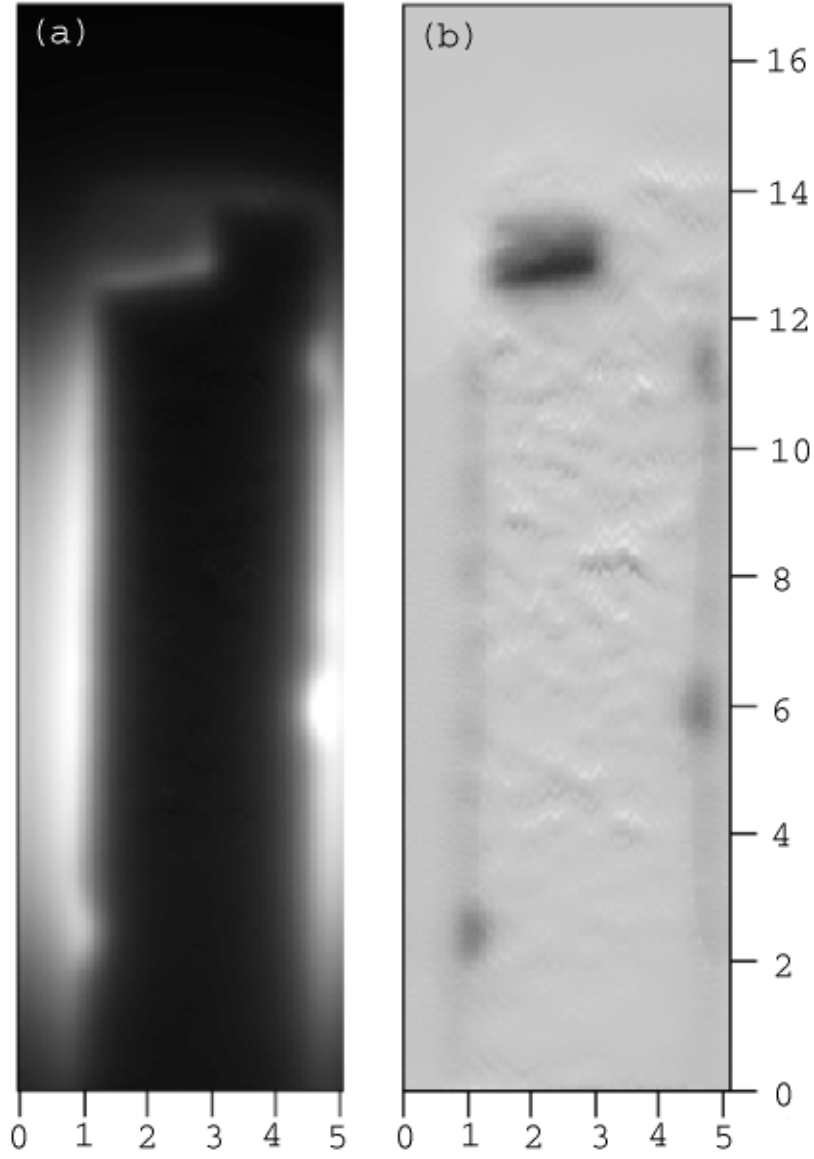


Figure 5.6: AC susceptibility images for the YBCO on RABiTS sample, zero-field cooled to 4.2 K for an external excitation frequency 500 Hz and an amplitude of 223 mOe. The spatial dimensions along both axes are in millimeters. (a) The χ' image whose grey scale ranges from -0.015 G (black) to 0.25 G (white). (b) The χ'' image, whose grey scale ranges from -0.045 G (black) to 0.01 G (white).

Law which gives

$$\nabla \times \vec{J}(\vec{x}, t) = \sigma \nabla \times \vec{E}(\vec{x}, t) = -\sigma \frac{d}{dt} \vec{B}(\vec{x}, t). \quad (5.3)$$

Additionally, we assume that the material response is linear so that $\vec{B}(\vec{x}, t) = \vec{B}(\vec{x})e^{i\omega t}$ and $\vec{J}(\vec{x}, t) = \vec{J}(\vec{x})e^{i\omega t}$ which we substitute into (5.3) to get

$$-\nabla \times \delta^2 \vec{J}(\vec{x}) = \frac{i}{\mu_0} \vec{B}(\vec{x}) \quad (5.4)$$

in which $\delta = \sqrt{1/\mu_0\sigma\omega}$ is the skin depth,⁷ μ_0 is the permeability of free space, σ is the conductivity of the material, $\omega/2\pi$ is the driving frequency, $\vec{J}(\vec{x})$ is the induced eddy current and $\vec{B}(\vec{x})$ is the total magnetic induction. It's clear that the eddy current is out of phase with the drive field by a phase of $\pi/2$, which is why we expect the field generated by the eddy currents to affect the χ'' signal.

It's interesting to note the similarity between (5.4) and the London equation (in MKS units)⁸

$$-\nabla \times \lambda^2 \vec{J}(\vec{x}) = \vec{B}(\vec{x}) \quad (5.5)$$

in which λ is the London penetration depth, $\vec{J}(\vec{x})$ is the Meissner current and $\vec{B}(\vec{x})$ is the total magnetic induction. In our geometry, the shape of the current distribution $\vec{J}(\vec{x})$ will be the same for both (5.4) and (5.5). The primary difference is that the eddy current screening is out of phase with the drive field, while Meissner current screening is in phase with the drive field (and the Meissner current may flow at DC).

⁷This skin depth differs from the skin depth as conventionally defined by a factor of $\sqrt{2}$, see Jackson[58], p. 298 or Panofsky and Phillips[79].

⁸See Tinkham[4], p. 4 for the London equations. We have neglected the time dependence of \vec{J} and \vec{B} . In general these are time dependent quantities, but here we consider the DC Meissner response.

As discussed above, we expect to see the eddy current response of the nickel in the χ'' image. However, the nickel is below (and hence screened) by the YBCO, so we do not necessarily expect the nickel to actually see the driving field and respond, except in regions where the YBCO fails to screen. In fact this is exactly what we see. In Fig. 5.5(a), which shows χ' , there is a light region in the upper right corner of the sample which does not screen the external field. Darker colors are screening regions in this case because they are closer to zero field. This same region in Fig. 5.5(b), χ'' , shows the strongest response indicating that the YBCO is not superconducting in this region and hence not screening the nickel tape underneath. In addition to this region, there are other regions which have the same correlation between the two images, particularly at the edges of the sample.

We can understand these measurements more quantitatively by considering separately the AC response of the YBCO and the nickel substrate. At our low temperature (4.2 K) and field amplitude (below H_{c1f}), we expect the sample to be in the Meissner state, and so we expect to observe Meissner shielding in phase with the driving field. We could not cool the sample in zero field due to the presence of the substrate. The substrate provides a DC magnetic field, if the pinning in the sample is strong enough, this DC field will be pinned and when we measure AC excitations of the sample, we expect to find a Meissner screening response at the same frequency as the driving field. Line cuts through the χ' magnetic images in Fig. 5.5 and Fig. 5.6 at $x = 9.1$ mm are shown in Fig. 5.7, and qualitatively show the expected Meissner screening form.⁹

In the superconductor itself, we expect to observe losses associated with mo-

⁹We discuss Meissner screening in great detail in section 5.3.2, p. 106. We note here that these AC susceptibility measurements agree with the Meissner state discussion below.

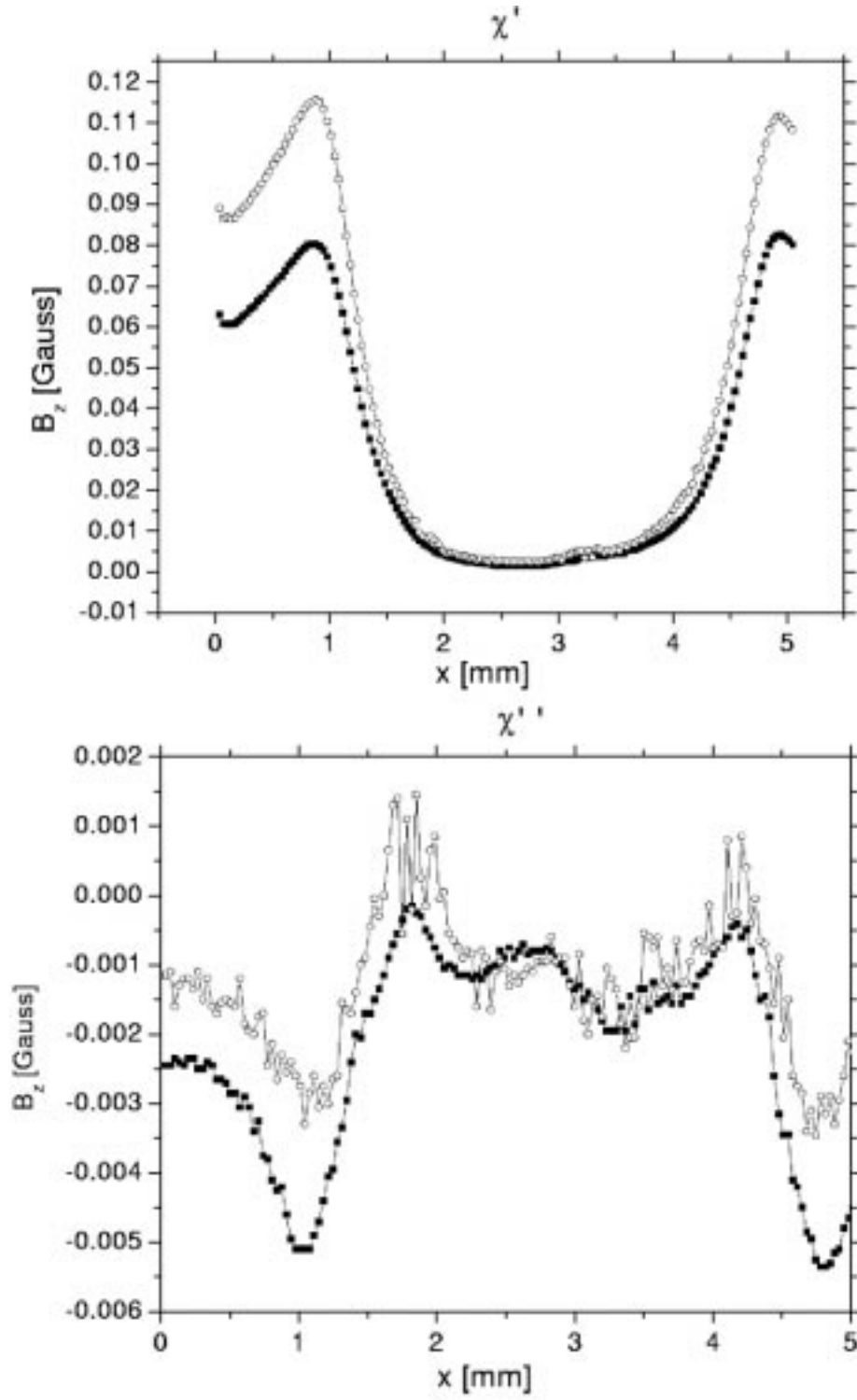


Figure 5.7: χ' and χ'' line cuts through AC susceptibility measurements taken at $x = 9.1$ mm, for 1 kHz (black squares) and 500 Hz (open circles).

tion of flux for any, arbitrarily low, excitation field because the spontaneous magnetization of the nickel assures that flux will always be present in the superconductor. Losses due to vortex motion in a superconductor may result from different processes, flux-flow resistance [80, 81] and intergranular (or grain boundary) vortex motion [82, 83]. It is well known that flux-flow resistance is strongly dependent upon driving frequency.¹⁰ Moreover, it has been reported that losses due to intergranular vortex motion are typically frequency independent [82].

We pointed out previously that because of the large spontaneous magnetization of the nickel that we could not cool the sample in total zero field, so we do not expect the sample to be in the Meissner state. Instead we expect the sample to have a complicated internal magnetic structure, which will respond hysteretically to the excitation field. Hysteretic losses appear in the out of phase image and provide a means to identify lossy regions of the sample. Furthermore, by studying the amplitude and frequency dependence we may determine the cause of the losses in different regions. There are regions near the edges of the sample which have strong loss signals, and no Meissner screening signal. These regions are likely defective YBCO film and the strong loss signal results from the eddy currents in the nickel.

It is difficult to do a systematic study of the sample over a wide frequency and amplitude range because of the time required to generate the different images. None the less, we have made several images at a fixed external amplitude, over a range of frequencies from 500 Hz to 5 kHz. A selection of these images is shown in

¹⁰An analogy can be drawn between flux-flow resistance and eddy current generation in normal metals, which as discussed previously, is proportional to the driving frequency. See Clem [81] for an excellent description and derivation of the analogy.

Fig. 5.5 and Fig. 5.6, with line cuts through these images at $x = 9.1$ mm shown in Fig. 5.7 and Fig. 5.7. From the line cuts in Fig. 5.7 (χ'' or loss images) we notice that there is considerable internal structure and that both line cuts at 500 Hz and 1 kHz are remarkably similar. Furthermore, we notice that the line cuts do not go to zero outside of the sample as they should. This indicates that the phase separation between the in and out of phase signals was incomplete at the lock-in amplifier. None the less, the loss signal is qualitatively frequency independent, indicating that the losses are occurring at the grain boundaries, rather than in the grains.

With losses occurring in the grain boundaries, rather than in the grains themselves (as flux-flow resistance) we expect that the current carrying capacity of the YBCO on RABiTS films may be increased by increasing the size of the grains in the sample. At some point however, the spontaneous magnetization of the RABiTS substrate will become the limiting factor for the losses, inducing flux in the YBCO causing flux-flow losses. These flux-flow losses would continue to occur even if one could engineer a way to deposit a single crystal on the RABiTS.

5.2.2 RABiTS DC hysteresis measurements

In addition to the AC susceptibility measurements we made DC hysteresis measurements on the sample in order to investigate how flux became pinned in the sample. We did this measurement at two different heights above the sample, approximately $50\text{ }\mu\text{m}$ and $20\text{ }\mu\text{m}$, but could only take single line scans at the closer height because of a tilt in the mounted sample relative to the scanning plane.

To generate a hysteresis measurement we take one scan after zero field cooling; ramp the external field up to a specific value; ramp the field back to zero; and

finally reimage the sample. We compare the two images by subtracting the first from the second. The resulting difference image should reveal where flux trapping is hysteric for the particular field.

We show, in Fig. 5.8(a)-(b) the images before and after application of the external field and in Fig. 5.9(a) the difference between Fig. 5.8(a)-(b). The SQUID at a height between $100\text{ }\mu\text{m}$ (however, the sample is tilted, as discussed above for the bare RABiTS substrate) and $50\text{ }\mu\text{m}$ and a peak applied external field of 223 mOe . In addition to the difference image, we compare the magnitude of the gradient of the field in Fig. 5.8(a) $|\nabla_{x,y}B_z|$ (shown in Fig. 5.9(b)) with the difference image in order to verify that the features observed in the difference image are not a result of mechanical misalignment between the two images resulting in a false image. We do this because two images, exactly the same, but offset slightly will produce a difference image which contains the strongest signal near where the gradient of the first two images is largest. It is clear from comparing Fig. 5.9 (a) and (b) that there is some correlation between the two images, indicating that some of the structure is due to misalignment in the probe mechanics.

A simple method to correct for this would be to shift one of the images in x and y before taking the difference, however to simplify this comparison process, we took single vertical line scans over the sample at a horizontal point of 7.5 mm in Fig. 5.8. These single line scans were taken separately from the images discussed above and were arranged so that the sample only moved along the single line during the data collection. In this way the line scans lie atop each other and would only need to be shifted in one direction. These line scans, shifted to match the peaks are shown in Fig. 5.10, for both the zero field cooled and hysteresis scans. It was not possible to match all of the peaks simultaneously. Vertical,

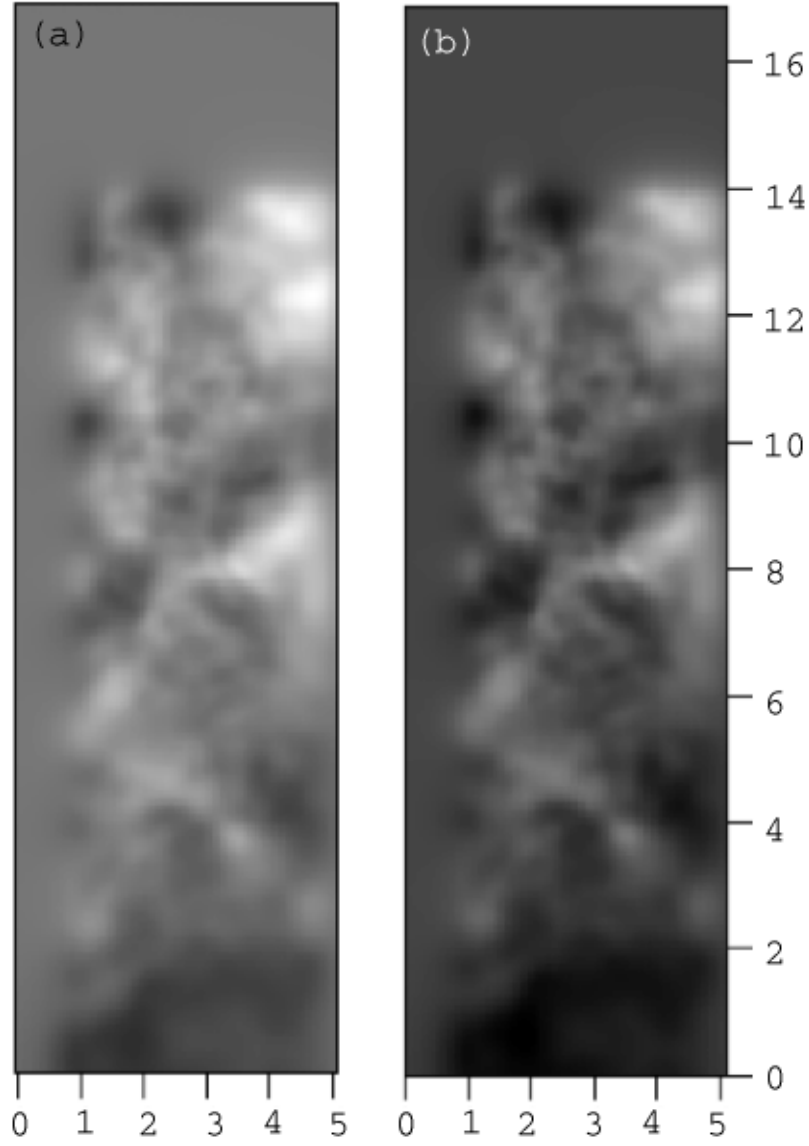


Figure 5.8: Typical images used to study DC hysteresis in the YBCO/RABiTS data at a height of $50\text{ }\mu\text{m}$. (a) Image taken after zero field cooling the sample. The grey scale ranges from low (black) to high (white) with a total range of 5.6 G. (b) Image taken after ramping the external field to 1.16 G and subsequently removing the external field before measuring. The grey scale is the same as (a).

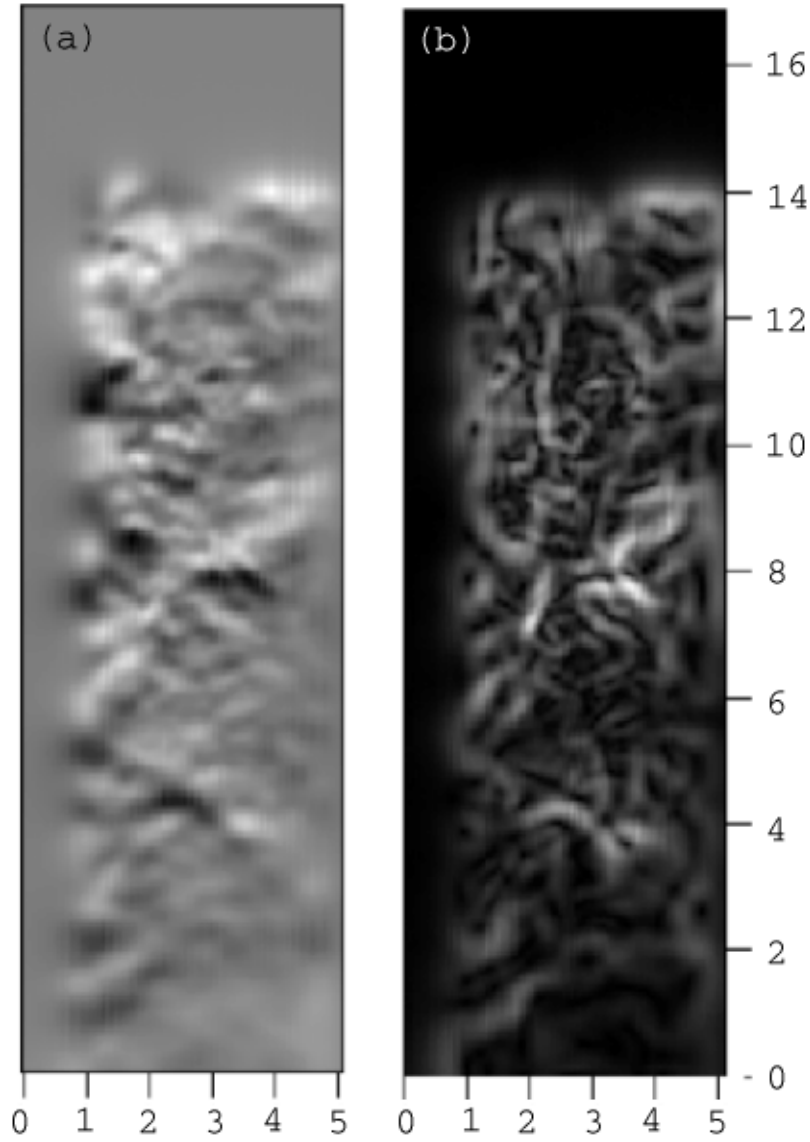


Figure 5.9: Typical images used to study DC hysteresis in the YBCO/RABiTS data at a height of $50\text{ }\mu\text{m}$. (a) Difference image taken by subtracting Fig. 5.8(a) from (b), the grey scale ranges from -1.7 G (black) to -0.35 G (white). (b) Magnitude of the gradient of the image in (a) for comparison with the difference image. The grey scale runs from zero (black) to 7.3 G/mm (white).

numbered lines are drawn in Fig. 5.10 at the location of several peaks. In order to correlate these two line scans we shifted the curves such that peak 1 occurred at the same x value for each. After we did this, the location of peak 2 and 4 did not coincide, however the location of peak 3 did. The difference in the peak coincidence, less than $10\text{ }\mu\text{m}$, indicates that either the mechanical deviations are not linear across the scan or that small flux has shifted within the sample on very small length scales. The difference between these two scan lines is shown in Fig. 5.10 along with the gradient of the zero field cooled line scan for comparison. Both line scans are very similar, except for a small offset which may be due to a flux jump in the SQUID washer between line scans. Furthermore, the gradient of the line scans correlates quite well with the difference between the two line scans, indicating that the difference we are measuring is a result of mechanical misalignment in the scanning mechanism, rather than real hysteresis.

In order to improve upon the line scans taken above, we made line scans at a SQUID height of about $20\text{ }\mu\text{m}$. By using these line scans analogously to the line scans taken at $50\text{ }\mu\text{m}$ (*c.f.* Fig. 5.10) we were able to observe new features in the sample that were invisible at the greater height. These line scans are shown in Fig. 5.11 for the same parameters as the previously discussed line scans.

Again, the same analysis was performed, comparing the zero field cooled line scan to a line scan taken after increasing the external field to 1.16 G and back to zero. Again, for the best comparison of the two, we shifted the zero field cooled image left and right until the peaks matched as closely as possible to the line scan taken after applying the external field. This helps to eliminate potential errors introduced into the difference image because of the gradient of the magnetic field. The gradient and the difference are shown in Fig. 5.11 for comparison. The

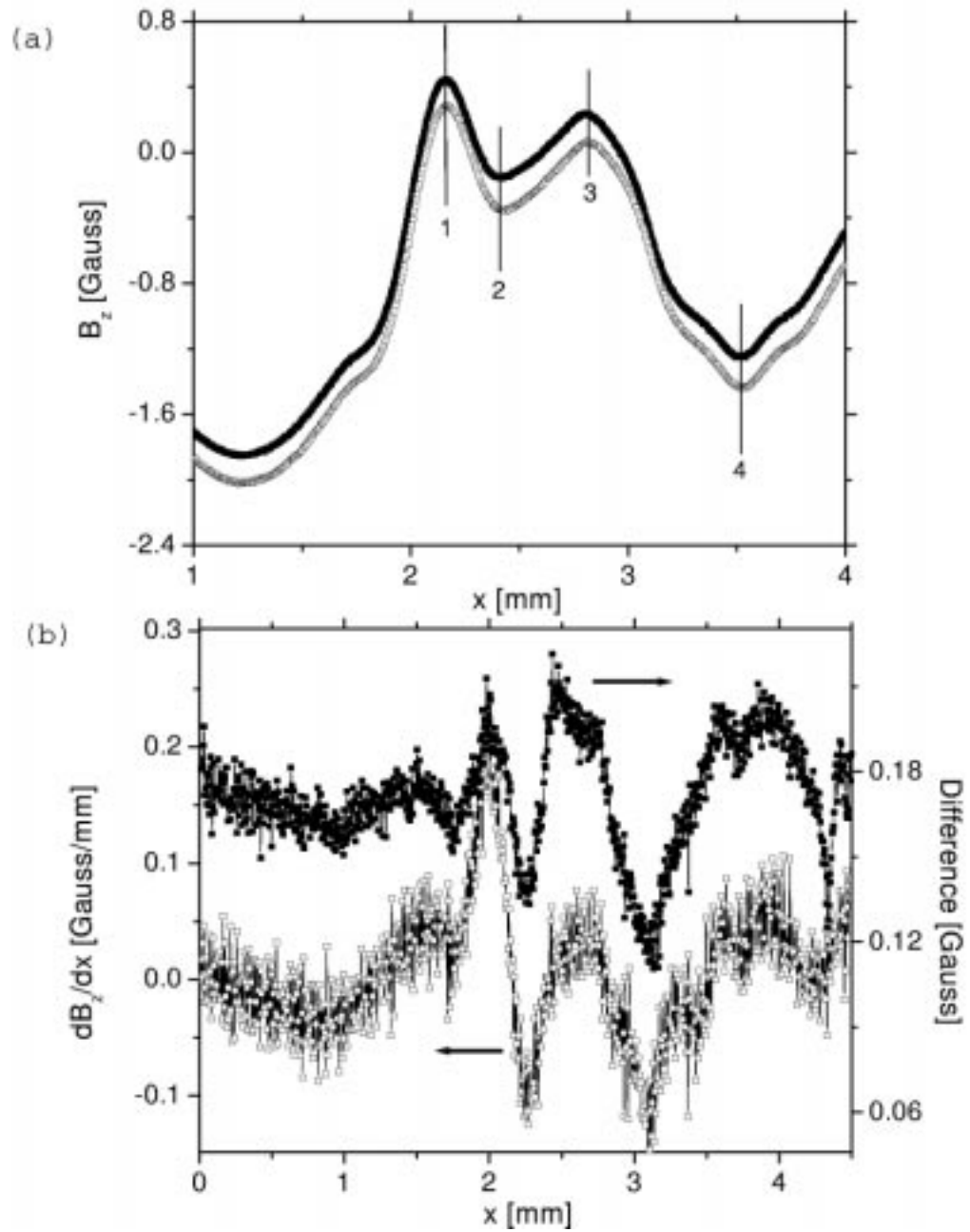


Figure 5.10: (a) Vertical line cuts of DC hysteresis images, with the SQUID at a height of $50 \mu\text{m}$, at $x = 7.5 \text{ mm}$. Zero field cooled line scan (open circles) and line scan after ramping the external field to 1.16 Oe and back to zero (black squares). (b) Difference (black squares) and gradient (open squares) of the vertical line cuts.

correlation between the two is not nearly as strong as in the previous case.

As a better method of comparison, we compare specific locations in Fig. 5.11. First consider the peaks that are quite evident in both line scans in Fig. 5.11 and note that the peaks are typically separated by about $100\text{ }\mu\text{m}$, which is the same average separation between the holes in the YBCO as seen in Fig. 5.1(a). We infer from this that the holes in the YBCO film are harboring pinned flux. Now compare the specific locations in the image indicated by arrows which indicate locations where the height of the peaks has changed between line scans. This change in the height indicates that the amount of flux pinned in that region has changed during the application of the external field.

The comparison of Fig. 5.10 and Fig. 5.11 is quite revealing. With the SQUID at a height of $50\text{ }\mu\text{m}$ there is very little structure in the line scans. The line scans at a height of $15\text{ }\mu\text{m}$ have a very peaked structure, demonstrating that flux is becoming trapped in the sample. In fact, we can compare the distance between the peaks, to the average distance between the holes (*c.f.* Fig. 5.1) which the YBCO/RABiTS sample presents.

5.3 Magnetic penetration into YBCO thin films

5.3.1 Experimental details

Because several authors (*c.f.* Zeldov *et al.* [2] and Kuznetsov *et al.* [69]) predict remanence to occur in different ways (center versus edge pinning of vortices), we studied thin superconducting $\text{YBa}_2\text{Cu}_3\text{O}_{7-\delta}$ films in an external field applied perpendicular to the plane of the sample using a scanning SQUID microscope (SSM) [84]. Furthermore, we know of no experimental measurements of the field

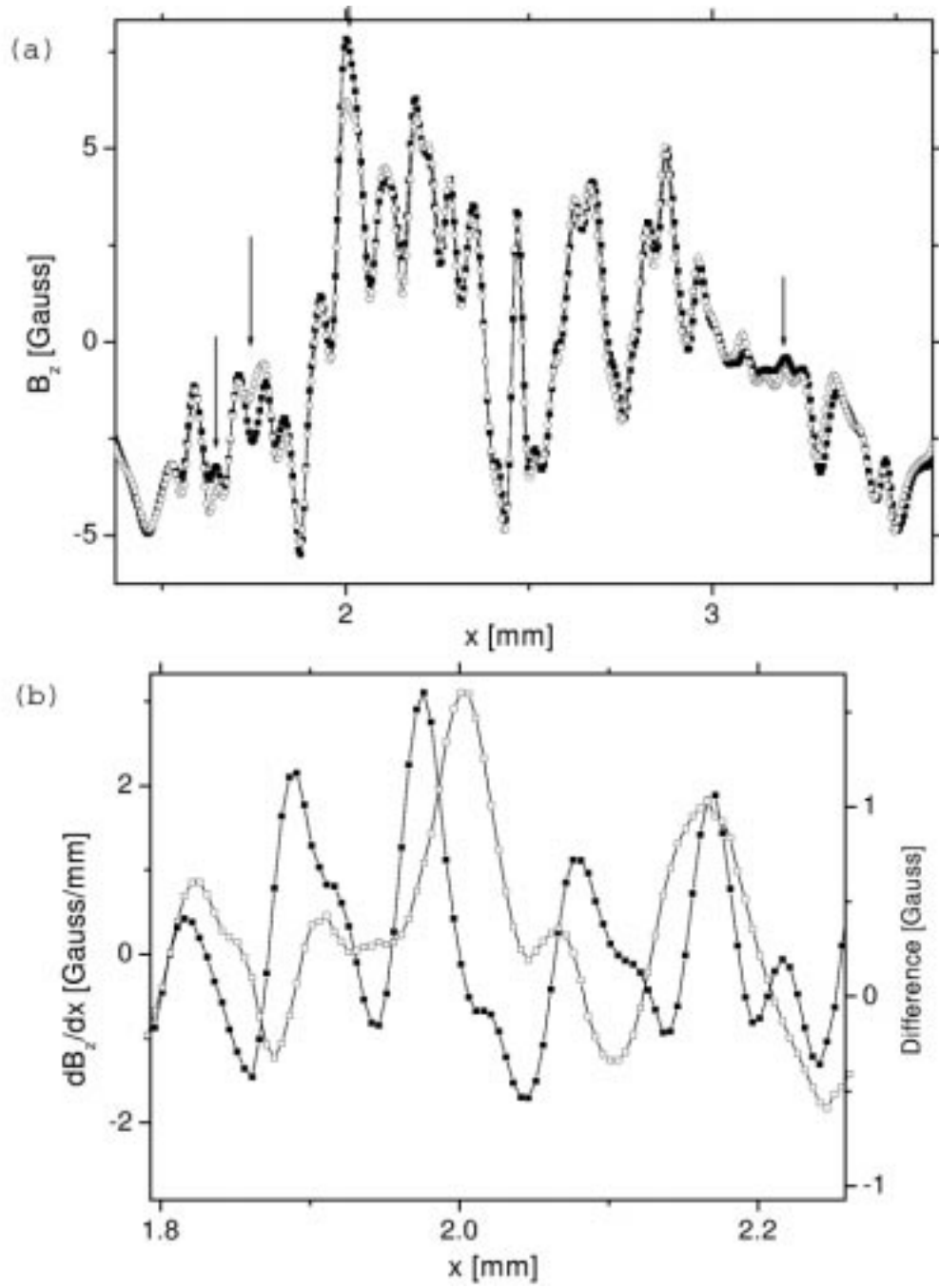


Figure 5.11: (a) Vertical line cuts of DC hysteresis images, with the SQUID at a height of $15\ \mu\text{m}$, at $x = 7.5\ \text{mm}$. Zero field cooled line scan (open circles) and line scan after ramping the external field to 1.16 Oe and back to zero (black squares). (b) Difference (black squares) and gradient (open squares) of the vertical line cuts.

nor current distributions in the Meissner state for a film, such as ours, with a large demagnetizing factor. Because we use a SQUID we are able to make sensitive low-field measurements which other techniques (such as magneto optical indicator films or scanning Hall probes) cannot provide.

The films were deposited using pulsed laser deposition onto a strontium titanate substrate, in a process similar to that used for depositing YBCO onto nickel based RABiTS tapes [59, 60, 61]. The films had a size of $1\text{ }\mu\text{m} \times 3\text{ mm} \times 15\text{ mm}$. This particular sample had a wire patterned into the center (*c.f.* Fig. 5.1(b)). Because of experimental probe design limitations, we could thermal cycle samples above 100 K, but could not make any measurements near the transition temperature. The measurements described here are all at 4.2 K.

5.3.2 Meissner state

We first studied the sample in the Meissner state. To verify that the sample remained in the Meissner state we zero field cooled the sample, ramped the external field from zero to a specific value and then ramped the external field back to zero. By comparing the image after zero field cooling with the image after ramping the external field up and down, we determined if any flux became trapped in the sample. If no flux became trapped in the sample the sample was assumed to be in the Meissner state up to the specified value of external field.¹¹ We found that our sample remained in the Meissner state for external fields less than 223 mOe but became hysteretic for fields greater than 448 mOe. Fig. 5.12 shows the sample in the Meissner state at 223 mOe.

¹¹It is possible, but very unlikely, that flux entered and left the sample reversibly, see the discussion on p. 95.

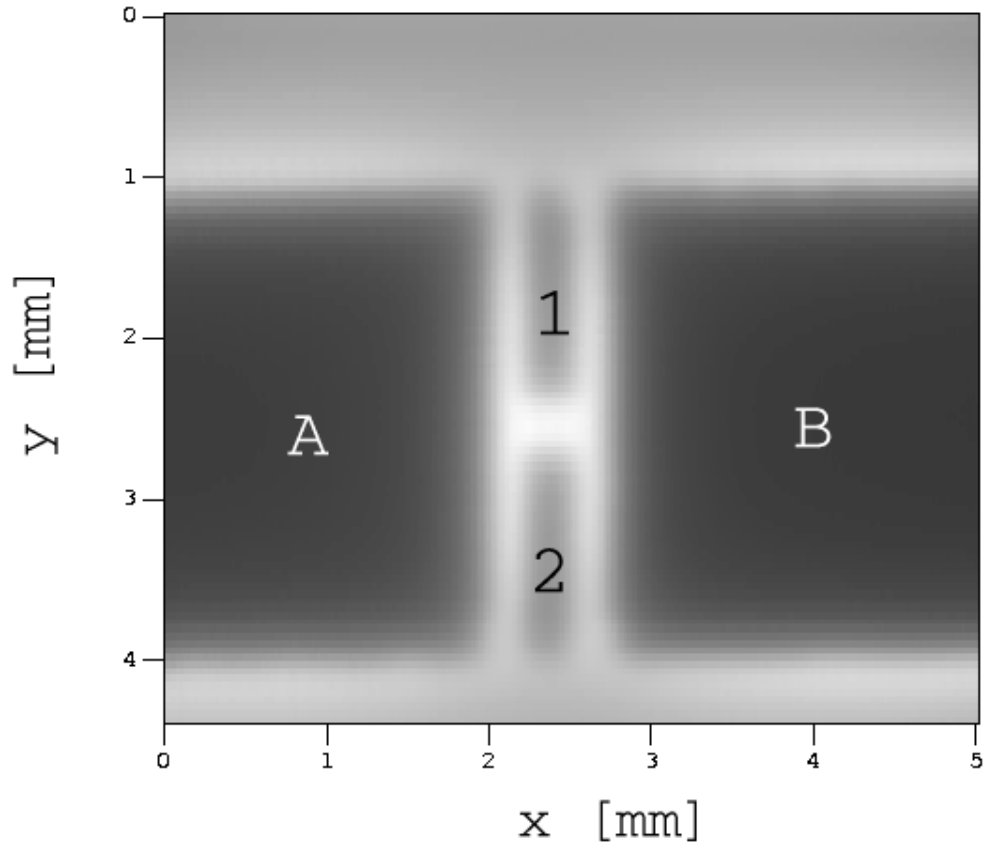


Figure 5.12: Magnetic image of the YBCO film in a 223 mOe applied field. The grey scale indicates average magnetic field in the SQUID ranging from zero (black) to 1.2 G (white). The superconductor is in the black colored regions, where it is screening flux, labeled A and B. The superconductor is 3 mm wide. In the center of the superconductor a wire (not visible) for transport measurements is patterned, leaving two sacrificial islands of YBCO, labeled 1 and 2.

Additionally, we verified that the sample contained no remanence in this case by subtracting the zero field cooled image from an image taken after increasing the external field and removing it again. Fig. 5.13 shows the results of this experiment, in which it can be clearly seen that there is no remaining flux pinned in the sample. We note there are some changes, notably the circular regions in the center. These circular regions are damaged regions where contact pads were pushed into the sample for testing of transport parameters, and should not be considered representative of the typical sample properties. The grey scale in Fig. 5.13 goes from -1.3 mG to 1.3 mG which corresponds to the flux sensitivity resolution level in our experiment of ± 1.3 mG for measurements (such as the remanence measurements presented here) which require the addition or subtraction of two images. Contributions to the noise level include flux noise in the SQUID, and displacement errors in the scanning process.

The flux difference measured in Fig. 5.13 is three orders of magnitude smaller than the flux difference measured in Fig. 5.15 or Fig. 5.12. The latter two flux difference levels are representative of the flux difference levels measured throughout the course of this experiment, *i.e.* the in-field Meissner state discussion to follow.

We have additionally made a line cut through the image shown in Fig. 5.12 at $y = 3.5$ mm. The data points for this line cut are shown in Fig. 5.14. The current distribution which generates this magnetic field profile can be inferred by comparing with the data. Because our sample is so long compared to the width (15 mm *vs.* 3 mm) we treat it as an infinitely long superconductor of width $2W = 3$ mm and thickness $d = 1$ μ m. Additionally, we define the thin film penetration depth $\lambda_{\perp} = 2\lambda^2/d$ where λ is the London penetration depth and λ_{\perp}

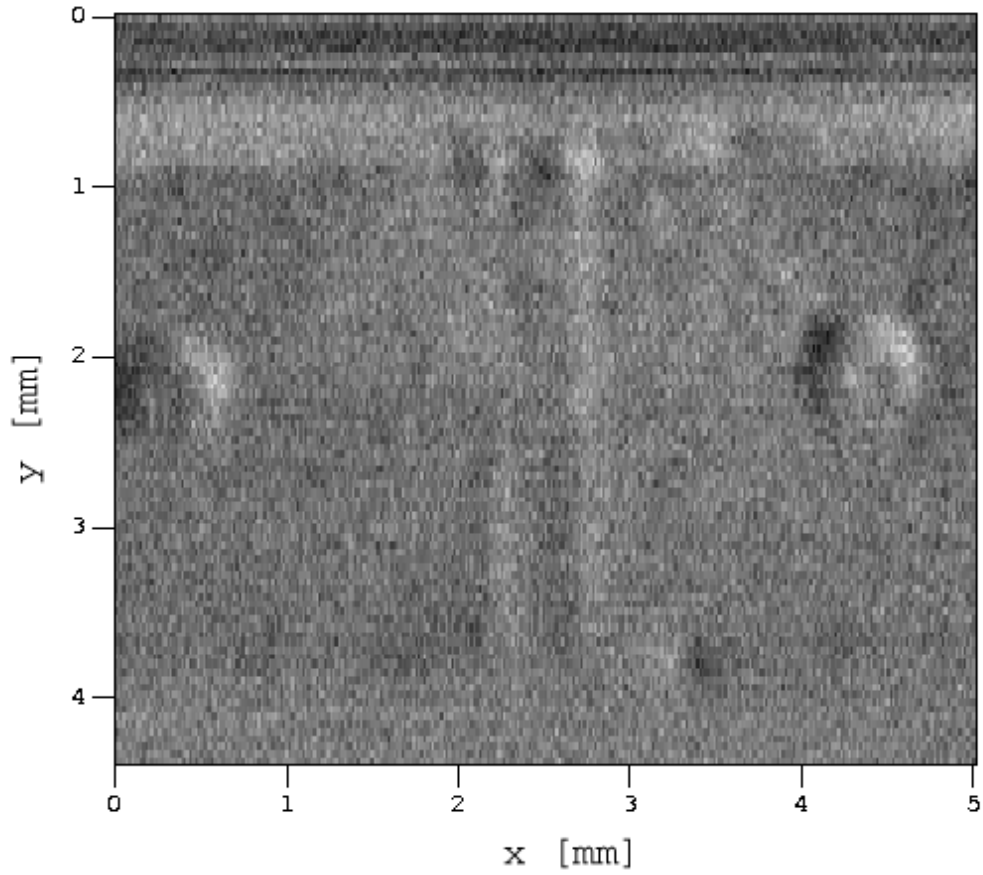


Figure 5.13: Remanence image of the YBCO film after cooling in zero field and then ramping the external field to 223. mOe. The grey scale runs from -1.3 mG (black) to 1.3 mG (white).

is the thin film penetration depth, as discussed in Pearl [85, 86].

Starting from the London equation and Ampere's law, we can derive an integrodifferential equation describing the current distribution in a thin film. This derivation is non-trivial, but a careful analysis has been carried out by Dorsey [63]. This integrodifferential equation is

$$\frac{\lambda_{\perp}}{2} \frac{\partial I(x)}{\partial x} = \frac{1}{2\pi} \int_{-W}^W \frac{I(x') dx'}{x' - x} - H_{\text{ext}} \quad (5.6)$$

in which $I(x) = \int J(x, z) dz$, the two-dimensional current density.

There is a well known solution to (5.6) due to Larkin and Ovchinnikov [62] for the current distribution interior to the sample. If $\lambda_{\perp} \ll W$ we neglect the left hand side of (5.6) and solve to get

$$I(x) = -\frac{2H_{\text{ext}}x}{\sqrt{W^2 - x^2}}, \quad (5.7)$$

with x as the coordinate along the width of the film. This diverges at the sample edge, so cannot be valid everywhere. (5.7) does not contain any dependence upon the penetration depth since we neglected that term in (5.6) to form the solution.

Larkin and Ovchinnikov also found a form for the current distribution at the sample edge, valid only in the edge region, but did not discuss the cross over region.¹²

Instead, we chose to look at the Vodolazov and Maksimov[68] results: an asymptotic form for the current distribution in the sample, for the case of a thin film $d < \lambda$ and a thick film $\lambda < d < W$, valid over the entire cross section of the sample. They find that the results in both the thin and thick cases closely

¹²There is an error in the Larkin and Ovchinnikov edge formulation, noted by Dorsey [63]. In both cases, the maximum value of the current (*c.f.* Eqn. 5.8), at the edge, is however, given correctly, and agrees with the asymptotic results given by Vodolazov and Maksimov[68].

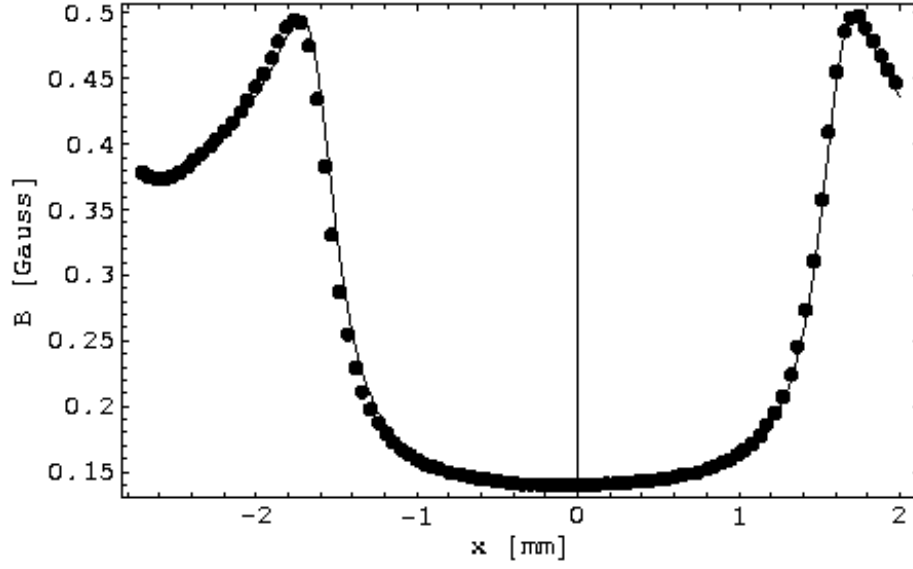


Figure 5.14: Comparison of line cut (black dots) in Fig. 5.12 with the magnetic field predictions for $-2 \text{ mm} < x < 2 \text{ mm}$ of Vodolazov *et al.* (solid line). We used the following parameters to generate the specific curve, with the caveats noted in the text: $\lambda = 150 \text{ nm}$, $H_{\text{ext}} = 200 \text{ mOe}$, a SQUID height of $175 \mu\text{m}$ and the sample's geometric parameters.

agree, except near the edge region $|x| < W - d$, and that both solutions agree for the maximum value at $|x| = W$. They predict this edge value, which is the maximum value of the current distribution,

$$\frac{I(W)}{H_{\text{ext}}} = \sqrt{2\pi \frac{W}{\lambda_{\perp}}}. \quad (5.8)$$

We compared our measured magnetic field profile with the profile predicted by Vodolazov and Maksimov

$$I(x) = H_{\text{ext}} \frac{x}{\sqrt{\alpha(W^2 - x^2) + \beta}}, \quad (5.9)$$

with $\alpha = \frac{1}{4} - \frac{0.63}{(W/\lambda_{\perp})^{0.5}} + \frac{1.2}{(W/\lambda_{\perp})^{0.8}}$ and $\beta = \frac{2\lambda_{\perp}}{\pi W} + 4(\frac{\lambda_{\perp}}{W})^2$. With this model we found the best comparison to occur for a SQUID height of $175 \mu\text{m}$ and an external field of 200 mOe . These values compare favorably to the experimental parameters: an estimated SQUID height of $100 \mu\text{m}$ and an external field of 223 mOe . Additionally we find that we can compare the data with any value of λ of about $1 \mu\text{m}$ or less; this occurs because our resolution is limited by the height of the SQUID over the sample. Consequently, we cannot extract a value for λ from our data. However, there is quite good agreement between the data and the model using our parameters, as shown in Fig. 5.14.

5.3.3 Demagnetization factor

We computed the demagnetization factor for the sample we used by comparing the value of the applied external field compared to the measured magnetic field near the edge of the sample, using

$$\eta = 1 - \frac{H_{\text{ext}}}{H_{\text{edge}}} \quad (5.10)$$

in which H_{ext} is the applied external field and H_{edge} is the magnetic field as measured at the edge of the sample. We take the model parameters, generated above, and use them, by setting the SQUID height to zero, to compute the magnetic field at the edge of the sample, $H_{\text{edge}} = 5770$ mOe. This value of H_{edge} yields a demagnetization factor of $\eta = 0.961$.

Once we know the demagnetization factor we can provide an estimate of H_{c1} , the first critical field of the sample. When H_{edge} exceeds H_{c1} , flux begins to penetrate the sample in the form of vortices. Because of observed flux pinning in the sample, flux does not penetrate further into the sample, and also remains pinned even when the external field is removed. From the observation of first flux penetration we obtain a measurement of H_{c1} . We used our values for the demagnetization factor at the surface of the sample to estimate H_{c1} for this film to be between 5.77 Oe (for which the sample remains in the Meissner state) and 11.48 Oe (for which we first notice flux penetration). We can compare this range to what one would expect for bulk samples. From Tinkham¹³ the first critical field is defined as the external magnetic field at which the free energy becomes metastable with respect to the formation of the first vortex. The value of this critical field in the bulk is

$$H_{c1} = \frac{1}{4\pi} \frac{\Phi_0}{\lambda^2} \ln \kappa, \quad (5.11)$$

in which $\kappa = \lambda/\xi$ the ratio of the London penetration depth to the superconducting coherence length. Using $\lambda = 2000$ Å and $\xi = 1$ nm we find a bulk value of $H_{c1} = 220$ G.

By contrast, Kuznetsov[69] provides a form for H_{c1} in the case of a thin film

¹³Tinkham [4], p. 149.

($d < \lambda$),

$$H_{c1f} \approx \frac{\Phi_0}{16(2 \ln 2 + 1)\lambda_{\perp}W} \left(\ln \frac{\lambda_{\perp}}{r_c} + 0.81 \right), \quad (5.12)$$

in which r_c is the radius of the vortex core and is taken to be $r_c \approx \xi$. (5.12) already accounts for the demagnetizing factor, so the Kuznetsov formula gives a value of $H_{c1} = 250$ mG, which is considerably smaller than the bulk value, but is in excellent agreement with our applied field of 223 mOe.

The inferred value of H_{c1} from the flux penetration measurements, in the case of the bulk value, is too small. However, in the thin film case the value of H_{c1} agrees quite nicely between our experiment and Kuznetsov *et al.*[69] This indicates that our sample can be well described by the thin film limit ($d < \lambda$) despite the fact that our sample is actually slightly *thicker* ($d = 1 \mu\text{m}$) than the penetration depth ($\lambda \approx 2000 \text{ \AA}$).

5.3.4 Remanence in YBCO films

In addition to the Meissner state, we looked at the critical state, for external fields up to 57.4 Oe. Fig. 5.15 shows the remanence after zero field cooling the sample, applying a 57.4 Oe external field to it, and then removing the sample. The flux became trapped near the edges of the sample. This picture differs quite dramatically from that of the geometrical barrier [2] and even from the description of vortex penetration given by Vodolazov and Maksimov for thick films [68], in which remnant flux becomes trapped in the *center* of the sample.

Kuznetsov *et al.* [69] give a different picture of flux penetration and the critical state flux distribution in which flux penetrates the sample and, because of strong pinning sites, becomes pinned at the edge region and does not penetrate into the center of the sample. In fact the Kuznetsov *et al.* picture looks remarkably

similar to the flux distribution seen in our experiment.

Kuznetsov *et al.* give specific analytic predictions for the current distribution in the critical state. However, the size of the critical region relates to the magnitude of the external field. We cannot generate a large enough magnetic field in the scanning SQUID microscope to create a large enough critical region to analyze. This occurs because our resolution is limited by the SQUID-sample separation and we cannot resolve features of the size needed to quantitatively compare with the Kuznetsov *et al.* model.

We can observe that the size of the critical region grows as the externally applied field is increased. Fig. 5.16 shows the magnetic field profile for the sample as the external field increases from 0 Oe to 44.9 Oe to 57.4 Oe.

To conclude, we have imaged both the Meissner state and the critical state in a YBCO film of large demagnetizing factor. From these image measurements, we have provided a direct estimate for H_{c1f} in YBCO and for the demagnetizing factor for our sample. What's more, we have been able to observe the onset of flux penetration into the sample and to characterize the flux distribution of the critical state, finding that flux penetrates the edge of the sample and immediately becomes strongly pinned to the edge region of the sample, in stark contrast to the geometrical barrier picture. This edge pinning is due to the strong pinning potential of our sample, which is quite different from the weak pinning of samples such as that measured by Zeldov *et al.* [2] The geometrical barrier is not important in our sample, or in other sample with large pinning potentials, especially highly granular thin film materials. In fact, pinning at the edge may be stronger due to enhanced material defects at the sample edge.

The value of H_{c1f} that we report here is different from the value of H_{c1} typ-

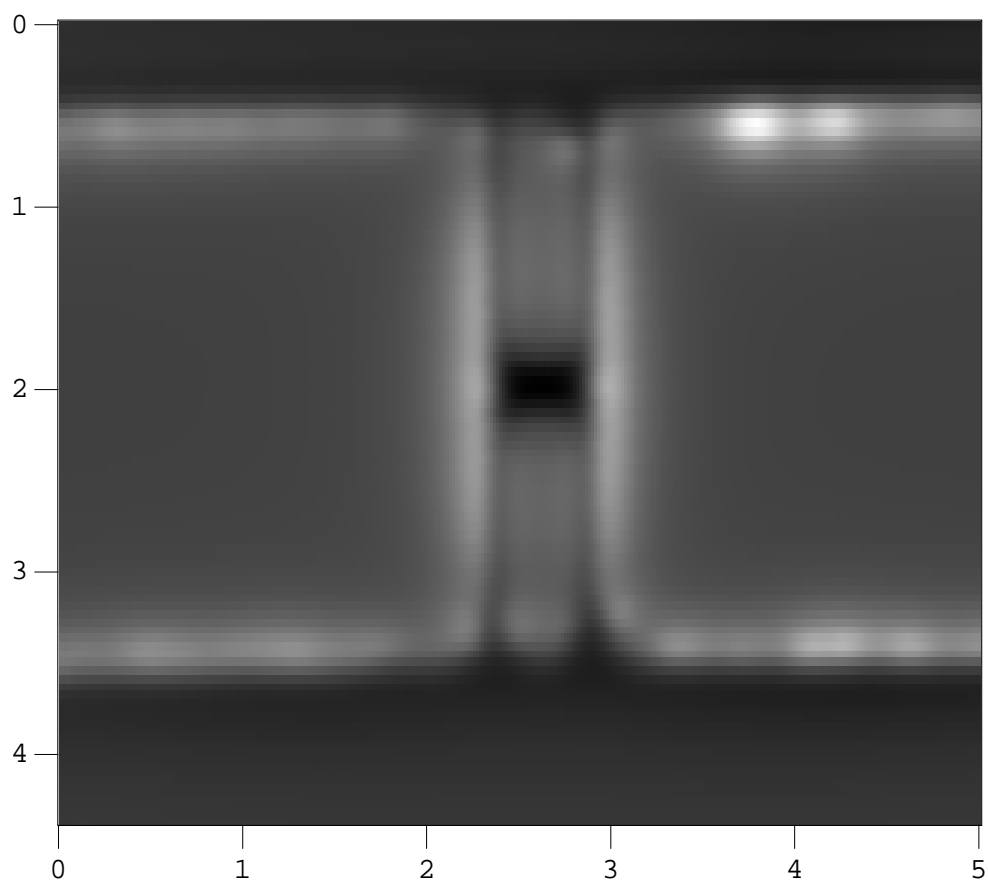


Figure 5.15: Remanence images of the YBCO film after cooling in zero field and then ramping the external field to 57.4 Oe and back to zero. The grey scale runs from -1.3 G (black) to 2.15 G (white).

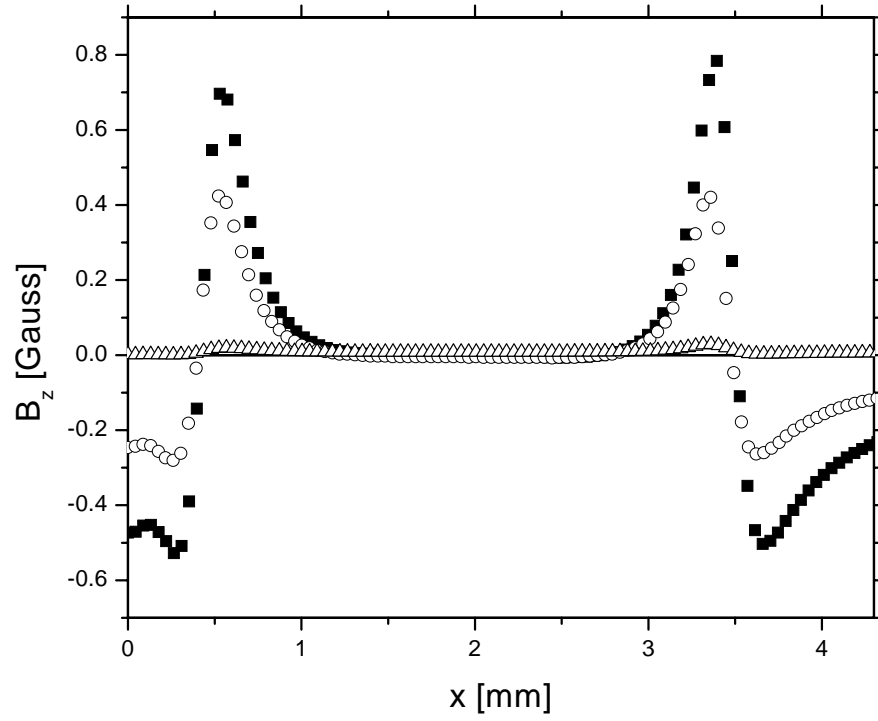


Figure 5.16: Magnetic field profiles on the remanence critical state in the YBCO/STO film. for $H_{\text{ext}} = 57.0$ Oe (black squares) 44.9 Oe (open circles) and 11.2 Oe (open triangles)

ically reported in the bulk material [87]. However, this value is about an order of magnitude larger than that predicted by Kuznetsov *et al.* for a thin film. The difference between the Kuznetsov *et al.* and bulk values arises due to the non-local nature of electrodynamics in thin films. The Pearl formulation of thin film electrodynamics [86, 85] (used by Kuznetsov *et al.*) requires that the thickness of the film be much less than the penetration depth (*i.e.* $d \ll \lambda$). For the sample in our experiment, we do not fall into this thin film regime ($d = 1\,\mu\text{m}$ and $\lambda \approx 1500\,\text{\AA}$). Our value for H_{clf} falls below the range of reported bulk values for H_{c1} [87], indicating that our sample falls into some intermediate regime between the thin film and bulk limits. Many practical devices are made with films of superconductor and may fall into this regime, so this intermediate regime may be of important practical consideration in terms of understanding the film response.

Chapter 6

Prospective

6.1 Introduction

We made many interesting observations which were not pursued in detail with the scanning SQUID microscope. Many of these observations may prove to be interesting sources of study in the future and are discussed here in that light.

6.2 Vortex avalanches

Before studying PME in unshunted Josephson-junction arrays we placed a large array into the scanning SQUID microscope in order to test out the SSM and see how well it functioned. We did many different experiments to test the microscope and fix any discovered problems. One of these experiments included zero field cooling the array and then increasing the external field in steps, imaging the array at each step.

6.2.1 Avalanche phenomenology

Below a particular field, the array remained in the Meissner state and screened all the external flux from the interior. Upon exceeding this particular field, the flux would penetrate the array in the form of “fingers” which avalanched in toward the center of the array, perpendicular to the array edges.

The zero field cooled array measured in zero field is shown in Fig. 6.1. Subsequent images taken after increases of the external field are shown in Fig. 6.2 in which the external field is ramped to $2.4 \Phi_0$ per unit cell (one avalanche has occurred, near the lower right edge) and Fig. 6.3 in which the external field is ramped to $4.8 \Phi_0$ per unit cell and many avalanches have occurred. Generally, these avalanches were quite reproducible. However, we note that there are distinctions between Fig. 6.1 through Fig. 6.3 and Fig. 6.4 through Fig. 6.6, notably in the finger at the lower right.

In order to verify that these avalanches really occurred as avalanches, not the aggregation of many small changes (not visible in our coarse grained steps), we took fine grained steps in the external field. At each step we imaged the array to observe the location of flux in the array. A series of these images are shown in Fig. 6.4 through Fig. 6.6, in which the first image Fig. 6.4 shows the array immediately after an avalanche at $\Phi_{\text{ext}} = 2.52 \Phi_0$ per unit cell. The second image Fig. 6.5 shows the array after the external field was increased to $2.64 \Phi_0$ in which no large avalanche has occurred, but there have been small redistributions of flux, particularly at the end of the fingers. The numbers in the figure indicate the regions where this redistribution takes place. Fig. 6.6 shows the next avalanche into the array in an image taken at $2.76 \Phi_0$ per unit cell.

Fig. 6.5 immediately follows Fig. 6.2 but there are important distinctions

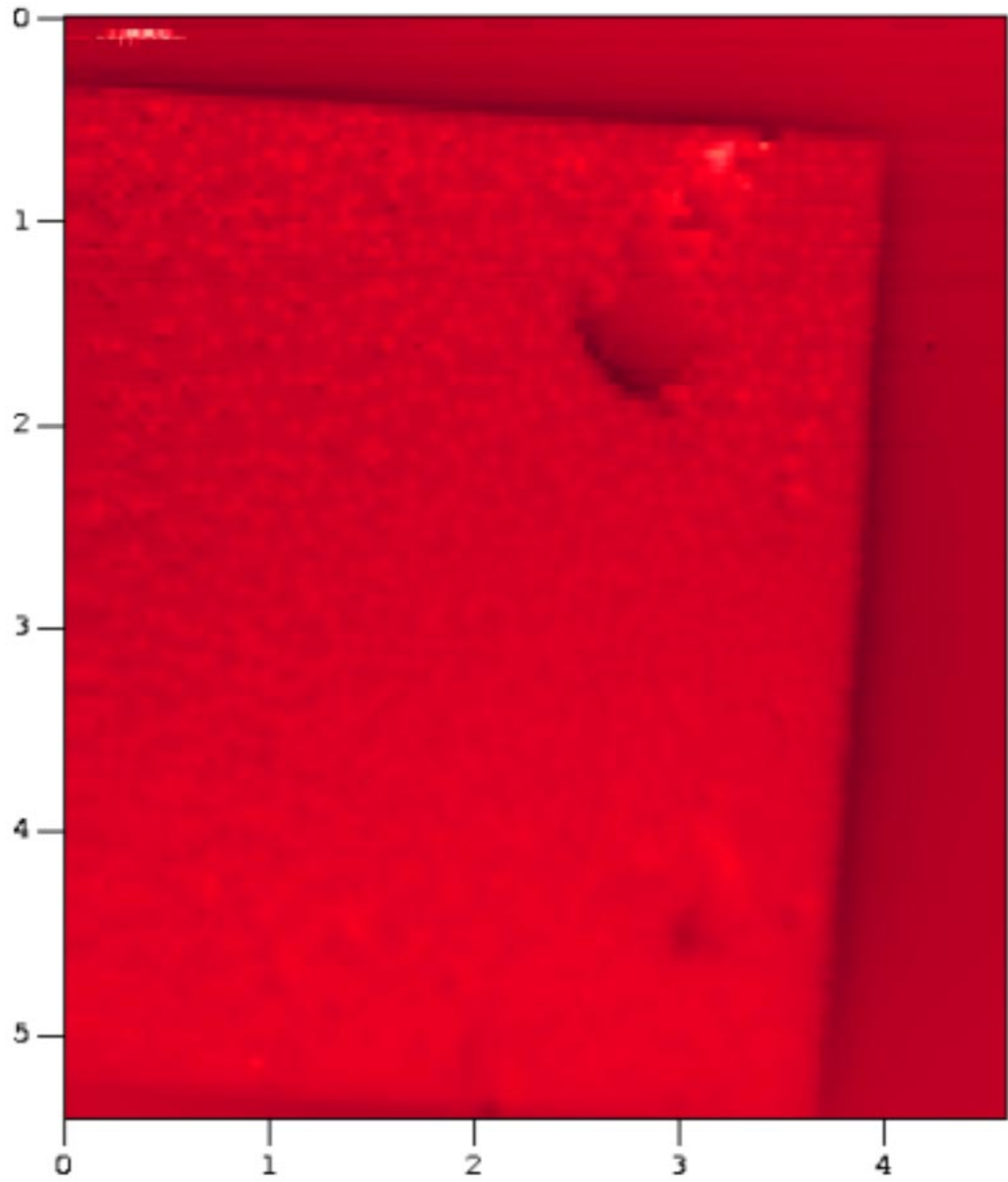


Figure 6.1: Successive vortex avalanches into 100×150 Josephson-junction array after initial zero field cooling. The color scale has a range of 0.09 G and the length scales are shown in millimeters. The array is shown as zero field cooled, in zero external field.

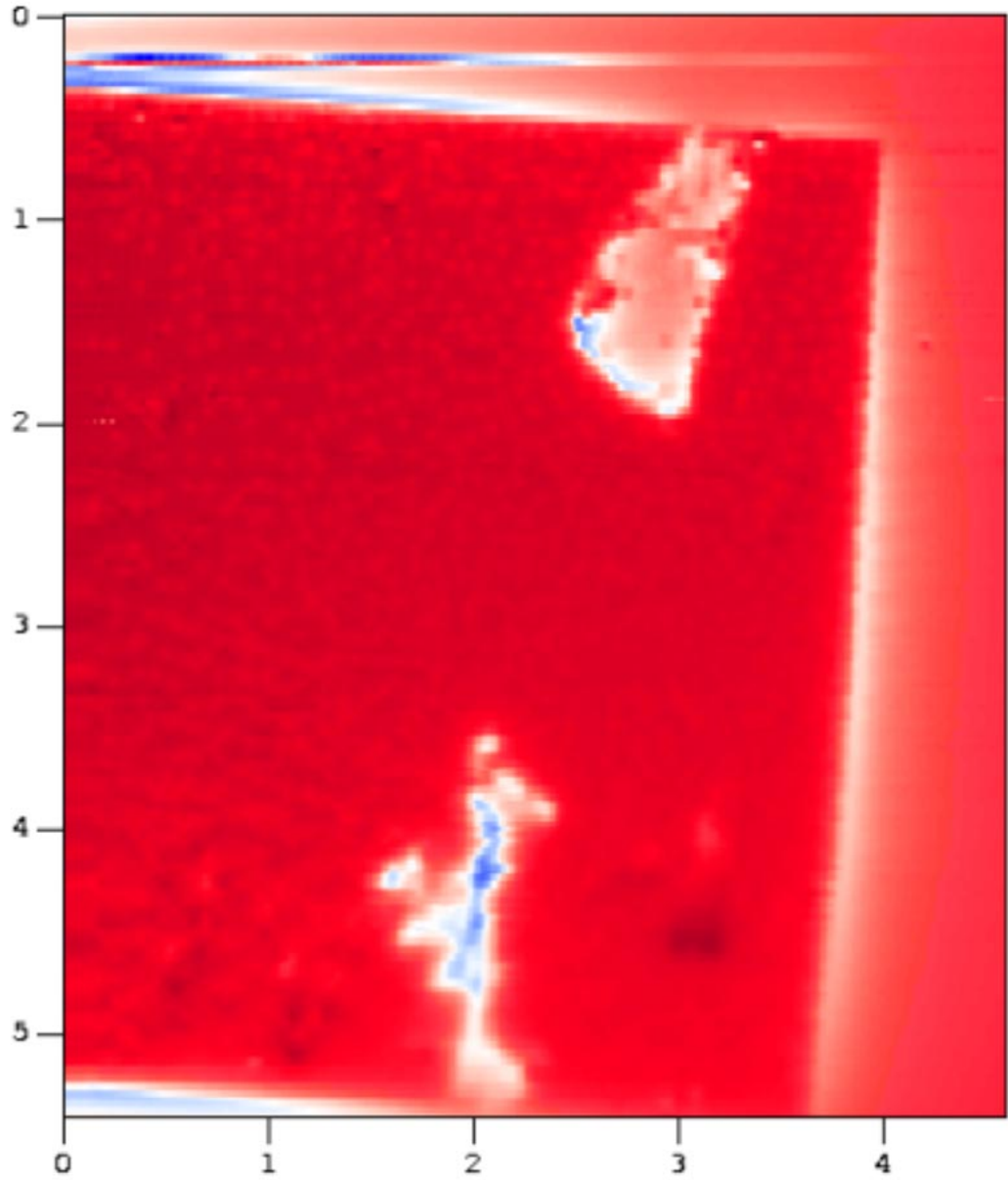


Figure 6.2: Successive vortex avalanches into 100×150 Josephson-junction array after initial zero field cooling. The color scale has a range of 0.09 G and the length scales are shown in millimeters. The external field has been ramped to $4.8 \Phi_0$ per unit cell.

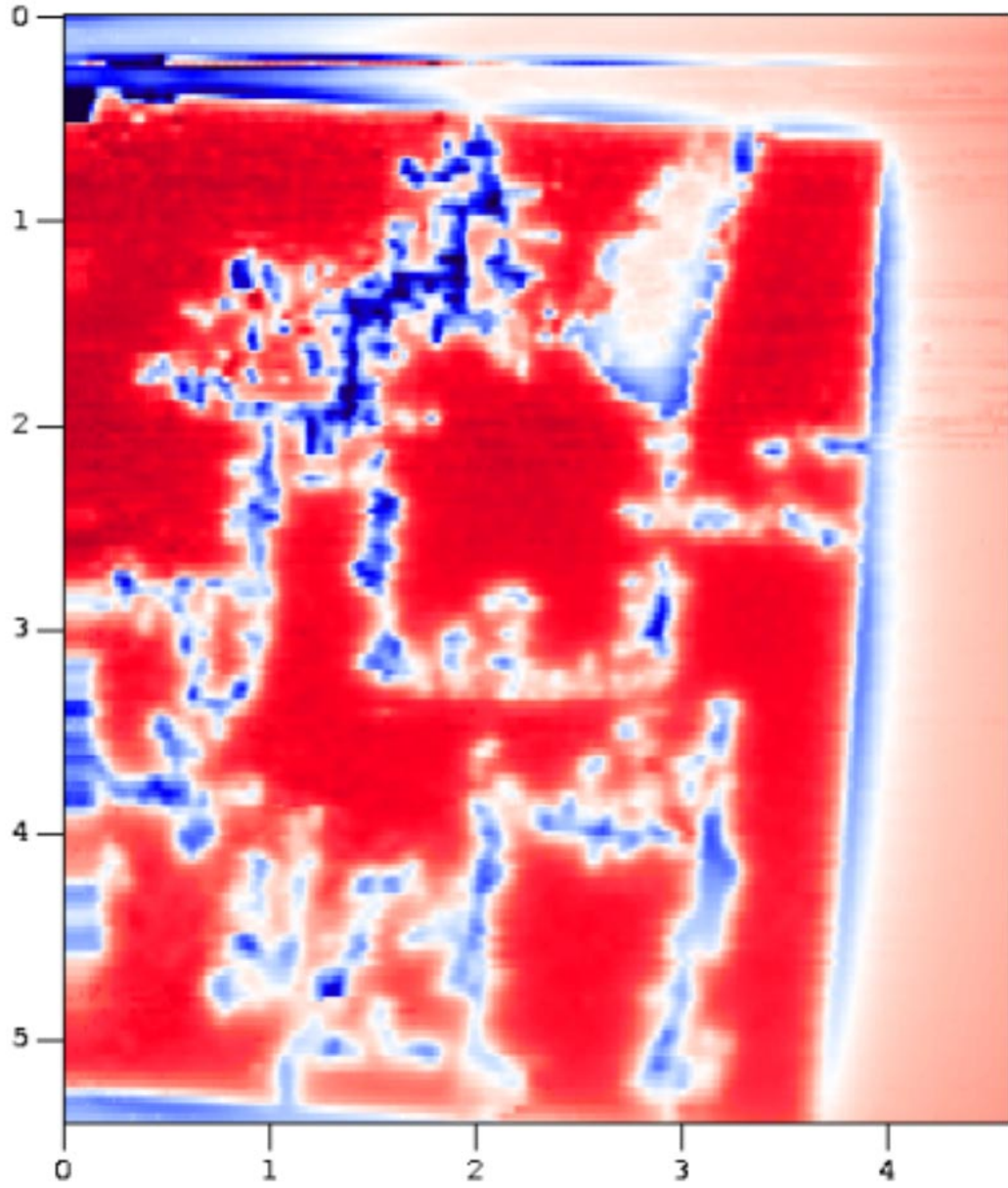


Figure 6.3: Successive vortex avalanches into 100×150 Josephson-junction array after initial zero field cooling. The color scale has a range of 0.09 G and the length scales are shown in millimeters. The external field has been ramped to $2.4 \Phi_0$ per unit cell.

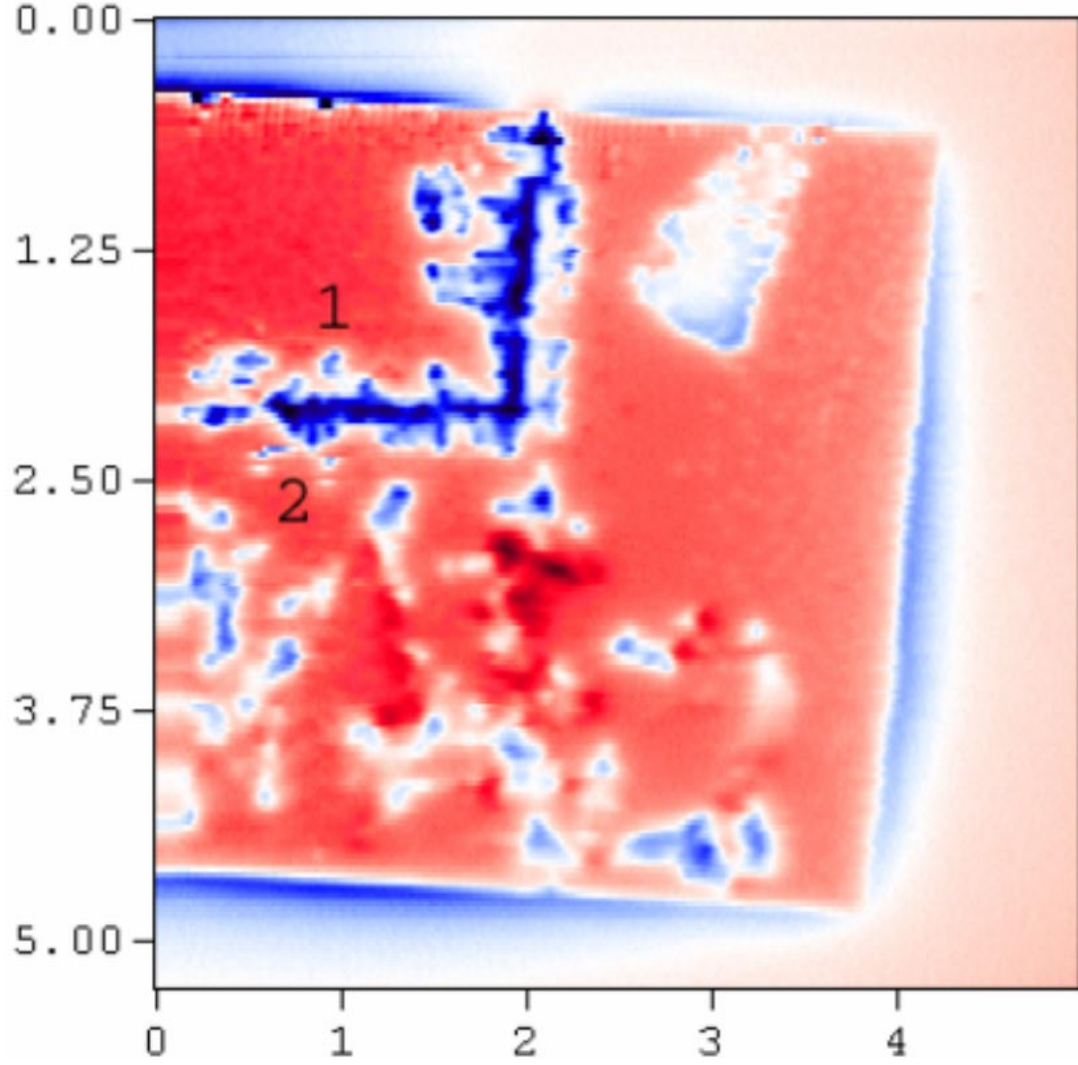


Figure 6.4: Magnetic field image taken between vortex avalanches. The array was zero field cooled, then the external field increased to $\Phi_{\text{ext}} = 2.52 \Phi_0$ per unit cell of the array. The color scale has a range of 0.09 G and the length scale along the edges is shown in millimeters.

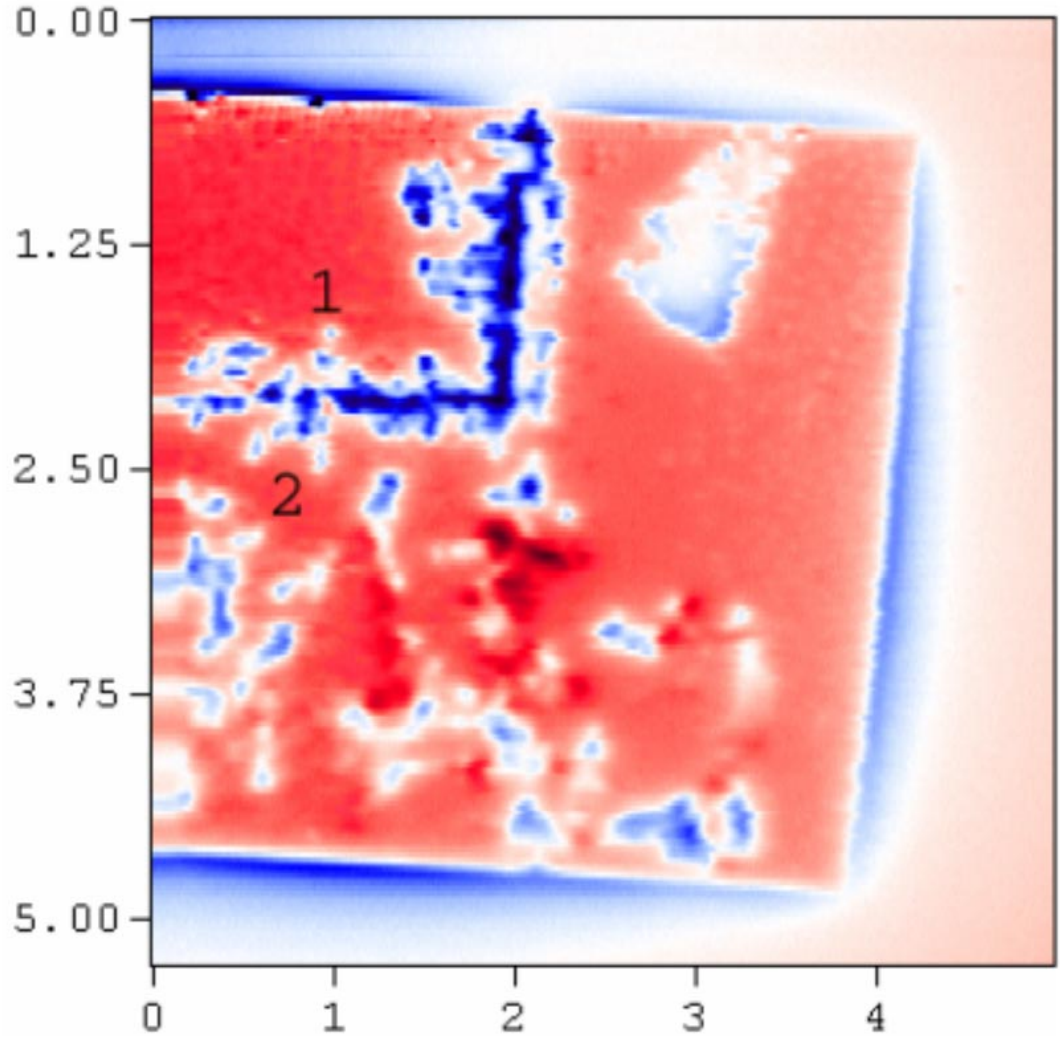


Figure 6.5: Magnetic field image taken between vortex avalanches. The array was zero field cooled, then the external field increased to $\Phi_{\text{ext}} = 2.64 \Phi_0$ per unit cell of the array. The color scale has a range of 0.09 G and the length scale along the edges is shown in millimeters.

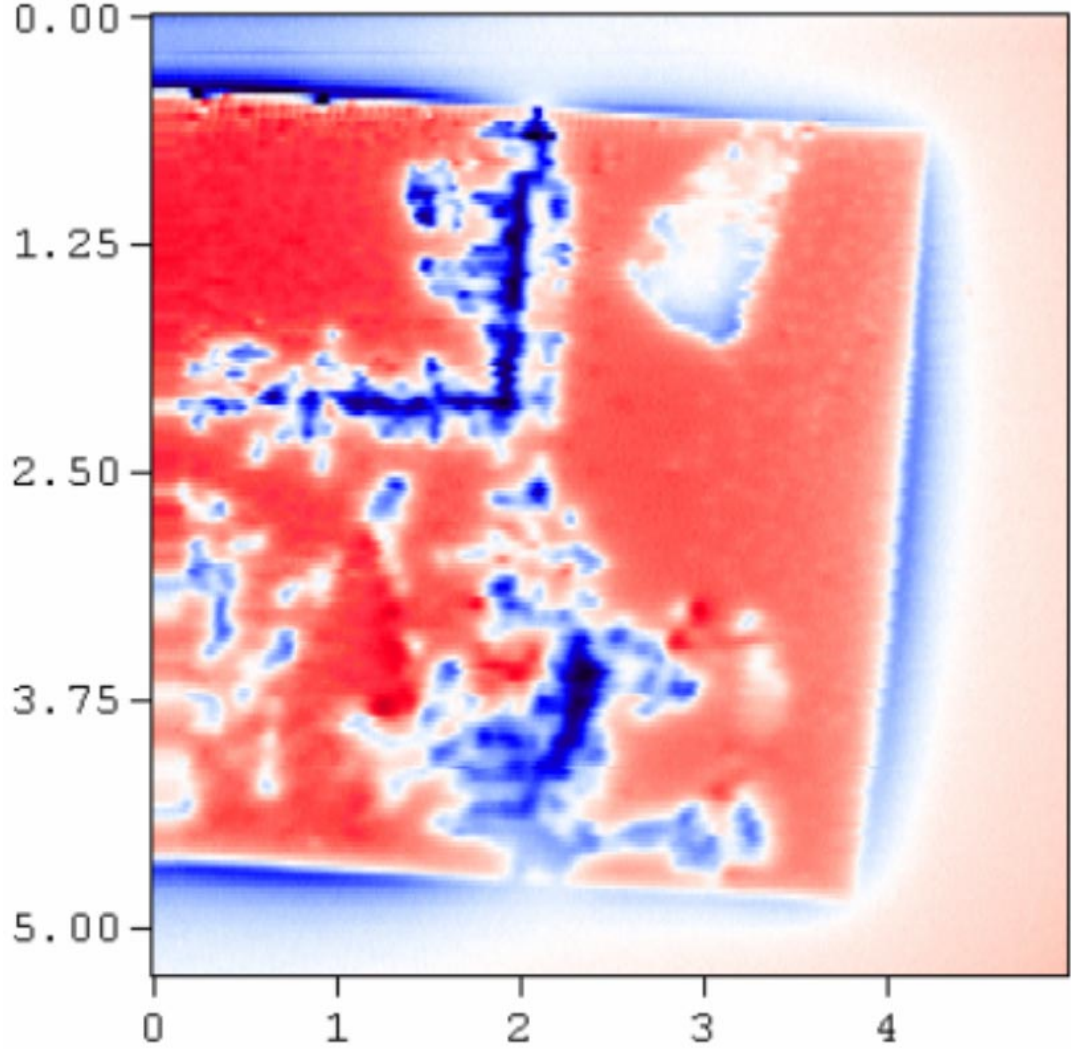


Figure 6.6: Magnetic field image taken between vortex avalanches. The array was zero field cooled, then the external field increased to $\Phi_{\text{ext}} = 2.76 \Phi_0$ per unit cell of the array. The color scale has a range of 0.09 G and the length scale along the edges is shown in millimeters.

between the two images. We notice that Fig. 6.4 is much more complicated than Fig. 6.2 in which only one small avalanche has occurred. We can understand this because we have increased the external field in Fig. 6.4 to $\Phi_{\text{ext}} = 2.52 \Phi_0$ per unit cell versus the external field in Fig. 6.2 of $\Phi_{\text{ext}} = 2.4 \Phi_0$ per unit cell, so we expect further flux processes to have occurred.

6.2.2 Potential avalanche explanations and further experiments

Shunted Josephson-junction arrays

Fernando Araujo-Moreira worked with Paola Barbara looking at AC susceptibility in shunted and unshunted Josephson-junction arrays.¹ They noticed that there were distinct differences in the AC susceptibility between the two cases. In fact, we expect these differences just by comparing the equations which describe the array in both cases. The unshunted array we have already described (see (2.4), p. 9) but in the case of the shunted array, we need to modify the equations because of the shunt resistor which provides a resistive and inductive short around the Josephson junction, R_s and L_s . Fig. 6.7 shows this relationship schematically (*c.f.* Fig. 2.2). The RCSJ model equation becomes modified,

$$I = I_c \sin(\gamma) + \frac{1}{R} \frac{\Phi_0}{2\pi} \frac{d\gamma}{dt} + C \frac{\Phi_0}{2\pi} \frac{d^2\gamma}{dt^2} + I_s, \quad (6.1)$$

in which I_s is the current through the shunt resistor. To fully define all of the variables, we now need a further equation which equates the voltage drops across the junction channel and the shunt channel

$$\frac{\Phi_0}{2\pi} \frac{d\gamma}{dt} = +L_s \frac{dI_s}{dt} + I_s R_s \quad (6.2)$$

¹Refs. [11] and [12] summarize these results.

in which L is the inductance due to the shunt resistor and R_s is the resistance of the shunt resistor. However, if we assume that the inductance is small, we can ignore the induction term in (6.2) and the additional resistive term adds damping to (6.1). For proper values of the shunt resistor, this system becomes *over-damped*.² If we do not neglect the inductance of the shunt resistor, the dynamics become significantly more complicated, and are discussed in detail in Ref. [88].

Once vortices penetrate the shunted array, we may imagine that instead of starting a complicated dynamic process by which they move deep into the array (the fingers) their motion is damped, and penetration takes place in a more uniform manner. Because of these differences between the shunted and unshunted arrays, we might expect the avalanche behavior to occur only in the unshunted array, *i.e.* the dynamics causing the avalanches to occur would die out in the shunts. This experiment has not been attempted, though samples exist with similar parameters to the unshunted arrays.

Self organized criticality

The flux avalanches into the array look remarkably similar to models of self-organized criticality (SOC) [89]. Several authors have used the SOC model to theoretically describe the critical state in superconductors [90, 91], and there have been some measurements of SOC in bulk superconductors [92]. A well developed model is that of Ginzburg [90] which says that under a constant drive (*i.e.* linearly increasing external field) that the flux should enter into the array as a form of

²The distinctions between under-damped and over-damped junctions are discussed in detail in Tinkham [4] and Newrock *et al.* [7].

avalanches. Quantitatively, it describes the distribution in physical size of the avalanches, and the distribution in time between avalanches. SOC says that both of these distributions must be a power law over many orders of magnitude.

In order to verify these power law distributions experimentally, there are some significant challenges which must be overcome. To measure the size of the vortex avalanches over a large scale of avalanche size, we would need to analyze images of about 1000 avalanches or so, which means making SSM images of 1000 avalanches. For the array size we have been looking at it takes between one half and one hour to make the scan. So, to generate the required 1000 images it would take about one month of continuous scanning. This amount of scanning is not prohibitive, but would take a considerable amount of effort and, provided that nothing goes wrong with the microscope, can be accomplished.

Another possibility to verify SOC is to consider the time distribution between the avalanches, regardless of avalanche size. This experiment is not quite as simple to do with the SQUID microscope, because it requires time resolved, over several decades, flux information over the entire array, which cannot simultaneously be collected while scanning because of the time required to scan. This experiment could be performed by putting a gradiometer around the array³ and positioning the SQUID over the secondary coil of the gradiometer to measure the changes in flux as the external flux is increased. Instead of scanning, the SQUID is positioned in one place and a time resolved flux is measured in the SQUID. A similar experiment has been performed in bulk samples by Field *et al.* [93] in which they were able to resolve avalanches larger than fifty vortices. The SQUID microscope should be able to greatly improve on this resolution.

³Samples with this design have been created, Hypres design APN2.

6.3 Vortex ratchets

Working with Profs. Steve Rugierro and Laslo Barabasi at Notre Dame University, we began to explore the vortex ratchet effect in superconductors. The ratchet effect, as it is generally known, first discussed by Feynman in his lectures [94], but has been of particular interest lately in superconductors [95] and Josephson-junction arrays [96, 97, 98, 99, 100]. Much of the work surrounding the ratchet effect has been theoretical and focused on understanding just how it is that small (on the scale of Brownian motion) objects, such as single celled organisms, produce directed motion [101, 102, 103, 104], however, there has been some particularly interesting experimental work, including the chemical fabrication of molecular scale ratchets [105] and micrometer scale AC electric potential ratchets [106, 107]. In a superconductor, we want to use the ratchet effect to move vortices around for our benefit, primarily to remove flux from a superconductor in order to reduce the losses in the superconductor when carrying current.

In order to ratchet vortices around in a superconductor, we use the model of Lee *et al.* [95] which generates the ratchet potential through the patterning of the surface. The line energy of a vortex is proportional to the length of the vortex in the superconductor [4] so we can make an asymmetric sawtooth potential provided that we can pattern the surface of the superconductor in the shape of this asymmetric sawtooth. The application of an AC current provides a Lorentz force to the vortices which moves the vortices back and forth across the ratchet potential. Since the ratchet potential is asymmetric the vortices move preferentially in one direction instead of the other.

Preliminary samples of niobium with the surface patterned in this way where

fabricated at Notre Dame.⁴ An Alpha-step[108] scan, in Fig. 6.8 and Fig. 6.9 shows what the surface features of these samples look like. There are two designs, one with a unidirectional asymmetric sawtooth, Fig. 6.9. This sample is designed to move vortices one way across the sample. In principle, we should be able to see vortices move across this sample. The second sample consists of two opposing asymmetric sawtooth ratchets, Fig. 6.8. This sample is designed to flush vortices away from the center line of the sample and out of the sample.

There are two ways to experimentally look at these samples. Naturally, we would want to look at the sample with the SSM and observe the motion of vortices out of the sample upon application of the AC current. Alternatively, we could make current-voltage curves of the samples to demonstrate that after flushing vortices out of the sample, the sample presents lower losses to a supercurrent.

These samples were placed into our SQUID microscope probe with current and voltage leads attached for I-V curve measurement. Unfortunately, the initial samples had an extremely high critical current, making it difficult to generate I-V curves, except at temperatures near the transition temperature of niobium. The problem here is that it is difficult to maintain a stable enough temperature in the SQUID probe to generate reproducible I-V curves. Additionally, we attempted to scan these samples before and after the application of the ratchet current, but were unable to observe any change within the samples.

We believe that in order to observe the ratchet effect in these samples, we need to have a much lower critical current so that we can observe the samples near 4.2 K. At this temperature, the sample will be more resistant to small temperature variations. Currently new samples are being fabricated to meet

⁴Samples have been designated RAT1, RAT2 and RAT3.

these requirements and it may soon be possible to complete this experiment.

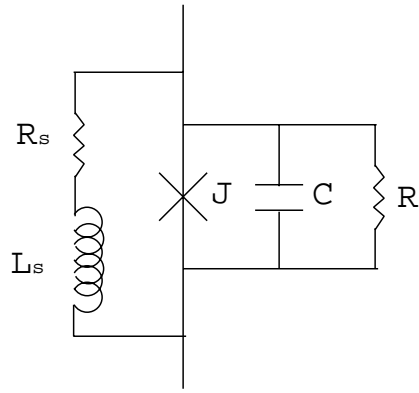


Figure 6.7: Schematic of shunted Josephson junction. R_s and L_s refer to the shunt resistance and inductance respectively. C is the capacitance of the junction, R refers to the resistive channel through the junction and J refers to the Josephson supercurrent channel.

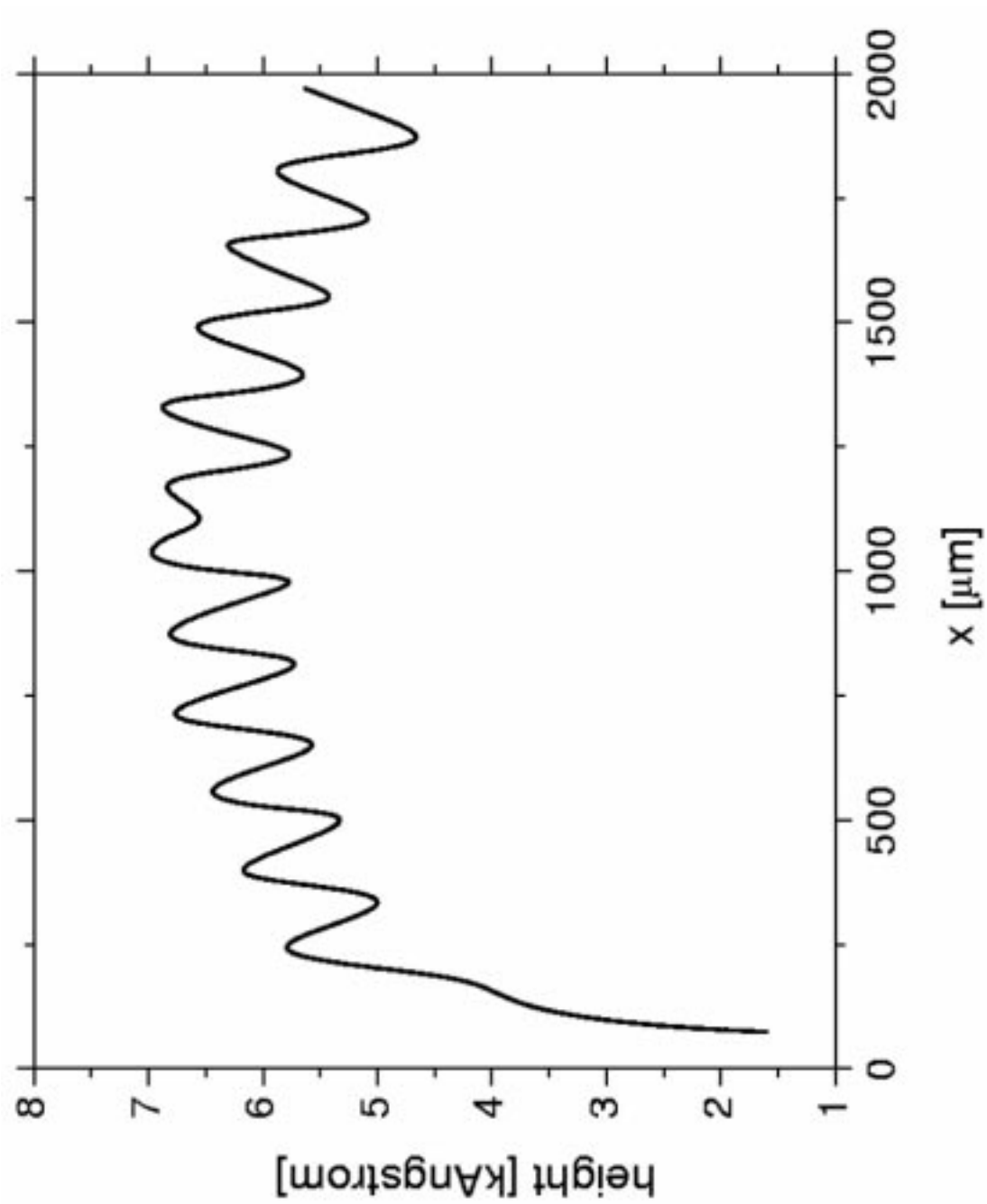


Figure 6.8: Alpha step scan for ratchet samples. Opposing asymmetric sawtooth ratchets.

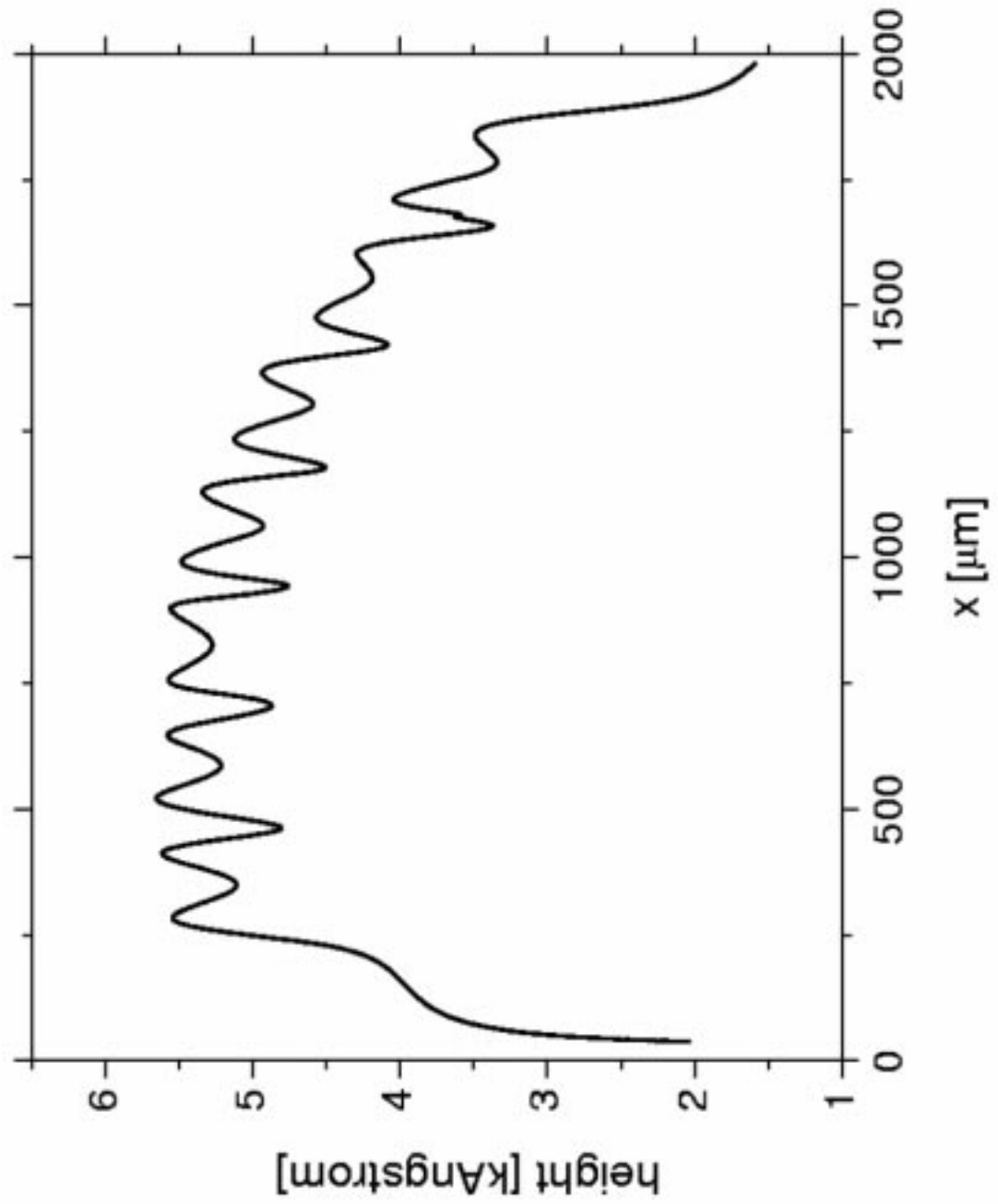


Figure 6.9: Alpha step scan for ratchet samples. Unidirectional asymmetric sawtooth ratchets.

Appendix A

Low T_c scanning SQUID microscope

A.1 Introduction

The low T_c scanning SQUID microscope (SSM) is based on a design originally by Anna Mathai, Randy Black and Fred Wellstood [84, 109] with many additional refinements provided by Fred Cawthorne and Rick Newrock of the University of Cincinnati[110]. Our description of the probe may be overly verbose here, if only to serve as a source of documentation and as an archive of which techniques have proven useful.

The probe used in these experiments was designed to primarily look at niobium Josephson-junction arrays so niobium technology was incorporated into the SQUID sensor. An important feature of the Black-Wellstood design is that it thermally isolates the SQUID and the sample from each other. This is in contrast to other designs[49] in which the SQUID tip (on a cantilever) is in direct thermal contact with the sample. We use the SSM primarily to measure quasi-DC magnetic flux, but we have made some low frequency measurements as well.¹

¹See, *e.g.*, the section on AC susceptibility in YBCO on RABiTS, 5.2.1, p. 89.

A.2 Mechanical design

The sample stage moves around in both x and y through the action of two linear pushrods, which are connected to screws at the room temperature flange of the probe. The SQUID tip remains stationary but may be moved in the z direction by means of a wedge which is also attached to a rod and screw assembly at the room temperature flange of the probe. This basic design comes from the Black-Wellstood microscope design[109, 84]. We have added copper heat sinking which extends through the cold flange directly into the liquid helium bath. There is separate heat sinking for both the SQUID and the sample. This heat sinking is shown schematically in Fig. A.1 along with the thermometry. A sketch along the length of the probe shows the general arrangement of the various parts, Fig. A.2.

A.2.1 Thermometer placement

Both the sample and SQUID are mounted on sapphire tips sitting at the end of copper cold fingers. Immediately below each of the sapphire tips sits a germanium thermometer[111] (sensitive from about 3 K to 100 K) which allows us to monitor temperature of both the sample and SQUID during operation.

A thermometer mounted in the plastic housing at the cold end provides some information about the heat produced by friction. Because the plastic has a very low thermal conductivity, the plastic will heat up during continuous scanning, absorbing heat from friction, until it becomes saturated. At saturation we can no longer control the temperature of the SQUID and sample, because the plastic temperature exceeds the SQUID operating temperature. The plastic must cool must cool before subsequent measurements may be taken.

A thermometer mounted on top of the cold flange, in the liquid helium bath, is

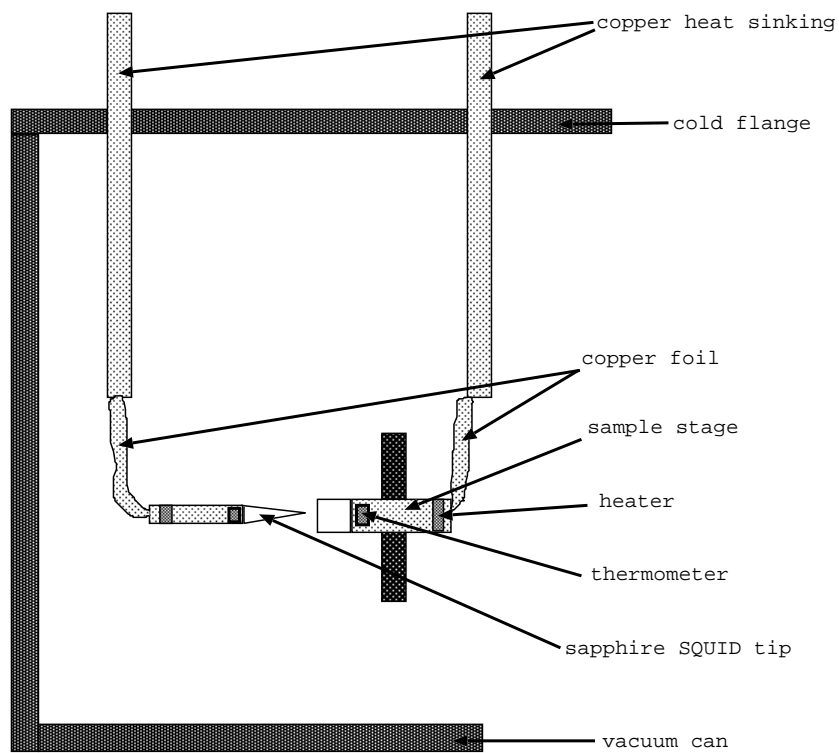


Figure A.1: Detail of cold flange heat sinking, showing cut away of vacuum can.

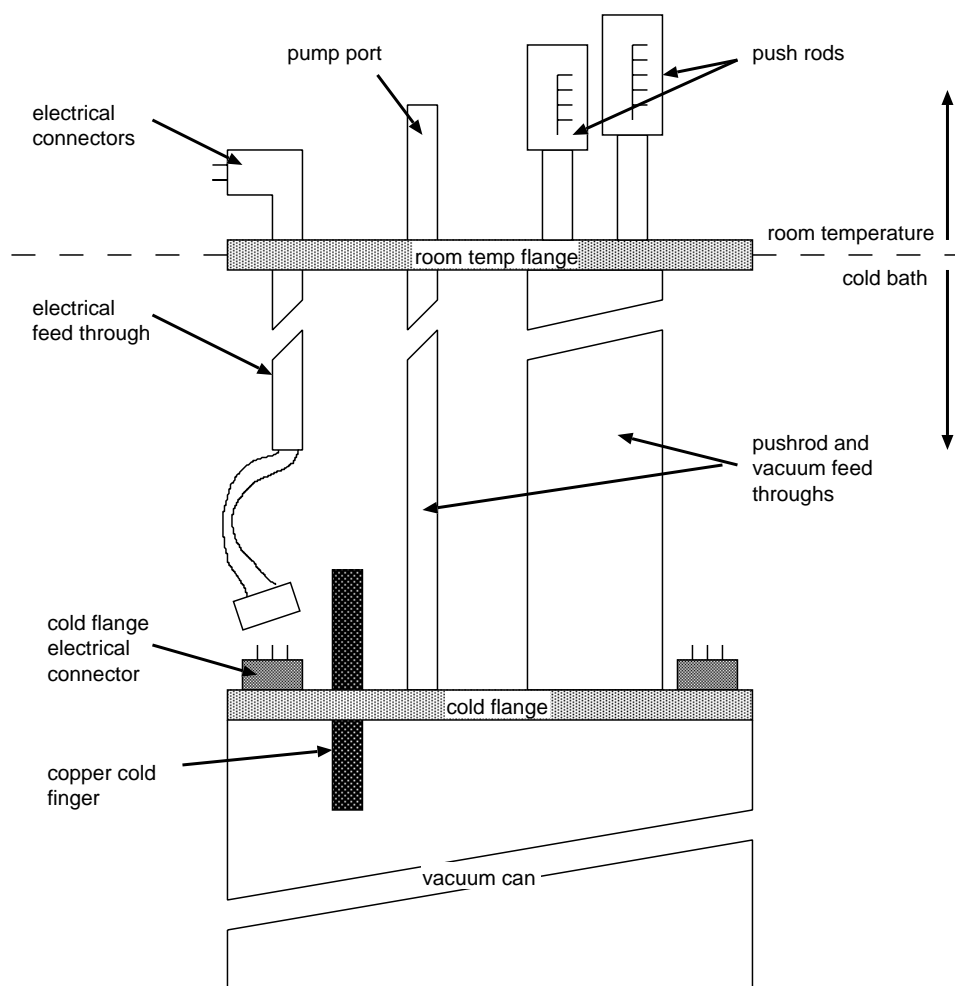


Figure A.2: Sketch of probe detailing major parts

useful for monitoring the probe temperature during initial cool down. The sample and the SQUID tips are provided with heaters wound from twisted pairs of manganin wire of about $50\ \Omega$. A separate Neocera LTC-21 temperature controller[112] is attached to each thermometer-heater pair for the sample and SQUID. With this arrangement we can separately control the sample and SQUID temperatures during operation.

A.2.2 Friction

Heat generated by friction in the scanning mechanism may raise the sample temperature by as much as a kelvin during different parts of the scanning cycle. Fig. A.3 demonstrates how the output of the SQUID electronics change as the temperature of the SQUID changes from about 4.2 K to 6.75 K. (Above 6.75 K the SQUID can no longer be kept in the flux-locked loop.) The total change in output voltage in Fig. A.3 corresponds to $0.417\ \Phi_0$ in the SQUID, which can easily swamp a real flux change if the temperature is not controlled or the shift is not corrected.

A.2.3 Vacuum quality

SQUID and sample temperature stability during scanning strongly depends upon the quality of the vacuum inside the probe. If there are no helium leaks on the cold end, any gases in the probe will be cryopumped out and the SQUID temperature during scanning may be controlled. Using two temperature controllers we can hold the SQUID and sample temperatures to within 0.01 K during scanning.

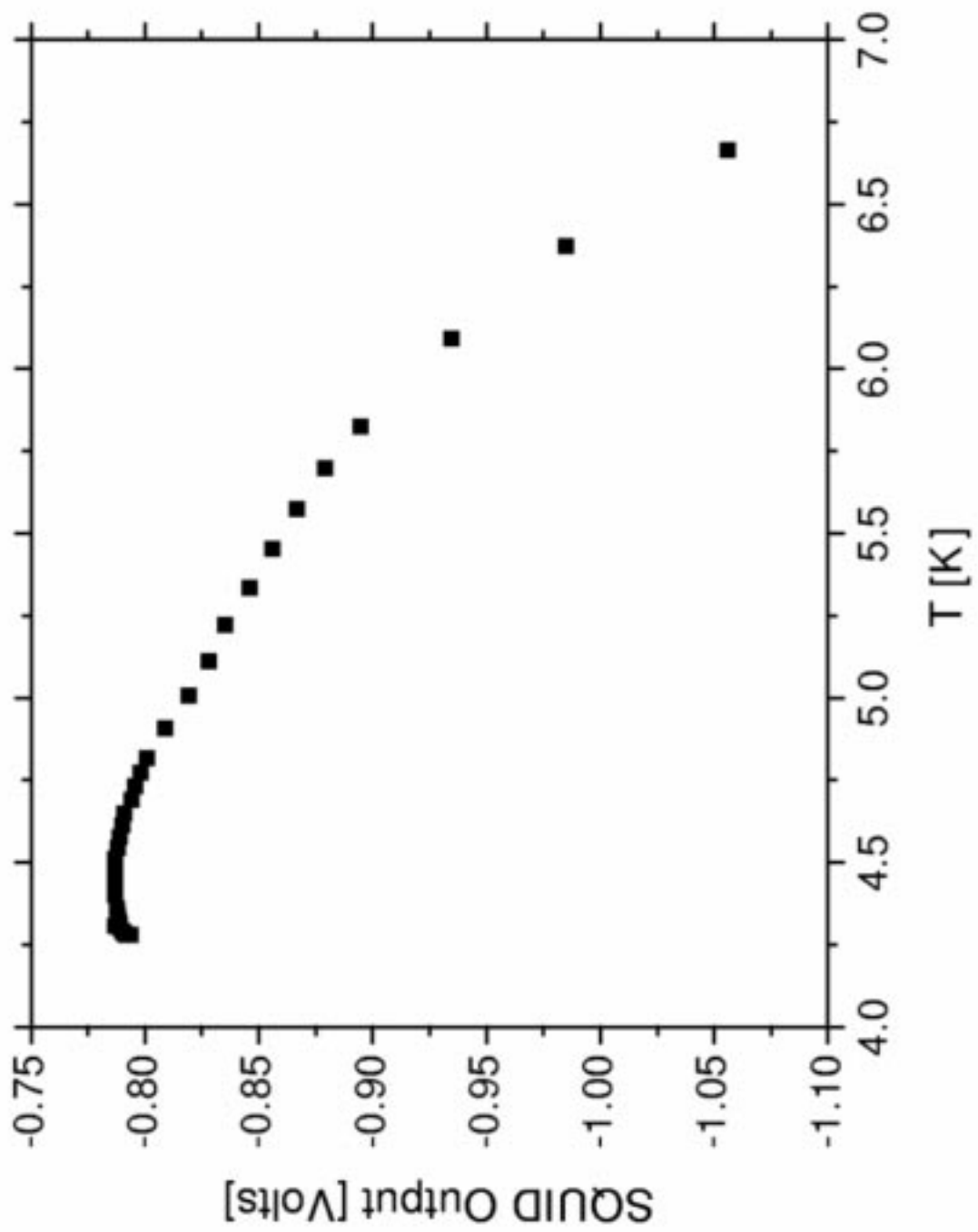


Figure A.3: SQUID electronics output *vs.* SQUID temperature

A.2.4 Scanning range

The scanning range of the mechanism is limited to approximately 20 mm in the x direction and to approximately 10 mm in the y direction. The data files output by the scanning computer index the x and y coordinates in terms of the number of steps taken by the stepper motors to move the sample. We have calibrated these stepper motor steps to real world motion at room temperature and found 10814.9 ± 5.2 steps per millimeter in the x direction, and $42933. \pm 90.$ steps per millimeter in the y direction. For the calibration we measured the actual movement of the sample stage using calipers. This movement was compared to the number of steps moved by the stepper motors. More detail on the coordinate system used for scanning is discussed in section B.3, p. 156. Additionally, data collected on samples of known geometry typically compare quite well to the known size.²

A.3 SQUID design

SQUIDs are fabricated out of Nb – Al₂O₃ – Nb Josephson junctions and made at the Hypres, Inc. foundry[113]. An optical micrograph of a SQUID is shown in Fig. A.4. We integrated the feedback coil for the SQUID flux locked loop onto the chip. The primary drawback is that there is not enough room to make a four-point measurement of the SQUID. We make a two point measurement, and use the other two contact pads for biasing the feedback coil.

A single SQUID after dicing is about 1 mm square and an optical image of one SQUID for the tip is shown in Fig. A.4(a). Nine of these SQUIDs are included in

²For a comparison, see the Meissner state current density profile fit in section 5.3.2, p. 106.

Hypres design APNSQD1. We order the chip from Hypres and when it arrives, dice it up into the nine SQUIDS for use in the probe. The procedure for mounting the SQUIDS into the probe is described in section C.1.2, p. 164.

The inside dimension of the SQUID loop, $10\text{ }\mu\text{m}$, ultimately limits the spatial resolution of the SQUID. Redesigning the SQUID with a smaller loop would, in principle, improve the spatial resolution. However, the largest obstacle to increasing the spatial resolution is the SQUID-sample separation. We have difficulty achieving a SQUID-sample separation less than twenty micrometers and in practice the separation is typically closer to fifty micrometers. We have designed SQUIDS with smaller geometry, but have never used them, nor tested them. These smaller SQUIDS are described in design specification APNSQD2.

A.4 Electronic design

The electronics used to measure the flux impinging upon the SQUID use the well known flux-locked loop.³ Additionally, the electronics used for this probe have had the analog phase detector of Ref. [109] replaced with a digital phase detector.

A.4.1 Digital phase detector

The digital phase detector was designed by Fred Cawthorne and put together in the electronics shop at the University of Cincinnati in collaboration with Rick Newrock. The schematic for this phase shifter is shown in Fig. A.5. The digital phase detector has a resolution of eight bits, yielding a lowest significant bit equal to 0.025 radians.

³See the excellent discussion in Ref. [109] and the references contained therein.

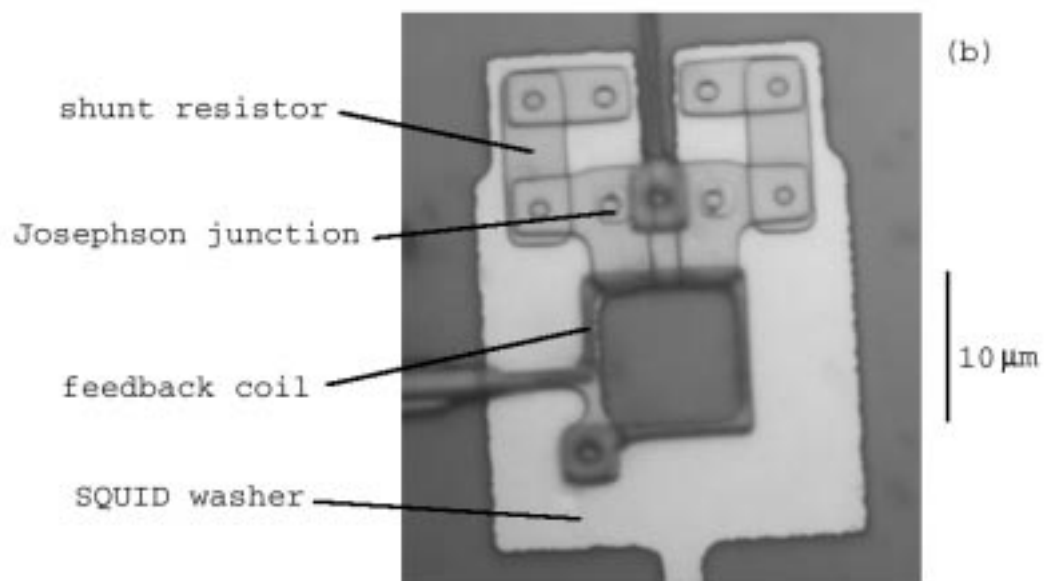
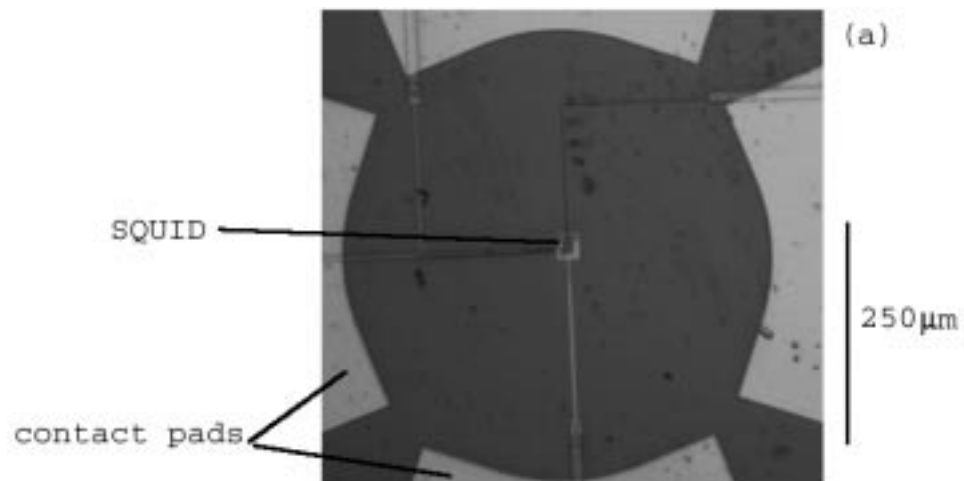
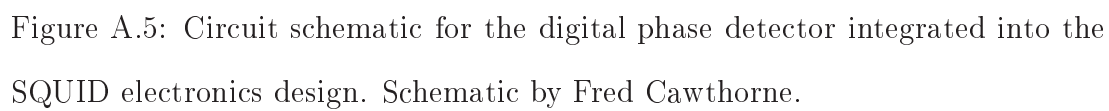


Figure A.4: (a) Optical micrograph of SQUID tip, detailing contact pads. (b) Optical micrograph of SQUID washer.



The following description of the digital phase detector was prepared by Fred Cawthorne:

Digital Phase Detector

The key portion of the following circuit is the CD4066 quad bilateral switch[114], connected as a switching type phase sensitive detector.

System timing is derived from a 25.6 MHz crystal clock[115]. The clock is divided by two presetable 8 bit dividers, type 74ALS867A[116]. One of the two is preset at the terminal count and the other is programmable by a circuit board mounted DIP switch. The 100 kHz output of the preset divider, U2, is buffered by opamp U4B to allow external monitoring of the clock.

By applying these two phase adjustable 100 kHz clocks to two opposing quadrants of the detector, a DC error voltage may be derived during nonsynchronous periods in signal applied to the external input port. The input from the squid preamp is applied to 1 and 8 of the detector with reference to common at pins 4 and 11. U4a amplifies the error voltage and damps spurious harmonics by the use of C3.

To set up the proper phase relationship between clock quadrants:

1. Remove all AC bias from the squid.
2. Set the experimental baseline state in the squid, normal or not.
3. Set the shift code for U1 (using the DIP switch S1) so that the error voltage output from the detector is zero. Note that switch nine is a phase reversal switch.

This completes the setup procedure. Any phase shifts in the input signal from the normal state will produce a bipolar error voltage proportional to the phase error between the system clock and the squid signal.

A.4.2 Electronic frequency response

Once the SQUID electronics and SQUID are integrated together, we can measure the frequency response of the system. Ultimately, the output from the electronics passes through an integrator, so the band pass of the electronics cannot be any greater than that of the integrator. The band pass of the integrator is designed to be about 10 kHz. We used a Hewlett-Packard 3562A spectrum analyzer[117] to measure the frequency response of a SQUID (sitting in the experimental Dewar) coupled with the SQUID electronics. We can see, in Fig. A.6 that $1/f$ noise exists below 500 mHz and the white noise persists up to about 10 kHz, where it is cut off by the integrator roll off. The white noise region has a floor of $5.0 \mu\Phi_0/\sqrt{\text{Hz}}$ which translates to $703 \text{ fT}/\sqrt{\text{Hz}}$.

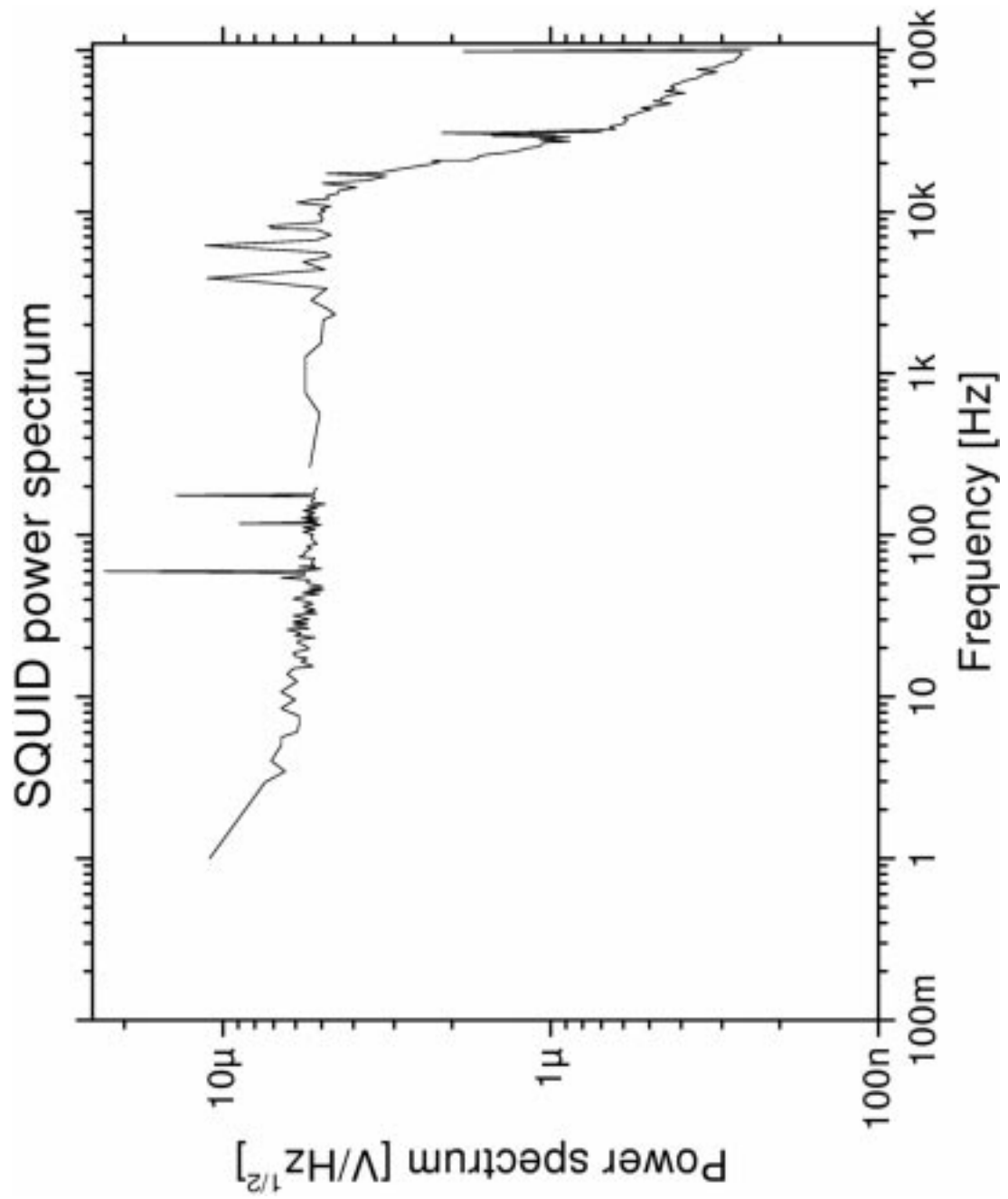


Figure A.6: Frequency response of the SQUID electronics, generated with the SQUID sitting in the probe and Dewar.

Appendix B

Computer control documentation

B.1 General overview

The SQUID microscope controller computer, called the “SQUIDBox,” is a PC computer running a custom program under MS-DOS to control the operation of the microscope. The program serves to provide a manual user interface for positioning the sample and making simple scans. Manual positioning is accomplished through a remote joystick controller, and through a LCD touch screen interface. The SQUIDBox also provides functionality for setting up and running basic data scans.

Scans are effected by moving the sample in a raster type motion under the SQUID while collecting the output from the SQUID electronics in an A/D board. The data is then saved to disk, and may be exported.

Additionally, the SQUIDBox may act as a GPIB device. As such, it can be remotely controlled via another computer.

Our setup is similar to the setup used by Rick Newrock’s group at the University of Cincinnati.

B.2 Computer controller and software

The computer itself is an 486 based PC running custom software under MS-DOS. The computer screen is a Dynapro SC3 Touchscreen[118]. The computer drives the stepper motors which are described in section B.3. The computer is also equipped with an analog to digital data acquisition board which is described in section B.4. The drivers for the various hardware controllers are included in the software for controlling the SQUID microscope.

B.2.1 SCAN CONFIG menu, setting the controller parameters

The SQUIDBox allows the user to set different parameters for scanning, as well as to save those parameters to disk. In addition it provides an interface for manual operation. All of the options are selectable through the touchscreen.

The coordinates used by the controller program are in units of steps for the stepper motors. The x and y numbers used in the program are the relative position of the stepper motors. To move the sample up, both x and y motors are used in tandem. To move the sample left and right, only the y stepper is used. Consequently, to get the real y coordinate from the SQUIDBox coordinate system, one must subtract program x from program y .¹

¹See section B.3, p. 156 for a more complete description of the coordinate systems used in the experiment.

Scanning direction

The scanning direction can be selected as horizontal or vertical which is defined with respect to the probe axis while mounted in the Dewar. The vertical scanning direction moves the sample down to collect one scan line, up and over to do the next scan line. The horizontal scanning mode moves the sample left and right under the SQUID. The vertical scanning mode is preferred for imaging because it minimizes the amount of friction, and consequently heating to the probe. The horizontal mode is useful for making single line scans across the sample.

Scanning velocity

The scanning velocity can be set in the SQUIDBox as well. Two options are available, the forward direction and the back retrace direction. The forward direction is the speed used when collecting data and the backward retrace is the speed used when moving back to get the next raster line. The scanning speed must be slow enough to allow the electronics to track the rate of field change due to sample movement.

Scanning acceleration

Similar to the scanning velocity, the acceleration of the stepper motors can be set by the user. The scanning acceleration defines how quickly the motors reach operating velocity. If this number is too short the velocity will not be constant over the entire scan and the data points will not be evenly spaced in the raster line. The forward and back retrace directions have the same meaning as for the scanning velocity.

Number of columns and rows

The number of data points collected is set by determining the number of rows and columns of data to take. Each column is one raster line. The number of rows is the number of data points collected in each line. The number of rows cannot exceed 4048 points, or the A/D board buffers overflow. This includes the use of multiple channels, *i.e.* when using two channels, use a maximum of 2024 points per line.

Crash detection

The SQUIDBox has a rudimentary SQUID-sample crash detection scheme. It is supposed to abort the scanning if the SQUID suddenly unlocks. It is currently not used, and does not work very well.

Recording potentiometers

The SQUIDBox can record the value of the potentiometers connected to the stepper motors while it is scanning. This might be useful for verifying that the motors are not slipping. This feature is not used either, and the potentiometers have been disconnected to allow a larger scanning area.

B.2.2 GPIB control

The SQUIDBox can be controlled remotely via GPIB using another computer as the master controller. To do this, the SQUIDBox must be put into GPIB mode, otherwise the GPIB functions will not operate. In GPIB mode, the SQUIDBox can execute most of the operations than can be done manually. The list of possible GPIB commands follows.

Table B.1: This is a listing of the GPIB commands accepted by the SQUIDBox. The commands may be sent to the SQUIDBox, and the appropriate action will be taken. If you query the SQUIDBox, it will respond with the requested value.

Command	Description	Range
“SCAND,I”	Set Scan Direction to I <i>Output:None</i>	0=Horizontal 1=Vertical
“CRASHD,I”	Set Crash Detection to I <i>Output:None</i>	0=Off 1=On
“RPOTS,I”	Set to record pot positions to I <i>Output:None</i>	0=Off 1=On
“SCANXV,X”	Set Xvelocity1 (forward scan) to X <i>Output:None</i>	
“SCANYV,Y”	Set Yvelocity1 (forward scan) to Y <i>Output:None</i>	
“SCANXA,X”	Set Xaccel1 (forward scan) to X <i>Output:None</i>	
“SCANYA,Y”	Set Yaccel1 (forward scan) to Y <i>Output:None</i>	
“BSCANXV,X”	Set Xvelocity2 (back retrace) to X <i>Output:None</i>	
“BSCANYV,Y”	Set Yvelocity2 (back retrace) to Y <i>Output:None</i>	
“BSCANXA,X”	Set Xaccel2 (back retrace) to X <i>Output:None</i>	
“BSCANYA,Y”	Set Yaccel2 (back retrace) to Y <i>Output:None</i>	
“NUMROWS,I”	Set NumRows (data points per scan line) to I <i>Output:None</i>	

continued on next page

Table B.1: *GPIB commands continued*

Command	Description	Range
“NUMCOLS,I”	Set NumColumns (number of scan lines) to I <i>Output:None</i>	
“STARTUL,X,Y”	Set Start Upper Left Coordinates to X, Y <i>Output:None</i>	
“ENDLR,X,Y”	Set End Lower Right Coordinates to X,Y <i>Output:None</i>	
“*IDN?,”	Simple Identification Query <i>Output:“Model 1.0 SQUIDBOX”</i>	
“SCAND?,”	Scan_Direction Query <i>Output:“Scan_Direction”</i>	
“CRASHD?,”	Crash_Detect Query <i>Output:“Crash_Detect”</i>	
“RPOTS?,”	Record_Pots Query <i>Output:“Record_Pots”</i>	
“SCANXV?,”	Xvelocity1 Query <i>Output:“Xvelocity1”</i>	
“SCANYV?,”	Yvelocity1 Query <i>Output:“Yvelocity1”</i>	
“SCANXA?,”	Xaccel1 Query <i>Output:“Xaccel1”</i>	
“SCANYA?,”	Yaccel1 Query <i>Output:“Yaccel1”</i>	
“BSCANXV?,”	Xvelocity2 Query <i>Output:“Xvelocity2”</i>	
“BSCANYV?,”	Yvelocity2 Query <i>Output:“Yvelocity2”</i>	
“BSCANXA?,”	Xaccel2 Query <i>Output:“Xaccel2”</i>	

continued on next page

Table B.1: *GPIB commands continued*

Command	Description	Range
“BSCANYA?,”	Yaccel2 Query <i>Output</i> : “Yaccel2”	
“NUMROWS?,”	NumRows Query <i>Output</i> : “NumRows”	
“NUMCOLS?,”	NumColumns Query <i>Output</i> : “NumColumns”	
“STARTUL?,”	Start Upper Left Coordinates Query <i>Output</i> : “StartULx,StartULy”	
“ENDLR?,”	End Lower Right Query <i>Output</i> : “EndLRx,EndLRy”	
“XY?,”	Current Position Query <i>Output</i> : “X,Y”	
“PRETENSION,”	Pretension Command. This command is deprecated. it is better to do this using the GOTOXY command. The pretension command moves to Start X+6000,Y and may be dangerous to do if you are not careful. <i>Output</i> :None	
”START,”	Start Scanning <i>Output</i> : “STARTSCAN” or “NOSCAN”	
“GOTOXY,X,Y”	Move SQUID to position X,Y <i>Output</i> :None	
“STATUS?”	Ask the controller what it’s doing. <i>Output</i> :1 if moving, 0 if doing nothing	

The GPIB Primary Address is set to 6, but can be changed. Just redefine ADDRESS at the top of the program.

A file is created called `gpibout.dat` which will allow recording of status variables (*e.g.* `gpib_readpending`, `gpib_writepending`, `gpib_readbuf`, etc.) to as-

sist in debugging.

The scanning mode is somewhat complicated. The controller-SQUIDBox dialog is essentially the following (for a single channel scan):

Controller Command	SQUIDBox Response
"START, "	"STARTSCAN"
	"FILES, 1"
"FILE1, NAME?"	"data10.asc"
"SEND, "	

At this point the interrupt routine is disabled on the SQUIDBox, and the `ibwrtf-ibrdf` file transfer is initiated. The full sequence for a series of channels or potentiometer files continues the above sequence until all files are read.

Known Bugs

In GPIB mode the SQUIDBox will sometimes hang at the end of a scan, without responding to the GPIB controller. This can be worked around by manually sending an arbitrary command to the SQUIDBox. However, after sending the arbitrary command we will have to manually copy the data files from the SQUIDBox over to the GPIB controller.

Also, aborting the scan might cause problems with SQUIDBox. The error handling routines are not yet adequate.

B.3 Stepper motors

The stepper motors are driven with an Oregon Microsystems PC Motion Controller board[119]. Additionally, the stepper motors are each attached to a potentiometer. The potentiometers were used to give a rough measure of where

the stepper motors are relative to the sample location. The potentiometers turn when the stepper motors turn, and the resistance can be read out by the program. This information might be recorded using the `Record_Pots` feature in the program.

In practice, this information is not useful. The mechanical details of the stepper motors *vis-à-vis* the scanning mechanism are discussed in more detail in section A.2.4, p. 142. Furthermore, the potentiometers have been disabled in order to increase the scanning range.

B.3.1 Coordinate systems

To understand the coordinate system that is used internally by the SQUIDBox, and the coordinate system that is used for the output data files, we must discuss how the computer scans. All discussion relates to the probe *as mounted in the Dewar*. Due to the physical arrangement of the pushrods, the sample stage will move up and down when both of the pushrods are moved simultaneously. The general relationship between the coordinate system as seen in the probe, and the coordinate system in the images is shown in Fig. B.1.

Moving the sample up and down along the axis of the probe corresponds to the x (horizontal) direction in the data images. To move the sample left and right, only the tall pushrod moves. This corresponds to the y (vertical) direction in the data images. For the data files, the origin will always be the upper left corner of the image and x and y are measured in terms of stepper motor steps.

Internal to the SQUIDBox, a different set of coordinates is used. This coordinate system relates the position of the stepper motors instead of the sample position. However, these coordinates are also measured in stepper motor steps.

The origin, internal to the SQUIDBox can be fixed arbitrarily.

The relationship between the SQUIDBox internal-coordinate system, the output-image coordinate system and the actual position of the sample is best explained by example. We use capital letters X and Y to indicate coordinates in the system of the output images and lower case letters x and y to indicate coordinates in the system of the SQUIDBox. Using the SQUIDBox to set up an image, we must define an origin, an upper left (UL) and a lower right (LR) position. UL and LR indicate the start and end of a particular scan.

Using the joystick control, and starting from the origin, we would first move the sample up as far as we wish to scan. This positions the sample at $(x_{\text{upper}}, y_{\text{upper}})$. Next we move the sample to the left, which positions the sample at $\mathbf{x}_{UL} = (x_{\text{upper}}, y_{\text{upper}} + y_{\text{left}})$. To set the lower right position, we do a similar process, moving the sample down first to $(x_{\text{lower}}, y_{\text{lower}})$ and then over to the right $\mathbf{x}_{LR} = (x_{\text{lower}}, y_{\text{lower}} + y_{\text{right}})$. If we now take a scan using these coordinates, we obtain a data file with coordinates $\mathbf{X}_{UL} = (0, 0)$ and $\mathbf{X}_{LR} = (X_{\text{lower}} = x_{\text{upper}} - x_{\text{lower}}, Y_{\text{right}} = y_{\text{left}} - y_{\text{right}})$. These calculations are essential for the interpretation of the data images and for the computation of new scanning coordinates for *e.g.* zooming in for detailed scanning.

We may also refer to coordinates based on the location of the pushrods. Each pushrod has a millimeter scale which refers to how far the pushrod has moved. The resolution of the millimeter scale is difficult to read accurately, so we use these numbers as rough position guides only. Should something go wrong, we can use these numbers to find the sample again.

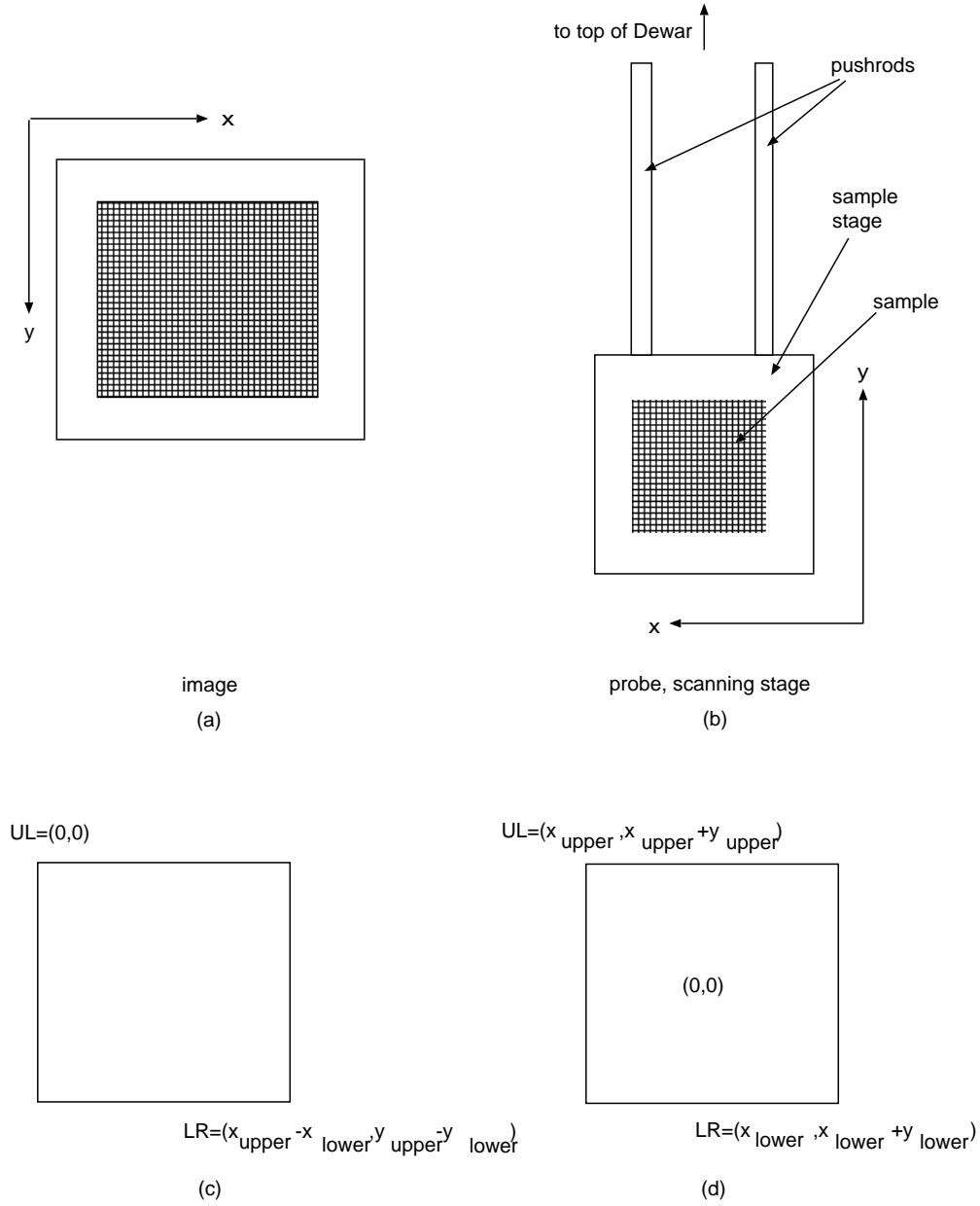


Figure B.1: Arrangement of coordinate systems in probe and images. (a) Coordinate axes for an image. (b) Coordinate axes for the probe. (c) Coordinate value relationship for an image. (d) Coordinate value relationship for the SQUIDBox.

B.4 A/D board

The SQUIDBox has a National Instruments AT-MIO-16X A/D board that is used in data collection[120]. The board has six channels which can be selected. Each of the channels also has an amplifier whose gain can be set in the SQUIDBox. Channel 1 generates a file called `dataX.asc`, where `X` represents an identification number for the file. Channel 1 generally collects the output directly from the SQUID electronics. If there are other channels active, those channels will have output files generated named `chY_X.asc` where `Y` represents the channel number (between two and six) and `X` represents the identification number for the scan. All files from the same scan will have the same identification number. The number `X` is an identifier of the data run and is chosen successively by the SQUIDBox.

B.5 Manual control

The sample may also be moved around manually using the **MANUAL** control menu. This menu provides the user with the current coordinates and allows the user to set the Upper Left and Lower Right coordinates for a scan. Additionally, the user can enable the joystick control (described below). Selecting a field on the touch screen containing the various coordinates allows the user to change the value of that field. For example, by touching the value of the current coordinates, the user will be prompted to enter the value of the new coordinates. Likewise, touching the value of the **Upper Left** or **Lower Right** prompts the user to enter new values for those coordinates.

By selecting **Start Scan**, the user can start a single scan, using the parameters set by the user. When the scan is finished, the user is prompted to save the

scan to a Zip disk or floppy disk.

B.5.1 Joystick control

The joystick control may be enabled when the controller is in manual mode. The joystick is constructed using video game parts. The hardware to drive the joystick was designed by Fred Cawthorne and runs on a modified version of his 6811 Board[121, 122]. The joystick may be used to drive the sample around *in situ* or when aligning the SQUID and sample at room temperature. It is better to pulse the joystick and move the sample in short bursts. A bug occasionally causes the SQUIDBox to continue to move the sample even if the joystick is released.

The software required to run the joystick is stored on an EPROM inside the controller box.

B.6 Scanning

During scanning, touching the screen anywhere amounts to an **ABORT** command. Do not attempt to change the data display while scanning is occurring. This is a design feature to make it easy to abort the scan should anything go horribly wrong. So that catastrophe may be avoided it is preferable to abort the scan as easily as possible. It is possible to have the SQUIDBox redo a single scan line, by selecting **REDO LINE**. This is useful if the SQUID unlocks during a scan line.

Appendix C

Experimental procedure

C.1 Preparing probe for measurements

Before anything else we make sure that the electrical contacts within the probe are good from the room temperature connectors down to the connectors inside the vacuum can. After this is done we mount the sample on the sample holder and align the SQUID and sample. Finally, we cool the probe to 4.2 K and begin measurements.

C.1.1 Sample mounting

Preparing to make sample contacts

The sample must present a flat surface to the SQUID tip. There may be no wires or contacts sticking up above the surface of the sample. This insures that the SQUID cannot crash into anything during normal operation. The SQUID (as well as the sample) may be destroyed if it crashes.

Making contacts to a sample this way is non-trivial. One example of how this has been done is shown in Fig. C.1. The sample chip is mounted to a silicon or

sapphire wafer using stycast epoxy. For the stycast, we use Black 2850FT with catalyst 24LV[123]. Gold leads are evaporated such that they overlap the contact pads on the sample chip surface and make contact to the bottom silicon wafer. Gold or copper wires can then be attached to using silver paste or indium solder such that they remain below the surface of the sample chip.

Evaporation of contact details

This applies equally to the contacts made to the sample as well as to the contacts made to the sample. Successful evaporation of gold leads is a straightforward, though perhaps tedious process. First, we paint photoresist with a small wire to mask off regions for the evaporated gold. We bake the photoresist for thirty minutes at eighty degrees centigrade to harden it. After baking, we double check under the microscope that photoresist coverage is good and then mount the sample into the evaporator. We use the ion mill head with the rotating sample stage, and verify that the sample may rotate freely over the evaporator boats. The evaporation proceeds according to the following:

- Ion mill the sample for 30 seconds to clean the surface.
- Evaporate 20 to 50 Å chrome, followed by about 2000 Å gold. During the evaporation we rotate the sample through the evaporating material to cover all of the surfaces.
- Remove the sample tip from the evaporator and lift off the photoresist.
- Evaporated gold does not typically stick to the stycast epoxy so we use silver paint to connect over the stycast.
- Attach wires to these leads using silver paste or indium solder.

Mounting sample into probe

The entire assembly mounts with Apeizon N vacuum grease[124] to the sapphire cylinder of the sample holder in the probe. The sapphire cylinder is clamped into a gold coated copper cold finger. This cold finger is thermally sunk to the helium bath through copper heat sinking. Around the sapphire cylinder a solenoid is wound which applies magnetic field to the sample.

C.1.2 SQUID mounting

We prepare the SQUID tip in a similar fashion to that of the sample. This is done by taking a SQUID chip (as cut from the Hypres delivered wafer) and mounting it to a sapphire cone with stycast epoxy. At this point the SQUID chip is square and we grind it down until it is circular and the same size as the tip of the sapphire cone (about 1 mm).

Grinding is started using a Dremel tool with an emery wheel. Grind the SQUID under a microscope to observe the grinding process. The emery wheel removes fairly large chunks from the SQUID, so at some point is unsatisfactory to grind the SQUID further. The grinding is completed using a polishing wheel.

Contacts are made to the SQUID chip by evaporating gold onto the contact pads and over and down the sides. This gold should cover the stycast epoxy and go down to the sapphire cone. Indium wets to sapphire at about 300° C and can be used to contact the evaporated gold. We have also had good luck using a combination of silver paste and silver paint. Small copper or gold wires are then used to contact the indium and connect to the rest of the probe wiring. This layout is sketched in Fig. C.1. We have tried many different ways to make these contacts: silver paint and paste and various solders. In all of the cases, the

big problem is thermal cycling. The SQUID must be thermal cycled in vacuum, otherwise ice crystals form that eventually break the contacts free. This makes testing in a dip probe problematic because the SQUID is not put in vacuum, nor is the Bellcore Dewar neck large enough to make a vacuum can that could contain the SQUID holder. A good solution would be to make a special probe to insert into a standard experimental Dewar. We have not done this. We dip test the SQUID a couple of times and verify that it works with the electronics anyway.

The longest lasting SQUID survived for approximately eighteen months, and had indium contacts, it crashed into a sample which destroyed it. We gingerly test the SQUID in the dip probe and make sure that it thermal cycles slowly. We only thermal cycle it one or two times this way. Once it works, we mount the SQUID in the probe and only thermal cycle it in vacuum. The contacts should work okay with this procedure. With this method we are careful of the wires themselves and examine them for kinks that may break upon subsequent thermal cycling. The SQUID will likely be thermal cycled many times before any useful data is taken so its important to get this to work properly.

The SQUID mounts into the probe similarly to the sample. The SQUID sits on the end of a sapphire cone which is clamped into a gold coated copper cold finger. This copper cold finger is thermally sunk to the helium bath by means of a copper heat sinking, separate from the sample. Provided that the vacuum in the probe is good the sample and the SQUID should both be thermally isolated from each other. In practice the SQUID needs considerable heat sinking to maintain a constant temperature.

The SQUID cold finger is mounted in a Delrin plate which holds the SQUID above the sample. The SQUID height above the sample can be controlled with a

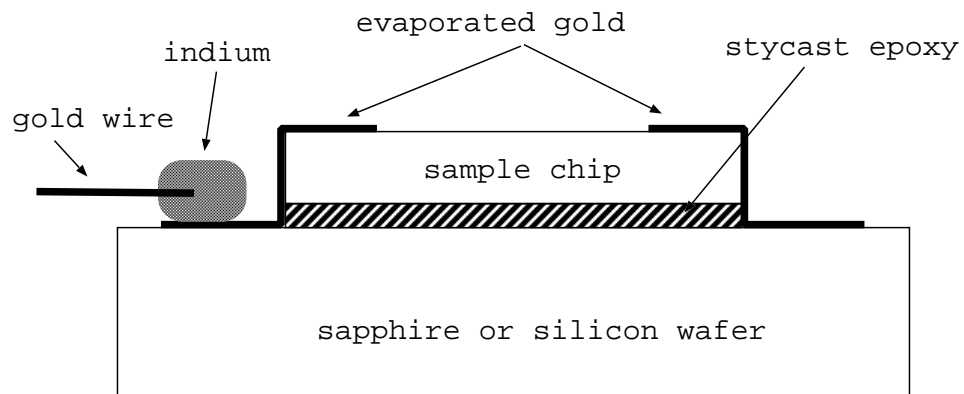


Figure C.1: Making contacts to the sample such that nothing protrudes above the plane of the sample chip

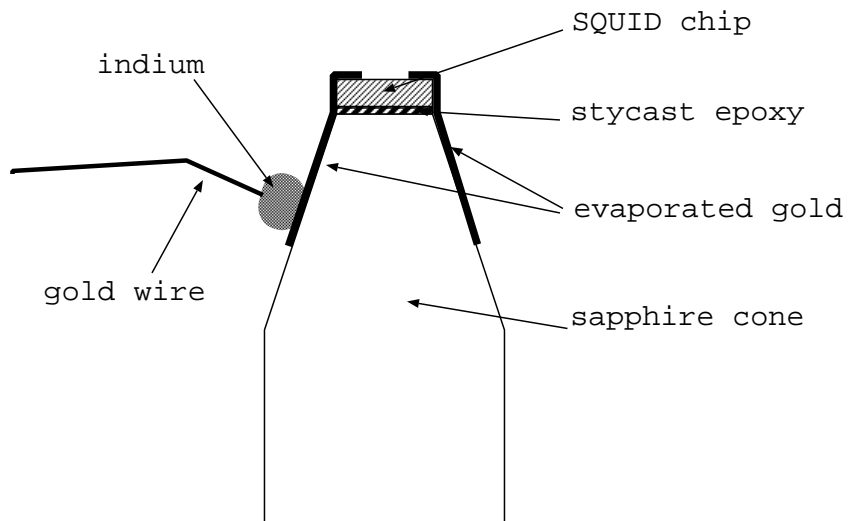


Figure C.2: Contacts made to the SQUID such that nothing protrudes above the SQUID tip.

z -wedge. Moving this wedge in and out raises and lowers the SQUID above the sample. There is considerable backlash in this mechanism and it cannot be relied upon for measurements nor can it be calibrated.

C.1.3 SQUID and sample contacts

After mounting, we check the all of the contacts from the vacuum can up to the room-temperature flange. Typical pinouts are listed in Table C.1 along with typical resistances at room temperature.

C.1.4 Sample and SQUID alignment

Once both the sample and SQUID are mounted in the probe and their contacts are okay, we align them with respect to each other. We bring the two close to each other using the z -wedge and by adjusting the SQUID mounting screws so that the SQUID is level with respect to the plane in which the sample moves. We do this using a stereo microscope. We then repeat the process with the sample.

Next we attach the stepper motor drive to the probe and use the joystick control to move the sample around while watching with the microscope. we adjust the SQUID and sample until they are aligned such that the SQUID-sample separation does not change over the entire range of the sample's motion.

Once the alignment is complete we record the coordinates. Generally the center of the sample is taken as $(0, 0)$ in the coordinate system of the SQUIDBox. Relative to this location record the upper-left and lower-right coordinates of the scan and save these values in the computer. Note the physical relationship with respect to the stepper motor coordinate system (used in the SQUIDBox) and the tick marks on the x, y, z pushrods.

Probe pinouts at room temperature

	SQUID	Temp	He Level
A	transformer feedback coil	$V+$	$V+$
B		$V-$	$V-$
C		$I+$	$I+$
D		$I-$	$I-$
E	I_{bias}	sample heater 33.5Ω	NC
F			NC
G	coil 11.4Ω	$V+$	NC
H		$V-$	NC
J		$I+$	NC
K	SQUID heater 40.8Ω	$I-$	NC
	Sample 1	Sample 2	
A	plastic thermo	$V+$	NC
B		$V-$	NC
C		$I+$	NC
D		$I-$	NC
E	NC	solenoid 15Ω	
F			
G		NC	
H		NC	
J		NC	
K		NC	

Table C.1: Room temperature flange pinouts at room temperature. All resistances listed are those measured at room temperature

Probe pinouts in liquid nitrogen

	SQUID	Temp	He Level
A	transformer feedback coil	$V+$	$V+$
B		$V-$	$V-$
C		$I+$	$I+$
D		$I-$	$I-$
E	I_{bias}	sample heater $30.0\ \Omega$	NC
F			NC
G	coil $8.0\ \Omega$	$V+$	NC
H		$V-$	NC
J	SQUID heater $30.0\ \Omega$	$I+$	NC
K		$I-$	NC
	Sample 1	Sample 2	
A	$V+$	NC	
B	$V-$	NC	
C	$I+$	NC	
D	$I-$	NC	
E	NC	solenoid $15\ \Omega$	
F	NC		
G	NC	NC	
H	NC	NC	
J	NC	NC	
K	NC	NC	

Table C.2: Room temperature flange pinouts at 77 K. All resistances are measured at 77 K

Probe pinouts in liquid helium

	SQUID	Temp	He Level
A	transformer feedback coil	$V+$	$V+$
B		$V-$	$V-$
C		$I+$	$I+$
D		$I-$	$I-$
E	I_{bias}	sample heater $28.0\ \Omega$	NC
F			NC
G	coil $2.2\ \Omega$	$V+$	NC
H		$V-$	NC
J	SQUID heater $27.8\ \Omega$	$I+$	NC
K		$I-$	NC
	Sample 1	Sample 2	
A	$V+$ plastic thermo $I+$ $I-$	NC	
B		NC	
C		NC	
D		NC	
E	NC	solenoid $1.7\ \Omega$	
F			
G		NC	
H		NC	
J		NC	
K		NC	

Table C.3: Room temperature flange pinouts at 4.2 K. All resistances are measured at 4.2 K

Maximum scanning range

The x, y stage has a maximum travel range. The tall push rod should not be raised to less than 40 mm, on its millimeter scale because parts of the sliding mechanism can run into stationary parts of the probe and wreck the scanning mechanism. Always check for obstructions to the scanning mechanism before scanning, and note of any features that might interfere with the scanning.

After many thermal cycles, the Delrin housing for the positioning mechanism may begin to catch the sample holder because it shifts out of alignment. If this occurs, the housing should be fully disassembled, and then reassembled paying strict attention to tolerances on each side, to ensure that the sample holder may slide freely. Problems with sliding may not manifest at room temperature, and may require dipping the scanning mechanism and housing into liquid nitrogen in order to test properly.

After recording these numbers the SQUID can be moved to a safe position for the rest of the procedure. Back the SQUID far away from the sample and move the sample so that the SQUID is not positioned over anything important. Generally we move the SQUID over a gold pad and position it there. Typical values for all of these alignment parameters are shown in Table C.4.

After verifying that the contacts are good and aligning the SQUID and sample we move the probe into the screened room. Be extremely careful of the wires when doing this as they are prone to catch on things and break. Generally we recheck all the contacts before tightening the screws for the vacuum can. There is a lead liner for the vacuum can which is supposed to help act as a magnetic shield. This lead liner has never been used primarily for two reasons. First fitting everything into the vacuum can is a difficult proposition and requires some contortion to

	pushrods			steppers	
	tall (mm)	short (mm)	<i>z</i> -wedge (mm)	<i>x</i>	<i>y</i>
Centered	72	37	5	0	0
Upper Left	68	30	5	154490	41650
Lower Right	106	45	5	-207133	-40587
Safety	89	42	20	-44000	-44000

Table C.4: Typical values for the alignment parameters of the SQUID and the sample.

make it work; there is simply no room for the lead can. Second the lead can may trap flux and frustrate, rather than help, our attempt to reduce the ambient flux.

C.2 Pumping down and leak checking

Evacuate the probe using the diffusion pump station. The diffusion pump has a base pressure of about 2×10^{-6} torr. We have achieved this pressure using the diffusion pump alone, but only once. It took about two days to reach this pressure so just be patient. There are so many crevices that virtual leaks are a big problem, so its hard to tell if there is a real leak or not. Generally we pump for 24 hours until the probe pressure reaches about 10^{-5} torr.

At this point it is a good time to leak check the probe. There are so many things which can go wrong and the entire procedure takes so much time that we have found it beneficial to leak check the probe every time it is used. However, at room temperature the probe generally proves to be leak tight. Important things to check at this point are the large indium O-ring sealing the vacuum can as well as the fittings at the top. The connectors on the cold flange are known to leak,

but generally only leak when in liquid nitrogen or helium. Check them to be safe. In order to finish leak checking it is necessary to cool the probe in liquid nitrogen.

C.3 Pre-cooling in liquid nitrogen

The leak checking procedure can be finished by putting the probe into the experiment Dewar and cooling with liquid nitrogen. The most important thing is to cool the probe slowly. We have found that cooling the probe quickly results in vacuum leaks opening up on the cold flange. Begin with an empty Dewar. Make sure the Dewar contains no nitrogen nor debris at the bottom. Any debris in the bottom may block the transfer lines when you later try to blow the nitrogen out of the Dewar.

Clamp the small fill line to the side of the vacuum can before continuing.

If the Dewar is warm simply lower the probe into the Dewar, and bolt the flange to the top of the Dewar. Reattach the diffusion pump the probe and continue to pump on the probe and monitor the pressure. We now start to cool the probe by trickling liquid nitrogen into the Dewar. Do this slowly. we prefer to use the small storage Dewar, pressurized to 5 psi. At this pressure the nitrogen transfers slow enough rate is slow enough that the probe is not stressed. If you use a large storage Dewar the pressure is 22 psi and it is easy to transfer nitrogen too quickly. The nitrogen transfer should take from fifteen minutes to a half hour.

We never lower the probe into the Dewar if there is already liquid nitrogen in the Dewar. This puts a lot of thermal stress on the vacuum joints and causes leaks. We have tried lowering the probe slowly into a nitrogen bath and it does not work.

Watch the pressure in the probe as you transfer the nitrogen. It should drop continuously. Sometimes the pressure may jump up and then drop back down. This is okay and just means that a virtual leak opened up. If the pressure shoots up and cannot be pumped down this means that a leak has opened up on the cold end of the probe.

Its necessary to try and find the leak. Let the probe fully cool in nitrogen. The thermometers work at nitrogen temperature so you can tell that the probe is fully cooled. Once the probe is fully cooled, pull it out of the Dewar and leak check it immediately before it has time to warm up. The leak can often be found this way. Leaks are often found in the solder joints for the electrical feed throughs on the cold flange.

Before trying to repair the leak, let the probe warm fully to room temperature and repeat the leak checking procedure. Liquid nitrogen leaks frequently go away at room temperature. Additionally the leaks do not often repeat, so try again. Cool very slowly into nitrogen, slower than before, and see what happens.

If no leaks develop you can proceed to cool with liquid helium. If the leaks do not go away they must be assessed. Any loss of vacuum in the probe means that the thermal isolation between the SQUID and the sample will be degraded. If the leak is small enough that we can pump on it continuously and keep a vacuum around 10^{-5} torr or smaller then we do so. If the leak is too large then it will have to be repaired.

C.4 Cooling with liquid helium

Before moving on, we check the electrical contacts in the probe again. See table C.2 for typical resistances at 77 K. This is important because we can save a

lot of time if we find a bad contact here. If there is a bad contact we pull the probe out to make a repair and are careful to blow the liquid nitrogen out of the Dewar before we pull the probe out. If we do not do this, the nitrogen will stay in the Dewar for a long time, and we do not want to lower the probe into nitrogen bath. Instead, we only want to trickle nitrogen slowly around the probe.

In addition to checking the electrical contacts at 77 K, we also check the scanning mechanism and verify that it can move smoothly over the full range of required travel. If the mechanism binds up, it will be necessary to open the probe and figure what is wrong. It may be necessary to disassemble the entire Delrin housing and reassemble to make sure that the mechanism operates smoothly.

The trick to cooling with liquid helium is to cool as slowly as possible. Since the plastic has very low thermal conductivity, a long wait is required to draw all of the heat out of the plastic. From 77 K to 4.2 K, cooling takes between two and three hours.

It is also necessary to put helium into the vacuum can as exchange gas, otherwise the plastic will never cool. At 77 K, we put about 50 mTorr of helium gas. We have also used hydrogen as exchange gas, but it freezes out at about 11 K and then it is impossible to cool the probe below 11 K.

Blow the liquid nitrogen out of the Dewar.

Begin the liquid helium transfer, while monitoring the temperature. The SQUID will cool the fastest because it is the best heat sink. We monitor closely the plastic temperature and use that as a guide. As long as the plastic continues to cool, everything is fine. In general we do not want to condense helium into the Dewar until the plastic has cooled to 4.2 K. This process does not require much effort, but must be monitored to insure that the transfer continues slowly.

It is essential that we cool the probe cool uniformly and slow enough so that the plastic temperature remains the same as the vacuum can temperature. It is easy to cool the vacuum can to 4.2 K while the plastic temperatures remains quite high (30 – 40 K). In this case, the helium exchange gas condenses on the inside surface of the can and the plastic cease to cool at any reasonable rate. If this happens, we allow any liquid helium to boil off, and the vacuum can is allowed to warm above 4.2 K, before attempting to re-cool the probe. LakeShore germanium thermometers are mounted on the sample, SQUID, cold flange and plastic to monitor the temperature during cooling.

C.5 Finding the sample

Once the probe is at 4.2 K, verify that the SQUID is working properly and check the electrical contacts. Typical resistances at 4.2 K are shown in table C.3.

Because of thermal contraction, the sample shifts inside the can when it is cooled to 4.2 K. This makes it somewhat challenging to find the sample once everything else is set to go. We have found that it's easiest to put an AC field into the sample solenoid, use a lock-in amplifier to look at the same frequency in the SQUID electronics output and scan around. There are always gradients in the DC remnant field which sometimes make it difficult to search for the sample by using a DC field into the sample solenoid.

We do not move too close to the sample initially. It is possible to knock the sample off the sample mount if the SQUID tip catches an edge of the sample. However, it is often difficult to find the sample location without moving somewhat closer. We always move closer to the sample while watching the SQUID output. If the SQUID touches the sample, it will unlock, and if we are gentle, we

can back away and there should be no problems.

It is generally easy to find the sample using this method and then we recheck the coordinates.

Once the sample is located, we bring the SQUID closer to it and try to get as close as possible. This is tricky because the sample may not be level any longer. We start in the middle of the sample, and move in until I just touch. Then we back the SQUID away and attempt to move around using the joystick control. We move over the entire scan range and make sure that the SQUID and sample do not touch. If all is well, we try a scan and it should appear as we expect. It is difficult to know how close the SQUID is to the sample or if the sample is even level with respect to the plane of the SQUID. The best way to figure the SQUID height above the sample is to scan an image which has features of known size. Unfortunately, not all samples have such features.

C.6 Day to day operation

The Dewar hold time is about twelve hours. So, we transfer helium every twelve hours. We fill the liquid nitrogen jacket every 24 hours. At this point, aside from making sure the cryogenes are full, there is not too much to worry about.

If the vacuum is poor, we may need to pump on the probe continuously.

C.6.1 Holding

If no data is to be taken, the probe can safely be left for 24 hours between helium transfers. In this time, the probe will warm to about 20 K to 30 K. This amount of heating is not a problem, and the probe can safely be re-cooled to 4.2 K for

the resumption of data collection.

It takes approximately 48 hours for the probe to warm to 100 K. At this temperature, the probe should be held in liquid nitrogen to insure that it does not warm any further. It will also be necessary to cool in nitrogen to 77 K before re-cooling to 4.2 K. Warming above 77 K has proven to cause faults arising from thermal stresses to the electrical contacts and the vacuum seals.

C.6.2 Scanning

During scanning, it is essential to mitigate the effects of heating due to friction in the slider mechanism. This heating causes not only the sample to warm slightly, but also the SQUID. We wish to hold the SQUID to as constant a temperature as possible, otherwise the critical current will drift, which in turn causes the SQUID voltage to drift, shifting the measured output from the SQUID electronics.

This effect has been measured more carefully by warming the SQUID and noting the change in output, as discussed in section A.2.2, p. 140 and shown in Fig. A.3.

Neocera LTC-21 Cryogenic Temperature controllers are used to control both the SQUID and sample temperatures during scanning. The control parameters for the temperature controllers must be set each time and are usually quite different between data runs. This is because we often change the heat sinking or the quality of the vacuum is different between data runs. Once stabilized the temperature controllers do an effective job of maintaining both the SQUID and sample temperatures to within 0.01 K. Typically the SQUID is operated at a temperature of 4.8 K.

C.7 Warming up

We allow the probe to warm to at least 77 K before pulling it out of the Dewar. Otherwise thermal stress can cause vacuum leaks. Typically we let the probe sit in the Dewar and warm up as slowly as possible.

When the probe is at 77 K or greater, we pull it out of the Dewar and let it warm to room temperature. we do not break the vacuum until it has fully warmed to room temperature (even deep inside the can). Otherwise, ice will form inside the can. The ice crystals seem to degrade the contacts; especially the SQUID contacts. Typically, wait twenty-four hours for the probe to warm to room temperature from 77 K.

C.8 Vacuum leak information

This appendix contains information about finding and repairing the vacuum leaks. This is information that was sent to me from John Markus of Rick Newrock's group at the University of Cincinnati.

Hi Aaron,

Sorry to hear that you still have some leaks, but relieved that it seem to be the feed throughs rather than a weld. (by the way, we've recently opened our probe and the cold flange patch weld is on the inside of the vacuum can in case you haven't noticed it yet). The following may or may not help but here is an outline of the technique I've used to get successful joints when reusing those low temp. feed throughs and brass flanges. I prefer to use a hot plate rather than a heat gun because the temp is easier to control and it's easier to

inspect and work on the part without heating up my hands and face.

1. support the brass flange with feed through connector side up on a $\frac{7}{8}$ " OD. by $\frac{1}{2}$ " long copper pipe on a hot plate.
2. increase the hot plate temp slowly until the old solder melts
3. by grabbing a few pins with needle nose pliers, remove the feed through from the flange and quickly wipe away any extra solder from the feed through. I find a cloth rag works well or you can clean up the surface with a soldering iron. Just try to have the sides and step tinned without any lumps so it will fit back into the flange
4. clean up the brass flange while it is still hot, I use Stay-Clean liquid flux on a cotton swab to remove extra solder
5. re-tin the side surfaces of the flange if necessary
6. melt new solder in the step of the flange so there is a nice continuous bead of molten solder all the way around the ring. Our solder¹ is in awkward squares so we melt it on a soldering iron and let drops fall on a glass plate to get usable flat drips that can be cut with a razor blade and applied to the part using tweezers
7. apply Stay-Clean liquid flux around the feed through with a cotton swab
8. with needle nose pliers set the feed through into position on the flange. If it doesn't really fit do some extra solder blobs that

¹This low temperature solder is Cerrolow 117 or 137. The number refers to the melting point in Centigrade.

were difficult to clean, preheat the feed through with a heat gun until the solder flows and then install the feed through

9. set a small mass on the pins of the feed through to keep it from “floating” up on the solder. I use a $\frac{3}{4}$ ” long piece of $\frac{1}{2}$ ” OD solid copper rod.
10. add solder to any gaps around the perimeter of the feed through
11. turn off the hot plate and don’t move the assembly until it is cool enough to touch and hold in your hand
12. wash the assembled parts (maybe in baking soda solution) to neutralize and remove the nasty acid flux. then dry completely with compressed air.

I don’t recall the melting temp of the solder we used and I don’t have any info on those feed throughs but I would guess they can handle a temp higher than 117F so you may want to try another solder. The black filler on those is probably some glass-filled epoxy and since it is a solder type connector, should be able to handle rather high temperatures. If you have a spec. sheet on them it may recommend a solder to use or at least a maximum temp. (If you find out anything I’d appreciate a note about it) Maybe you shouldn’t try a higher temp unless you’ve got some spares sitting around, I guess their pretty expensive—like \$100 for one tested to 4 K by the company.

Leak checking is always annoying and cold leak checking is even worse. I assume you’ve got some mass spectrometer vacuum leak detector tuned to ^4He . My number one rule and advice to students is Do Not use too much test gas. If you know you have a leak then

careful, minimum He application is key. He atoms are very fast and with large amounts flying around its very hard to pin-point a leak. As a test gas applicator, I've taken a damaged needle valve from the gas handling system of a deposition chamber and attached to it a thin piece of $\frac{1}{16}$ " OD flexible copper tubing about 6" long. I set the He flow rate with the needle valve by watching the bubbles in a beaker of water when the tip of the wand is submerged (for fine leaks maybe 1-2 bubbles per second). Then move the wand around one suspect joint or part of joint at a time waiting a short time before moving to the next joint. Since He rises in air and I assume the probe is hanging vertically, start at the top and work your way down. For leak checking while at ℓN_2 temps, try incrementally lowering a small Dewar of ℓN_2 off the probe and testing those joints just above the liquid level. This does two things for you, 1. it helps keep the joints cold and 2. it block random He from possible leaks below the liquid level. You may need to use a higher He flow rate to overcome the boiling ℓN_2 gas flow around the test area. I have a 10 liter Nalgene Dewar (Fisher Scientific cat no. 10-194-100d \$225) that I raise and lower on the stationary hanging probe with a lab jack. This Dewar is small enough to be manageable yet deep enough to submerge the cold flange, except for the double feed through. (if your lab doesn't have something similar, check in the physics departments lecture demonstration equipment for one you could borrow.)

Good luck and keep me posted on your progress. If any of the above is unclear or you have other questions just send me a note.

-John

BIBLIOGRAPHY

- [1] W. Meissner and R. Oschenfeld, Die Naturwissenschaften **21**, 787 (1933).
- [2] E. Zeldov, A. I. Larkin, V. B. Geshkenbein, M. Konczykowski, D. Majer, B. Khaykovich, V. M. Vinokur, and H. Shtrikman, Phys. Rev. Lett. **73**, 1428 (1994).
- [3] C. P. Bean and J. D. Livingston, Phys. Rev. Lett. **12**, 14 (1973).
- [4] M. Tinkham, *Introduction to Superconductivity* (McGraw Hill, New York, 1996).
- [5] J. Bardeen, L. N. Cooper, and J. R. Schreiffer, Phys. Rev. **108**, 1175 (1957).
- [6] V. L. Ginzburg and L. D. Landau, Zh. Eksperim. i. Teor. Fiz. (1950).
- [7] R. S. Newrock, C. J. Lobb, U. Geigenmüller, and M. Octavio, Sol. State Phys. **54**, 263 (2000).
- [8] C. Ebner and D. Stroud, Phys. Rev. B **31**, 165 (1985).
- [9] C. de Leo, G. Rotoli, P. Barbara, A. P. Nielsen, and C. J. Lobb, *Mutual inductance route to paramagnetic Meissner effect in 2D Josephson-junction arrays* (2001), submitted to Phys. Rev. B. Also cond-mat/0103199.

- [10] C. Auletta, P. Caputo, G. Costabile, R. de Luca, S. Pace, and A. Saggese, Physica C **235-240**, 3315 (1994).
- [11] F. M. Araujo-Moreira, P. Barbara, A. B. Cawthorne, and C. J. Lobb, Phys. Rev. Lett. **78**, 4625 (1997).
- [12] P. Barbara, F. M. Araujo-Moreira, A. B. Cawthorne, and C. J. Lobb, Phys. Rev. B **60**, 7489 (1999).
- [13] M. Sigrist and T. M. Rice, J. Phys. Soc. Jpn. **61**, 4283 (1992).
- [14] M. Sigrist and T. M. Rice, Rev. Mod. Phys. **67**, 503 (1995).
- [15] B. D. Josephson, Phys. Lett. **1**, 252 (1962).
- [16] A. B. Cawthorne, P. B. S. V. Shitov, C. J. Lobb, K. Wiesenfeld, and A. Zangwill, Phys. Rev. B **60**, 7575 (1999).
- [17] D. Dominguez, E. A. Jagla, and C. A. Balseiro, Phys. Rev. Lett. **72**, 2773 (1994).
- [18] U. Geigenmüller, C. J. Lobb, and C. B. Whan, Phys. Rev. B **47**, 348 (1993).
- [19] E. Ott, *Chaos in Dynamical Systems* (Cambridge UP, New York, 1993).
- [20] A. Mathai, *Superconducting Quantum Interference Device Microscopy and Order Parameter Symmetry in YBa₂Cu₃O_{7- δ}* , Ph.D. thesis, University of Maryland (1995).
- [21] A. Mathai, Y. Gim, R. C. Black, A. Amar, and F. C. Wellstood, Phys. Rev. Lett. **74**, 4523 (1995).
- [22] A. H. Silver and J. E. Zimmerman, Phys. Rev. **157**, 317 (1967).

- [23] A. Barone and G. Paterno, *Physics and Applications of the Josephson Effect* (Wiley, New York, 1982).
- [24] C. Auletta, R. D. Luca, S. Pace, and G. Raiconi, Phys. Rev. B **47**, 14326 (1993).
- [25] C. Auletta, G. Raiconi, R. de Luca, and S. Pace, Phys. Rev. B **51**, 12844 (1995).
- [26] M. Chandran, Phys. Rev. B **56**, 6169 (1997).
- [27] G. Filatrella, A. Petraglia, and G. Rotoli, Euro. Phys. J. B **12**, 23 (1999).
- [28] C. Lucheroni, Phys. Rev. B **55**, 6559 (1997).
- [29] J. R. Phillips, H. S. J. van der Zant, J. White, and T. P. Orlando, Phys. Rev. B **47**, 5219 (1993).
- [30] S. Ramo, J. R. Whinnery, and T. van Duzer, *Fields and Waves in Communications Electronics* (Wiley, New York, 1984), 2nd ed.
- [31] W. Braunisch, N. Knauf, V. Kataev, A. Grütz, A. Kock, B. Roden, D. Khomskii, and D. Wohlleben, Phys. Rev. Lett. **68**, 1908 (1992).
- [32] W. Braunisch, N. Knauf, B. Bauer, A. Kock, A. Becker, B. Freitag, A. Grütz, V. Kataev, S. Neuhausen, B. Roden, D. Khomskii, and D. Wohlleben, Phys. Rev. B **48**, 4030 (1993).
- [33] S. Riedling, G. Bräuchle, R. Lucht, K. Röhberg, H. v. Löhneysen, H. Claus, A. Erb, and G. Müller-Vogt, Phys. Rev. B **49**, 13283 (1994).

- [34] B. Schliepe, M. Stindtmann, I. Nikolic, and K. Baberschke, Phys. Rev. B **47**, 8331 (1993).
- [35] Ü. Onbaşlı, Y. T. Wang, A. Naziripour, R. Tello, W. Kiehl, and A. M. Hermann, Phys. Stat. Sol. B **194**, 371 (1996).
- [36] G. S. Okram, D. T. Adroja, B. D. Padalia, O. Prakash, and P. A. J. de Groot, J. Phys.: Cond. Mat. **9**, L525 (1997).
- [37] D. J. Thompson, M. S. M. Minhaj, L. E. Wenger, and J. T. Chen, Phys. Rev. Lett. **75**, 529 (1995).
- [38] P. Kostić, A. P. Paulikas, U. Welp, V. R. Todt, C. Gu, U. Geiser, J. M. Williams, K. D. Carlson, and R. A. Klemm, Phys. Rev. B **53**, 791 (1996).
- [39] A. Terentiev, D. B. Watkins, and L. E. D. Long, Phys. Rev. B **60**, R761 (1999).
- [40] A. K. Geim, S. V. Dubonos, J. G. S. Lok, M. Henini, and J. C. Mann, Nature **396**, 144 (1998).
- [41] T. M. Rice and M. Sigrist, Phys. Rev. B **55**, 14647 (1997).
- [42] P. Kostić, B. Veal, A. P. Paulikas, U. Welp, V. R. Todt, C. Gu, U. Geiser, J. M. Williams, K. D. Carlson, and R. A. Klemm, Phys. Rev. B **55**, 14649 (1997).
- [43] A. P. Nielsen, J. Holzer, A. B. Cawthorne, C. J. Lobb, R. S. Newrock, and J. Markus, in *Rencontres du Vietnam: Superconductivity, Magneto-Resistive Materials and Strongly Correlated Quantum Systems.*, edited by N. V. Hieu, T. T. Van, and G. Xiao (1999), p. 75.

- [44] A. P. Nielsen, J. Holzer, A. B. Cawthorne, C. J. Lobb, R. S. Newrock, and J. Markus., Physica B **280**, 444 (2000).
- [45] A. P. Nielsen, A. B. Cawthorne, P. Barbara, F. C. Wellstood, C. J. Lobb, R. S. Newrock, and M. G. Forrester, Phys. Rev. B **62**, 14380 (2000).
- [46] Currently the Northrop-Grumman Corp, Baltimore, MD.
- [47] J. M. Jaycox and M. B. Ketchen, IEEE Trans. Magn. **Mag-17**(1), 400 (1981).
- [48] J. R. Kirtley, A. C. Mota, M. Sigrist, and T. M. Rice, J. Phys.: Cond. Mat. **10**, L97 (1998).
- [49] J. R. Kirtley, M. B. Ketchen, K. G. Stawiasz, J. Z. Sun, W. J. Gallagher, and S. H. Blanton, Appl. Phys. Lett. **66**, 1138 (1995).
- [50] Keithley Instruments, Inc., 28775 Aurora Road, Cleveland, Ohio 44139. Phone: 800-552-1115, Fax: 440-248-6168, <http://www.keithley.com>.
- [51] A. E. Koshelev and A. I. Larkin, Phys. Rev. B **52**, 13559 (1995).
- [52] C. Auletta, G. Raiconi, R. De Luca, and S. Pace, Phys. Rev. B **49**, 12311 (1994).
- [53] V. V. Moschalkov, X. G. Qiu, and V. Bruyndoncx, Phys. Rev. B **55**, 11793 (1999).
- [54] P. S. Deo, V. A. Schweigert, F. M. Peeters, and A. K. Geim, Phys. Rev. Lett. **79**, 4653 (1997).

- [55] P. S. Deo, V. A. Schweigert, and F. M. Peeters, Phys. Rev. B **59**, 6039 (1999).
- [56] W. Prusseit, H. Walter, R. Semerad, H. Kinder, W. Assmann, H. Huber, B. Kabius, H. Burkhardt, D. Rainer, and J. A. Sauls, Physica C **317–318**, 396 (1999).
- [57] L. D. Landau and E. M. Lifshitz, *Electrodynamics of Continuous Media* (Pergamon, New York, 1960), translated by J. B. Sykes and J. S. Bell.
- [58] J. D. Jackson, *Classical Electrodynamics* (Wiley, New York, 1962), 2nd ed.
- [59] D. M. Feldman, J. L. Reeves, A. A. Polyanskii, G. Kozlowski, R. R. Biggers, R. M. Nekkanti, T. L. Peterson, S. E. Babcock, and D. C. Larbalestier, Appl. Phys. Lett. **77**, 1 (2000).
- [60] D. M. Feldman, J. L. Reeves, A. A. Polyanskii, A. Goyal, R. Feenstra, D. F. Lee, M. Paranthaman, D. M. Kroeger, D. K. Christen, S. E. Babcock, and D. C. Larbalestier (2000).
- [61] Home page of RABiTS at Oak Ridge National Lab, <http://www.ornl.gov/~vhk/rabits.html>.
- [62] A. I. Larkin and Y. N. Ovchinnikov, Sov. Phys. JETP **34**, 651 (1972).
- [63] A. T. Dorsey, Phys. Rev. B **51**, 15329 (1995), and references therein.
- [64] E. H. Brandt, Phys. Rev. Lett. **71**, 2821 (1993).
- [65] E. H. Brandt, Phys. Rev. B **49**, 9024 (1994).
- [66] E. H. Brandt, Phys. Rev. B **54**, 4246 (1996).

- [67] E. H. Brandt and G. P. Mikitik, Phys. Rev. Lett. **85**, 4164 (2000).
- [68] D. Y. Vodolazov and I. L. Maksimov, Physica C **349**, 125 (2001).
- [69] A. V. Kuznetsov, D. V. Eremenko, and V. N. Trofimov, Phys. Rev. B **59**, 1507 (1999).
- [70] T. H. Johansen, M. Baziljevich, H. Bratsberg, Y. Galperin, P. E. Lindelof, Y. Shen, and P. Vase, Phys. Rev. B **54**, 16264 (1996).
- [71] C. Ferdeghini, E. Giannini, G. Grassano, D. Marré, I. Pallecchi, and A. S. Siri, Physica C **294**, 233 (1998).
- [72] L. Landau and L. Lifshitz, Phys. Z. Sowjetunion **8**, 153 (1935).
- [73] H. R. Kercher, D. P. Norton, A. Goyal, D. K. Christen, D. M. Kroeger, M. Paranthaman, D. F. Lee, F. A. List, and R. Feenstra, Phys. Rev. B **60**, 6878 (1999).
- [74] A. S. Arrott and T. L. Templeton, Physica C **233**, 259 (1997).
- [75] R. Hertel and H. Kronmüller, Phys. Rev. B **60**, 7366 (1999).
- [76] Formerly EG&G Princeton Applied Research, presently Perkin-Elmer Instruments, <http://www.instruments.perkinelmer.com> Princeton Applied Research - Headquarters, 801 S. Illinois Ave., Oak Ridge, TN 37831-0895, Phone: 800-366-2741, 865-482-4411 Ext. 343, Fax: 865-425-1334.
- [77] T. Ishida and R. B. Goldfarb, Phys. Rev. B **41**(13), 8937 (1990).
- [78] K. Yamamoto, H. Mazaki, H. Yasouka, S. Katsuyama, and K. Kosuge, Phys. Rev. B **46**(2), 1122 (1992).

- [79] W. K. H. Panofsky and M. Phillips, *Classical Electricity and Magnetism* (Addison-Wesley, Reading, MA, 1955), 2nd ed.
- [80] M. Nikolo and R. B. Goldfarb, Phys. Rev. B **39**, 6615 (1989).
- [81] J. R. Clem, in *Magnetic Susceptibility of Superconductors and Other Spin Systems*, edited by R. A. Hein, T. L. Francavilla, and D. H. Liebenberg (Plenum, New York, 1991), pp. 177–211.
- [82] S. Çelebi, I. Karaca, E. Aksu, and A. Gencer, Physica C **309**, 131 (1998), and references therein.
- [83] K. H. Müller, M. Nikolo, and R. Driver, Phys. Rev. B **43**, 7976 (1991).
- [84] R. C. Black, A. Mathai, F. C. Wellstood, E. Dantsker, A. H. Miklich, D. T. Nemeth, J. J. Kingston, and J. Clarke, Appl. Phys. Lett. **62**, 2128 (1993).
- [85] J. Pearl, in *Low Temperature Physics, LT9*, edited by J. G. Daunt, D. O. Edwards, F. J. Milford, and M. Yaqub (Plenum, New York, 1965), vol. A, pp. 566–570.
- [86] J. Pearl, Appl. Phys. Lett. **5**(4), 65 (1964).
- [87] R. Liang, P. Dosanjh, D. A. Bonn, and W. N. Hardy, Phys. Rev. B **50**(6), 4212 (1994), and references therein.
- [88] A. B. Cawthorne, C. B. Whan, and C. J. Lobb, J. Appl. Phys. **84**, 1126 (1998).
- [89] P. Bak, C. Tang, and K. Wiesenfeld, Phys. Rev. Lett. **59**(4), 381 (1987).
- [90] S. L. Ginzburg, JETP **79**(2), 334 (1994).

- [91] C. Tang, Physica A **194**, 315 (1993).
- [92] D. Shi and Z. Wang, IEEE Trans. Appl. Supercon. **5**(2), 1721 (1995).
- [93] S. Field, J. Witt, X. Ling, and F. Nori, Phys. Rev. Lett. **74**, 1206 (1995).
- [94] R. P. Feynmann, R. B. Leighton, and M. L. Sand, *The Feynmann Lectures on Physics*, vol. 1 (Addison-Wesley, Reading, MA, 1963), chap. 46.
- [95] C. S. Lee, B. Janko, I. Derenyi, and A. L. Barabasi, Nature **400**, 337 (1999).
- [96] F. Falo, P. J. Martinez, J. J. Mazo, and S. Cilla, Europhys. Lett. **45**(6), 700 (1999).
- [97] E. Goldobin, A. Sterck, and D. Koelle, *Josephson Vortex in a Ratchet Potential: Theory* (2000), cond-mat/0008237.
- [98] E. Trias, J. J. Mazo, F. Falo, and T. P. Orlando, Phys. Rev. E **61**(3), 2257 (2000).
- [99] J. F. Wambaugh, C. Reichardt, C. J. Olson, F. Marchesoni, and F. Nori, Phys. Rev. Lett. **83**, 5106 (1999).
- [100] I. Zapata, F. Sols, and P. Hanggi, Phys. Rev. Lett. **77**(11), 2292 (1996).
- [101] R. D. Astumian, Science **276**, 917 (1997).
- [102] R. D. Astumian and F. Moss, Chaos **8**(3), 533 (1998).
- [103] F. Jülicher, A. Ajdari, and J. Prost, Rev. Mod. Phys. **69**(4), 1269 (1997).
- [104] M. O. Magnasco, Phys. Rev. Lett. **71**(10), 1477 (1993).
- [105] T. R. Kelly, J. P. Sestelo, and I. Tellitu, J. Org. Chem. **63**, 3655 (1998).

- [106] J. Prost, J.-F. Chauwin, L. Peliti, and A. Ajdari, Phys. Rev. Lett. **72**(16), 2652 (1994).
- [107] L. P. Faucheux, L. S. Bourdieu, P. D. Kaplan, and A. J. Libchaber, Phys. Rev. Lett. **74**(9), 1504 (1995).
- [108] KLA-Tencor, Corp. Phone: 800-600-2829. <http://www.kla-tencor.com/>.
- [109] R. C. Black, *Magnetic Microscopy Using a Superconducting Quantum Interference Device*, Ph.D. thesis, University of Maryland (1995).
- [110] Professor Richard Newrock, Department of Physics, University of Cincinnati, Cincinnati, OH 45221, richard.newrock@uc.edu.
- [111] LakeShore Cryotronics, Inc. 575 McCorkle Blvd., Westerville, OH 43082-8888, Phone: 614-891-2244, FAX: 614-818-1600, <http://www.lakeshore.com>.
- [112] Neocera, Inc., Instrument and Systems Group, 10000 Virginia Manor Road, Suite 300, Beltsville, MD 20705-4215, Phone: 301-210-1010, FAX: 301-210-1042, <http://www.neocera.com/>.
- [113] Hypres, Inc., 175 Clearbrook Road, Elmsford, NY 10523, Phone: 914-592-1190, FAX: 914-347-2239, <http://www.hypres.com>.
- [114] Harris Semiconductor, 2401 Palm Bay Road NE, Palm Bay, FL 32905. Phone: 407-724-7000 or 800-4-HARRIS.
- [115] SPK Electronics Company, Ltd., 10F, No. 510, Sec 5, Chung Hsiao E., Taipei, Taiwan. Phone: 886-2-23462323, <http://www.spkecl.com/>.

- [116] Texas Instruments, PO Box 655303, Dallas, TX 75265.
<http://www.ti.com/>.
- [117] Agilent Technologies, formerly Hewlett-Packard Corp.,
<http://www.agilent.com/>.
- [118] Dynapro Thin Film Products, Inc., 7025 W. Marcia Road, Milwaukee, WI
53223, USA. Phone 414-365-3555.
- [119] Oregon Microsystems, Inc. <http://www.omsmotion.com/>.
- [120] National Instruments, <http://www.natinst.com/>.
- [121] A. B. Cawthorne, *68HC11-GPIB Rev. C, User's Guide*, University of
Maryland (1998), manual for the 68HC11-GPIB board designed by Fred
Cawthorne and used specifically for the SQUID microscope joystick con-
trol.
- [122] A. B. Cawthorne, *Dynamics of Josephson Junctions and Josepson-Junction
Arrays*, Ph.D. thesis, University of Maryland (1998).
- [123] Emerson & Cuming, 869 Washington Street, Canton, MA 02021, Phone:
781-828-3300, FAX: 781-828-3104.
- [124] Apiezon Products, M&I Materials Ltd., PO Box 136, Manchester M60 1AN
England. Phone +44 (0) 161 875 4096.

Index

H_c , 1

λ , *see* London penetration depth

n , *see* quantum number

H_{c1} , 1, 112–114, 115

H_{c2} , 1

π -junction, 14, 28

APNSQD1, 143

APNSQD2, 143

A/D board, 160

AC susceptibility, 89–91

alignment

 finding sample at 4.2 K, 176

 sample slider

 grabbing, 171

 travel range, 171

 SQUID-sample

 coordinates, 167

 horizontal, 167

 z-control, 165

BCS theory, 3

bugs,software

 changing data display, 161

 crash detect, 152

 GPIB, 156

 lock up after scan, 156

 scan abort, 156

 joystick, 161

controller coordinates, 150

cooling

 exchange gas, 175

 helium, 175

 nitrogen, 173

 transfer time, 173

critical state, 114

DC susceptibility, 98

demagnetization factor, 112

diffusion pump, 172

eddy currents, 94

flux compression, 59

fluxoid quantization, 9

- friction, 43, 140
- gauge invariant phase difference, 7
- Gibbs free energy, 19
- GPIB commands, 152
- Hall probe, 86
- Hamiltonian, 23
- heating, 43, 140
- induction matrix, 24
- Josephson relations, 7
- joystick control, 161
- lead can, 171
- leak checking, 172
 - cold, 179
- leaks
 - cold
 - nitrogen, 174
 - reproducibility, 174
- London equation, 94, 110
- London penetration depth, 94, 108
- magneto optical indicator films, 86
- mean field theory, 62
- Meissner effect, 1, 27
- Meissner state, *106–112*
- paramagnetic Meissner effect, 27
- pinouts
 - 77 K, 174
 - room temperature, 167
- pre-cooling, 173
- quantum number, *10–12*
- RABiTS, 82, *86–89*
 - AC susceptibility, 89
 - DC susceptibility, 98
- ratchet effect, 130
- RCSJ model, *7–10*
 - stability analysis, 17
- remanence, 114
- RSJ model, 9
- sample mounting, 162
 - contacts to probe, 167
- sample slider
 - 77 K, 175
 - mechanical grabbing, 171
 - scanning friction, 178
- scanning
 - acceleration, 151
 - columns, 152
 - coordinate system, 150

- crash detect, 152
- data files, 160
- direction, 151
- friction, 140
- record pots, 152
- rows, 152
- velocity, 151
- scanning range, 142
- self inductance
 - square, 65–68
- self organized criticality, 128
- shunted arrays, 127
- SQUID
 - IC design, 142
 - mounting, 164
 - contacts to probe, 167
 - thermal cycling, 165
- SQUID electronics, 143
 - digital phase detector, 143
 - frequency response, 147
- SQUID-sample alignment
 - coordinates, 167
 - horizontal, 167
 - z-control, 165
- stepper motors, 156
- calibration, 142
- coordinates, 142, 157–158
- superconductor
 - high T_c , 2
 - low T_c , 2
 - s-wave, 3
 - type I, 2
 - type II, 2
- temperature control
 - sample, 178
 - SQUID, 178
- thermometer
 - placement, 137
- vacuum can, 171
- vortex, 1
 - avalanche, 119
 - ratchet effect, 130
- warming probe, 179
- Wohllleben effect, 27